DISS. ETH NO. 27357

MODEL-BASED ASSESSMENT OF STATIONARY ENERGY STORAGE IN BATTERIES AND IMPLICATIONS FOR MATERIALS RESEARCH

A dissertation submitted to attain the degree of

DOCTOR OF SCIENCES of ETH ZURICH
(Dr. sc. ETH Zurich)

presented by

SIMON FABIAN SCHNEIDER
MSc ETH Chemistry

born on June 21, 1993

citizen of
Eriswil (BE), Switzerland

Accepted on the recommendation of

Prof. Dr. P. Novák
Prof. Dr. G. Hug
Mr. C. Bauer
Dr. T. Kober

2021

Simon Fabian Schneider: *Model-based assessment of stationary energy storage in batteries and implications for materials research,* 2021.

ABSTRACT

Large-scale energy storage is one of the prerequisites for the successful integration of renewable energy sources into the electricity supply system. In the past years, storage technologies including rechargeable lithium-ion batteries (LIBs) have therefore increasingly been deployed in numerous stationary application cases. While batteries offer several benefits, they inevitably degrade over time and use until they can no longer provide the designated service. The replacement of batteries that have reached the end of their lifetime does not only cause economic costs but also presents an environmental burden, as their manufacturing is associated with the depletion of critical resources and emission of greenhouse gases. Thus, the viability of stationary energy storage in rechargeable batteries depends on a complex interplay of multiple parameters related to the battery chemistry, battery manufacturing, and battery use phase.

This thesis presents a new assessment framework (i) to compare the technical, economic, and environmental viability of batteries on a cell level and (ii) to analyze the deployment and operation of battery systems providing grid-level energy storage. Consistency in the assessment of different battery technologies and application cases is ensured by combining and further developing modeling approaches from a wide range of research communities, including electrochemical battery performance models, semi-empirical battery degradation models, battery cost models, life cycle assessment (LCA), and energy-economic simulation and optimization models. The developed assessment framework was used to analyze multiple case studies and business cases. Based on the model results, this thesis provides guidelines and recommendations for further research on rechargeable batteries and the materials they are composed of.

The first part of this thesis is dedicated to the assessment of battery cells from a technical, economic, and environmental point of view. To this end, an electrochemical pseudo-two-dimensional (P2D) model is employed to assess practical specific energies of intercalation-based battery cells under varying discharge rates. Subsequently, the outputs of the P2D model are used to parameterize a bottom-up battery cell cost model and to assess greenhouse gas emissions associated with the manufacturing of battery cells from a life cycle perspective. Serving as a case study for the modeling framework, a comparative assessment of different LIBs and sodium-ion batteries (NIBs) was performed. The model results suggest that NIBs need further improvement on the materials level in order to become competitive with LIBs.

A strong inverse correlation has been found between the practical specific energy of battery cells and both their manufacturing costs and environmental impacts. By contrast, other drivers, such as cost savings due to the replacement of lithium-based materials by sodium-based ones, play only a relatively minor role under current raw material costs. NIBs are therefore most likely to become competitive with LIBs if the specific energy of NIBs can be further increased. This translates into a need for anode and cathode active materials that offer higher specific charges, higher gravimetric densities, and higher voltages.

The second part of this thesis is devoted to the techno-economic assessment of battery systems providing different stationary services, including peak shaving (PS), price arbitrage (PA), and primary control reserves (PCR) under a wide range of current and prospective electricity market conditions. The model results suggest that the provision of PS and PCR services is generally profitable under current investment costs of LIBs due to the high revenue potential of these application cases. By contrast, battery systems performing PA require both technical improvement and significant cost reduction in order to reach economic viability. On the whole, the findings of this thesis support the expectation that LIBs will continue to play a vital role in modern electricity supply systems.

An evaluation of different performance targets for battery systems shows that the research priorities vary considerably depending on the application case. This underlines that there is no *one-target-fits-all strategy* for the further development of today's LIBs. The model results suggest, however, that the second life use of batteries, which is enabled by extending their lifetime beyond 80% remaining capacity, is an important development target for all applications cases considered in this thesis. In addition, the following technical improvements are desirable, as they would improve the economics of stationary batteries: (I) Longer cycle lifetimes would be particularly beneficial for batteries that perform PA on electricity markets with high price volatility. (II) Higher energy efficiency would be desirable for batteries that perform PA on electricity markets with low price volatility. (III) The provision of PCR requires batteries to perform many shallow charge and discharge cycles. Hence, depending on the LIB technology used, the cycle stability should be further improved to ensure that they can sustain a high number of shallow cycles.

Overall, the holistic modeling approach presented in this thesis provides new insights into desirable improvements of today's rechargeable batteries.

ZUSAMMENFASSUNG

Die grosstechnische Energiespeicherung ist eine Voraussetzung für die erfolgreiche Integration von erneuerbaren Energien in das Stromversorgungssystem. In den letzten Jahren sind elektrochemische Speichertechnologien wie Lithium-Ionen-Batterien (LIBs) daher vermehrt für eine Vielzahl von stationären Anwendungen eingesetzt worden. Während Batterien mehrere Vorteile bieten, finden über die Zeit und mit zunehmender Nutzung Degradationsprozesse statt, die mit einer Verschlechterung ihrer Leistungsfähigkeit einhergehen. Batterien, welche das Ende ihrer Lebensspanne erreicht haben, können ihren Einsatzzweck nicht mehr erfüllen und müssen daher ausgetauscht werden. Dies verursacht nicht nur ökonomische Kosten, sondern stellt auch eine Umweltbelastung dar, da die Herstellung von Batterien mit der Erschöpfung von kritischen Ressourcen und der Emission von Treibhausgasen verbunden ist. Die Eignung von Batterien als stationäre Energiespeicher hängt somit von einem komplexen Zusammenspiel mehrerer Faktoren ab, welche durch die Batterie-Chemie, Batterie-Herstellung sowie Batterie-Nutzungsphase bestimmt werden.

In dieser Arbeit werden neue Berechnungsmodelle präsentiert, (i) um die technische, ökonomische und ökologische Eignung verschiedener Batterie-Technologien auf der Zellebene abzuschätzen, und (ii) um den Einsatz und Betrieb von netzgekoppelten Batteriesystemen zu analysieren. Um eine konsistente Untersuchung verschiedener Batterie-Technologien und stationärer Anwendungsfälle zu gewährleisten, werden Modellierungsansätze aus einem breiten Spektrum von Forschungsdisziplinen verwendet und weiterentwickelt, wie zum Beispiel elektrochemische Batterie-Leistungsmodelle, semi-empirische Batterie-Degradationsmodelle, Batterie-Kostenmodelle, Umweltbilanzen sowie energieökonomische Simulations- und Optimierungsmodelle. Die in dieser Arbeit entwickelten Berechnungsmodelle wurden verwendet, um eine Vielzahl von Fallbeispielen und Anwendungsfällen zu analysieren. Basierend auf den Modellrechnungen werden Empfehlungen vorgeschlagen, die als Leitfaden für zukünftige Forschung auf dem Gebiet der wiederaufladbaren Batterien und deren Materialien dienen.

Der erste Teil dieser Arbeit ist der technischen, ökonomischen und ökologischen Evaluation von Batteriezellen gewidmet. Zu diesem Zweck wird ein elektrochemisches pseudo-zweidimensionales (P2D) Modell verwendet, um die praktische spezifische Energie von Batteriezellen mit Interkalationselektroden unter verschiedenen Entladeraten zu berechnen. Die Modellresultate dienen in einem zweiten Schritt der Parametrisierung eines Bottom-up Batteriezellen-Kostenmodells und der

Quantifizierung von Treibhausgasemissionen, die bei der Rohstoffgewinnung und anschliessenden Batterie-Herstellung anfallen. Als Fallbeispiel wurden LIBs und Natrium-Ionen-Batterien (NIBs) untersucht. Die Modellrechnungen zeigen, dass die Aktivmaterialien von NIBs noch verbessert werden müssen, damit NIBs wettbewerbsfähig werden mit LIBs.

Die Modellresultate zeigen eine starke inverse Korrelation zwischen der spezifischen Energie von Batteriezellen und deren Herstellungskosten wie auch deren Umweltbelastung auf. Im Gegensatz dazu spielen andere Einflussfaktoren wie Kostenersparnisse durch den Ersatz von lithiumbasierten durch natriumbasierte Materialien nur eine relativ geringfügige Rolle unter den gegenwärtigen Rohmaterialkosten. NIBs werden daher am ehesten wettbewerbsfähig mit LIBs, wenn deren spezifische Energie weiter gesteigert werden kann. Dies erfordert die Entwicklung von Anoden- und Kathoden-Aktivmaterialien mit höheren spezifischen Ladungen, höheren gravimetrischen Dichten sowie höherer Zellspannung.

Der zweite Teil dieser Arbeit beschäftigt sich mit der technoökonomischen Untersuchung von Batteriesystemen, welche verschiedene stationäre Dienstleistungen, wie Lastverschiebung (LS), Preisarbitrage (PA) und Primärregelleistung (PRL) unter einer weiten Bandbreite von gegenwärtigen und prospektiven Elektrizitätsmarktszenarien erbringen. Die Modellresultate zeigen, dass der Einsatz von Batterien für LS und PRL unter den gegenwärtigen Investitionskosten für LIBs wirtschaftlich sein kann, da in diesen Anwendungen hohe Einnahmen generiert werden. Im Gegensatz dazu ist der Einsatz von Batterien für PA nur dann wirtschaftlich, wenn sowohl technische Verbesserungen der Batterie-Systeme als auch deutliche Kostensenkungen erzielt werden. Im Grossen und Ganzen stehen die in dieser Arbeit präsentierten Resultate in Einklang mit der Erwartung, dass LIBs in modernen Stromversorgungssystemen weiterhin eine bedeutende Rolle zukommen wird.

Eine Beurteilung von verschiedenen Leistungsparametern zeigt, dass sich die Forschungs-Prioritäten für die Weiterentwicklung von Batterie-Systemen je nach Anwendungszweck stark unterscheiden. Diese Erkenntnis verdeutlicht, dass es *nicht* ein *einziges* Entwicklungsziel für LIBs gibt, welches allen Ansprüchen gerecht wird. Die Modellrechnungen zeigen jedoch auf, dass die Second-Life-Nutzung von Batterien, welche eine Verlängerung ihrer Lebensdauer unterhalb von 80% Restkapazität bedingt, für alle in dieser Arbeit untersuchten Anwendungsfälle von grosser Bedeutung ist. Um die Wirtschaftlichkeit von stationären Batterien zu verbessern, sind zudem die folgenden technischen Fortschritte wünschenswert: (I) Eine längere zyklische Lebensdauer wäre insbesondere vorteilhaft für Batterien, welche für PA auf Elektrizitätsmärkten mit hoher Preisvolatilität eingesetzt werden. (II) Ein höherer Energiewirkungsgrad wäre von Vorteil für Batterien, welche für PA auf Elektrizitätsmärkten mit geringer

Preisvolatilität genutzt werden. (III) Bei der Erbringung von PRL sind Batterien einer Vielzahl von mehrheitlich flachen Lade- und Entladezyklen ausgesetzt. Je nach eingesetzter LIB-Technologie sollte daher die Zyklenfestigkeit weiter verbessert werden, um sicherzustellen, dass sie einer hohen Anzahl von flachen Zyklen standhalten können.

Insgesamt liefert der in dieser Arbeit entwickelte holistische Modellierungsansatz neue Erkenntnisse bezüglich der wünschenswerten weiteren Entwicklung von wiederaufladbaren Batterien.

ACKNOWLEDGEMENTS

First of all, I would like to thank my doctor father, Prof. Dr. Petr Novák, for his continuous support and scientific guidance over the past 3.5 years. I am grateful for the opportunity to carry out my PhD thesis under his supervision at the Paul Scherrer Institute. I have profited tremendously not only from his profound knowledge of electrochemistry and rechargeable batteries but also from his experience in collaborating across different research fields. Being shown how to manage interdisciplinary research projects effectively has been an invaluable experience.

I would like to thank my supervisors, Prof. Dr. Erik Berg, Dr. Tom Kober and Mr. Christian Bauer, for the opportunity to work in their research groups and for their scientific guidance: Erik for introducing me to the world of electrochemical battery modeling, Tom for his valuable feedback on the economic aspects of my work, and Christian for sharing his extensive expertise in life cycle assessment with me. It was a stimulating experience to work on such a wide range of research topics, and I am grateful to my supervisors for creating the environment to carry out an interdisciplinary PhD project.

I would like to thank Dr. Sigita Trabesinger for her support during the last two years of my thesis. I enjoyed our battery-related discussions as much as I profited from her truly remarkable skills in organizing group events and bringing people together.

I would like to thank Dr. Antriksh Singh for his support with time series clustering and for sharing other useful modeling ideas with me, Dr. Martin Densing for fruitful discussions about optimization problems and for his feedback on mathematical topics, Dr. Christopher Mutel and Dr. Brian Cox for teaching me how to improve my Python code writing, and Ms. Xiaojin Zhang for stimulating collaborations on battery life cycle assessment.

Financial support from SCCER and PSI is gratefully acknowledged.

I would like to thank Dr. Giovanni Castelli and Mr. Michael Vogel from *AEW Energie AG*, Dr. Marina González Vayá from *Elektrizitätswerke des Kantons Zürich*, and Mr. Serge Wisselmann and Dr. Walter Sattinger from *Swissgrid* for fruitful discussions and support.

I would like to thank Dr. Tino Wagner for sharing his LaTeX template for a

PhD thesis at ETH Zurich. It saved me a lot of work.

Furthermore, I would like to thank my colleagues and office mates (back in the pre-Corona age) who made my time at the Paul Scherrer Institute an unforgettable (in the positive sense!) memory: Eibar, Paul, Giulio, Christoph, Laura, Marta, Max, Aurélie, Daniela, Dave, Leiting, Łukasz, Steven, Eric, Aymane, Anna, Salvo, Sandro, Michel, Lydia, Yi - to name only a few of the many people I had the pleasure to work and spend time with. To use one of my favorite words in the English language - it was very *pleasant* having you all around!

Last but not least, I would like to thank my family and friends. I may not tell you often enough, but none of the endeavours in my life, be it academic, professional, or private, would be possible without you, nor would it be fun to even try.

CONTENTS

1

INTRODUCTION

1.1 STATIONARY ENERGY STORAGE

Human influence on climate has been the main cause for global warming since the mid-20th century. To date, temperature rise has induced severe alterations to humanity and nature, including increases in droughts, floods, sea level rise, biodiversity loss, and extreme weather events. [1] In an attempt to mitigate the devastating impact of anthropogenic climate change, the Paris Agreement defines a long-term goal of holding the global average temperature increase to well below 2 °C. [2] Efforts undertaken in the past years towards this goal include the reduction of CO_2 emissions in the energy sector through increased integration of renewables, such as wind energy and photovoltaics. Whereas these energy sources play a key role in transitioning into a low-carbon society, their intermittent nature necessitates complementary technologies for reliable electricity supply. Stationary energy storage is therefore increasingly deployed to balance deviations between electricity supply and demand. Electrochemical batteries including rechargeable lithium-ion batteries (LIBs) have proven great potential for numerous grid-level and off-grid applications due to their fast response time, high round-trip efficiency, low self-discharge, and scalability. [3, 4] Apart from stationary energy storage, LIBs are at the core of many mobile and portable applications, being the state-of-the-art technology for electric vehicles, laptops, and mobile phones. [5] The tremendous technical and economic significance of LIBs is reflected in the size of the global LIB market, which was valued $37 billion in 2019 and is projected to grow to $129 billion by 2027 [6].

1.2 BATTERIES AS STATIONARY ENERGY STORAGE SYSTEMS

Stationary energy storage in rechargeable batteries can support the integration of renewable energy sources into the grid and thus the decarbonization of the electricity supply system in different ways, which gives rise to multiple application cases that allow battery operators to generate economic revenues. Three frequently discussed application cases include (i) price arbitrage (PA) business, (ii) demand peak shaving (PS), and (iii) frequency regulation (FR). PA uses the battery to exploit temporal price differentials on the electricity market [7, 8]. In PS, batteries generate economic value indirectly by lowering the peak load of electricity consumers that incur not only

energy specific (kWh) electricity costs but also costs that scale with the peak load (kW) during the billing period [7, 9]. In FR, economic value is created by reducing deviations from the optimum grid frequency when the supply and demand of electricity are not balanced. Battery operators are usually remunerated for providing FR by the responsible transmission system operator (TSO). [7]

As time passes, batteries inevitably degrade until they no longer fulfil the technical requirements for the designated service [10, 11]. Battery components that have reached the end of their useful lifetime, normally the battery cells, must be replaced, which causes not only economic costs but also presents a substantial environmental burden, as the manufacturing of battery cells is associated with the depletion of resources with critical supply chains (e.g., cobalt and lithium) and emission of toxic substances and greenhouse gases. [7, 12–14] The suitability of rechargeable batteries for stationary energy storage is therefore contingent on several parameters, such as:

- battery performance including specific energy (kWh/kg) and specific power (kW/kg),
- raw material and battery manufacturing costs (EUR/kWh),
- greenhouse gas emissions due to raw materials mining (including energy consumption and the entirety of the supply chains), transportation, battery manufacturing and assembly, and battery system deployment (CO_2-eq./kWh),
- battery lifetime (number of charge/discharge cycles and number of service years),
- round-trip energy efficiency (%) of the energy storage system as well as economic and environmental costs due to energy losses, and
- second life aspects and recycling.

The above parameters are dependent on a complex interplay of multiple factors related to the battery chemistry (e.g., active materials), battery manufacturing (e.g., cell design and assembly), and battery use phase (e.g., application case and dispatch strategy). To ensure a reliable and consistent assessment of varying battery chemistries and application cases, the scientific literature therefore highlights the need for assessment methods which rely on modeling approaches from different research communities that are integrated in a systematic way. [7, 12, 15, 16]

1.3 WORKING PRINCIPLE OF LITHIUM-ION BATTERIES

LIB cells consist of a positive and negative electrode, which are separated by an electronically insulating separator soaked with an ionically conducting electrolyte solution

(see figure 1.1). Although not strictly applicable to secondary batteries, positive and negative electrodes are commonly referred to as *cathode* and *anode*, respectively. This convention, which is based on the discharge of a battery as a technical standard, is followed throughout this thesis. During discharge, lithium ions move from the anode to the cathode through the pores of the separator. By electroneutrality, this ionic flux is compensated by a concurrent release of electrons by the anode, resulting in an electric current between the anode and the cathode in an external electric circuit. In secondary batteries, these processes are reversible, which allows the battery to be recharged by applying an external power source. [17]

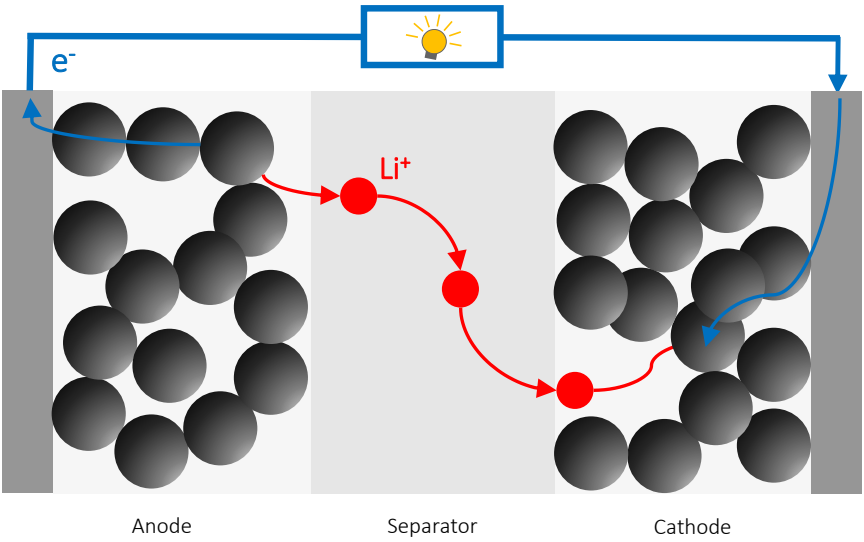

FIGURE 1.1: Schematic of a LIB cell. During discharge, lithium ions and electrons are transferred from the anode to the cathode side. During charge, the processes are reversed. Figure redrawn based on Ref. [18].

A LIB storage system is composed of the battery itself (multiple battery cells assembled into packs) and auxiliary components including the cooling system, thermal management system, and an energy management system. In addition, battery systems used in stationary energy storage applications typically require a power electronics system consisting of multiple AC/DC inverter and voltage transformer units. [4, 10, 19, 20] Figure 1.2 shows a schematic of a grid-connected battery system.

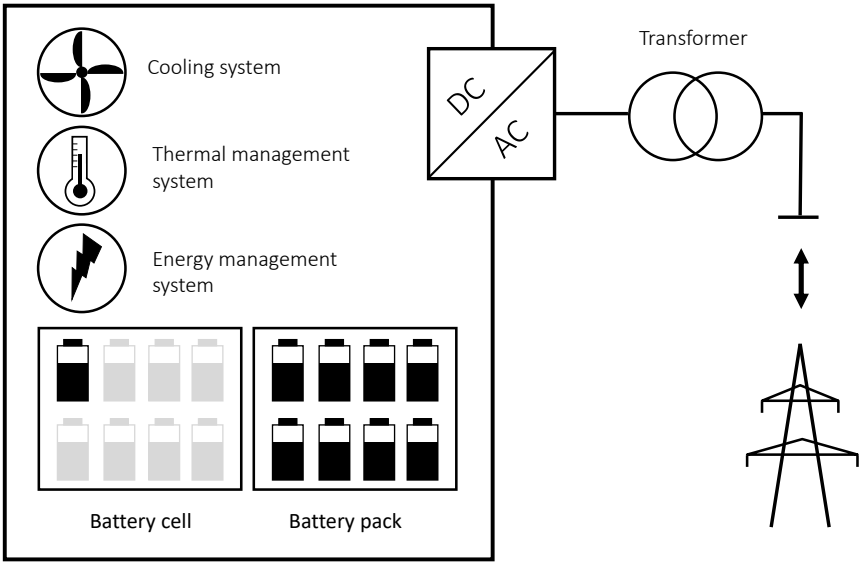

FIGURE 1.2: Schematic of a grid-connected battery system. Figure redrawn based on Ref. [4].

1.4 SCOPE OF THE THESIS

The goal of this thesis is to develop computational models (i) to assess the suitability of rechargeable batteries as stationary energy storage systems and (ii) to establish guidelines for materials and battery research on desirable improvements for current and emerging energy storage technologies. To this end, a wide range of modeling approaches from different research communities are employed, further developed, and combined into an assessment framework: (i) physics-based battery performance and semi-empirical battery degradation models, (ii) battery cell manufacturing models, (iii) environmental impact analysis models based on the methodology of life cycle assessment (LCA), and (iv) energy-economic simulation and optimization models for battery dispatch analysis. The following research problems are addressed in this thesis:

1.) Assessment of batteries on the cell level

- Comparative assessment of specific energy and power, manufacturing costs, and life cycle environmental impacts of current and emerging battery chemistries.

2.) Techno-economic assessment of batteries in stationary applications

- Economic assessment of using batteries in different application cases, including PA, PS, and FR. In addition, the impact of the battery configuration and dispatch strategy on battery degradation and lifetime revenues is analyzed.

1.5 THESIS OUTLINE

Chapter 2 reviews the literature on the computational modeling of LIBs with a particular emphasis on physics-based and semi-empirical battery cell performance and degradation models. Chapter 3 presents a new modeling framework to assess specific energies, manufacturing costs, and environmental impacts of intercalation-based practical battery chemistries. Serving as a validation and case study for the developed framework, a comparative assessment of LIBs and sodium-ion (Na^+) batteries (NIBs) is provided. In chapter 4, the focus of the analysis is shifted from the battery cell to the battery systems level. To this end, two models are developed for the technical and economic assessment of batteries in stationary applications: (i) an optimization model for batteries performing combined PA and PS, and (ii) a simulation model to analyze the provision of FR, such as primary control reserves (PCR). Chapter 5 builds upon the models introduced in chapter 3 and 4 and provides a wide range of case studies for batteries providing PS, PA, and PCR services under different electricity market conditions. Chapter 6 summarizes the main findings of the thesis, discusses their implications for the further development of rechargeable batteries, and provides an outlook for future research.

2

COMPUTATIONAL MODELING OF BATTERIES

This chapter provides an overview of the computational modeling of LIBs.[1] First, the main modeling approaches are reviewed, ranging from physics-based to data-driven ones, by comparing their predictive power, level of mechanistic understanding, and applicability to battery monitoring, diagnostics, and optimal control. Then, the pseudo-two-dimensional (P2D) model is discussed, which is one of the most widely used physics-based battery cell models. The chapter concludes with a review of battery lifetime assessment, with a particular emphasis on semi-empirical degradation models that are applicable to control problems for battery dispatch optimization. While the present chapter focuses on the computational modeling of LIBs, commonly used anode and cathode materials are introduced and discussed on the way. For an overview of the state-of-the-art of LIB active materials and cell components, the interested reader is referred to a recent review article of Armand et al. [21] and references therein.

2.1 REVIEW OF BATTERY MODELS

A multitude of modeling approaches exist to describe the dynamic behavior of battery cells, modules, and complete battery systems. Apart from internal variables of the battery cell, such as concentrations, potentials, and temperatures, parameters that are of particular interest for monitoring, diagnostics, and optimal control include the battery state of charge (SoC) and state of health (SoH). The SoC relates the available capacity $[Ah]$ at a given time to the maximum available capacity[2] $[Ah]$:

$$SoC = \frac{C(t)}{C_{max}}. \tag{2.1}$$

[1] The mechanistic details affecting battery performance and degradation vary somewhat across active materials and electrolyte combinations and are therefore technology specific. However, the modeling approaches discussed in this chapter are generally applicable to intercalation-based LIBs and transferable to similar battery chemistries, such as Na-ion and K-ion batteries. Due to their great technical and economic importance, this chapter focuses on state-of-the-art LIBs with graphite (anode) and transition metal oxide (cathode) based active materials.

[2] The maximum capacity may refer either to the *nominal* or *theoretical* capacity. The *nominal* (or *rated*) capacity is the capacity that can be withdrawn, at a defined discharge rate, from a fully charged battery as specified by the battery manufacturer. By contrast, the theoretical capacity denotes the maximum capacity that can be stored, defined in terms of the number of lithium ions contained in the electrodes. Unlike the nominal capacity, the theoretical capacity typically differs somewhat across individual battery cells (or battery systems) of the same type due to small variations in the manufacturing process. Note that the theoretical capacity represents a thermodynamic upper limit that can typically not be attained under practical discharge rates. [22, 23]

By contrast, the SoH is used to express the degradation level of a battery by relating its maximum capacity to the maximum capacity of a new battery [18]:

$$SoH = \frac{C_{max}}{C_{max}(t=0)}. \tag{2.2}$$

A battery management system (BMS) is usually employed to monitor the status of the battery and to balance the charge and discharge currents of the battery cells. BMSs thus play an important role in ensuring the safe and reliable operation of the battery and avoiding extreme working states that would have a detrimental impact on the long-term performance and lifetime of the battery. The complexity of BMSs ranges from simple charging and discharging protocols to controllers that rely on sophisticated mathematical representations of the battery dynamics. Whereas relatively simple algorithms are currently employed in many industrial applications, advanced approaches that can more accurately represent the dynamics of the battery allow for more effective control, monitoring, and diagnostics. The further development and system integration of battery models therefore plays an integral part in improving the performance and longevity of today's batteries. [10, 18, 24]

Dynamic battery models can be roughly grouped into three categories: (i) physics-based models, (ii) equivalent circuit models, and (iii) data-driven models. Physics-based models are among the most detailed ones in that they are formulated in terms of partial differential equations (PDEs) for the conservation of mass, charge, and energy, as well as expressions for electrochemical reaction rates that account for the physical, electrical, and chemical phenomena in the battery. These models offer mechanistic understanding by describing interactions between different phenomena, such as electrochemical reactions and mass transport processes, or the consumption of lithium through electrolyte reduction at the surface of the anode, which leads to solid electrolyte interphase (SEI) growth and battery degradation. Physics-based models require a high number of material and system specific parameters, which poses a practical challenge, as many of these parameters may not be directly measurable during battery charge and discharge cycles. The parameterization of physics-based models therefore necessitates time-consuming experimental measurements and numerical analyses. In addition, physics-based models are typically based on coupled PDEs, which makes their numerical solution challenging and computationally expensive, especially in real-time and optimization settings. [10, 18, 24–26]

Equivalent circuit models map the ionic and electronic processes in the battery cell to a network of electric circuit components, mostly resistors and capacitors. Despite not being formulated in terms of PDEs for the dynamic processes, equivalent circuit models can be easily adjusted and in many cases reproduce the measured behavior of batteries reasonably well. [18, 24]

Data-driven models are conceptually different from the aforementioned ones in that they do not aim for a representation of the underlying physics but are constructed

solely based on experimental (or simulated [27]) data. Relying on techniques from time series analysis and machine learning, such as neuronal networks [27], random forests [28], and regularized regression techniques [29], data-driven models provide predictive relationships between pairs of input and output vectors. Data-driven approaches can potentially model complex relationships in nonlinear dynamic systems that are not sufficiently physically understood, such as the interplay of battery performance and degradation effects. [18, 27–30]

2.2 PSEUDO-TWO-DIMENSIONAL BATTERY CELL MODEL

The pseudo-two-dimensional (P2D) model is one of the most widely used physics-based electrochemical battery cell models. Based on porous electrode theory of de Levi [31] and further developed by Newman, Doyle, and coworkers [32, 33], it is mathematically represented by a system of coupled nonlinear PDEs for the conservation of mass and charge in the three main sections of the battery cell, i.e., cathode, separator, and anode. [24, 34] Figure 2.1 shows the schematic of a LIB cell in cross sectional view. The indices c, s, and a are used to denote the cathode, separator, and anode sections of the battery cell, respectively. The current collectors are denoted by y for the cathode and z for the anode. The notation $i \in \mathcal{S} := \{y,c,s,a,z\}$ is used to refer to a particular section of the battery cell. The thickness of each section is denoted by l_i, and the total thickness of the battery cell is $L = \sum_{i\in\mathcal{S}} l_i$. [24]

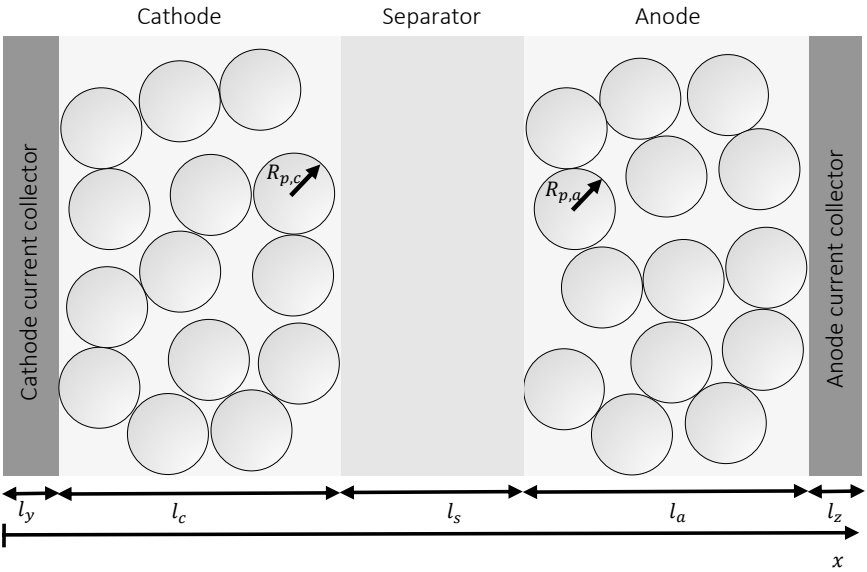

FIGURE 2.1: Schematic of a LIB cell in cross sectional view (figure redrawn based on Ref. [24]). The thickness of the different sections is denoted by l_y for the cathode current collector, l_c for the cathode, l_s for the separator, l_a for the anode, and l_z for the anode current collector. The radius of spherical active material particles is denotes by $R_{p,c}$ for the cathode and $R_{p,a}$ for the anode.

In porous electrode theory, transport is modeled via volume-averaged conservation equations [35]. Diffusion and conductivity coefficients that describe the average elec-

trolyte transport properties by accounting for the microscopic structure of the porous electrodes and separator are obtained as follows [36–38]:

$$D_{e,eff} = D_e \frac{\epsilon}{\tau}, \tag{2.3a}$$

$$\kappa_{e,eff} = \kappa_e \frac{\epsilon}{\tau}, \tag{2.3b}$$

where $D_{e,eff}$ and $\kappa_{e,eff}$ denote the *effective* diffusion and conductivity coefficient, respectively. By contrast, D_e and κ_e are the respective coefficients in pure electrolyte medium, while ϵ and τ denote the porosity and tortuosity, respectively, providing a macroscopic description of the porous medium microstructure. Porosity and tortuosity are related to each other via the Bruggeman equation [24, 34, 36, 37]:

$$\tau = \epsilon^{-\alpha}, \tag{2.4}$$

where the exponent $\alpha = 0.5$ for spherical solid phase particles.

Fick's laws of diffusion are differential equations relating the flux of a substance to its concentration as a function of location and time. The flux of lithium ions represents the number of lithium ions that pass a given location per unit time and area normal to the axis of diffusion. According to Fick's first law (eq. 2.5), the flux $F(x,t)$ $[mol/(m^2 s)]$ is proportional to the concentration gradient $(\partial c_e(x,t)/\partial x)$ that constitutes the driving force for the diffusion process:

$$F(x,t) = -D_e \cdot \frac{\partial c_e(x,t)}{\partial x}. \tag{2.5}$$

From eq. (2.5) follows Fick's second law of diffusion (eq. 2.6), which expresses the change in concentration of lithium ions over time [39]:

$$\frac{\partial c_e}{\partial t} = D_e \cdot \frac{\partial^2 c_e(x,t)}{\partial x^2}. \tag{2.6}$$

In the P2D model, conservation of mass in the electrolyte is described by eq. (2.7), which combines Fick's second law of diffusion with the flux density $j(x,t)$ $[mol/(m^2 s)]$ of lithium ions transferred between the electrolyte and solid phase:

$$\epsilon_i \frac{\partial c_e(x,t)}{\partial t} = \frac{\partial}{\partial x}\left[D_{e,eff,i} \cdot \frac{\partial c_e(x,t)}{\partial x}\right] + a_i(1-t_+)j(x,t), \quad i \in \{c,s,a\}, \tag{2.7}$$

where x is the spatial direction along which lithium ions are transported in the electrolyte phase of the porous medium (see figure 2.1), ϵ_i denotes the porosity, $D_{e,eff,i}$ is the effective diffusion coefficient (see eq. 2.3a), a_i is the specific interfacial area of the electrode (i.e., surface area of active material per unit volume of porous anode and cathode), and t_+ is the transference number. In the separator, the source term

$a_s(1-t_+)j(x,t)=0$, as no lithium ions are exchanged between the electrolyte and the solid phase (the separator contains no active material). [24, 34, 40, 41] Lithium ions are confined to within the cathode, separator, and anode sections of the battery cell, which is expressed by zero-flux boundary conditions at the cathode and anode side:

$$\left.\frac{\partial c_e(x,t)}{\partial x}\right|_{x=l_y} = \left.\frac{\partial c_e(x,t)}{\partial x}\right|_{x=l_y+l_c+l_s+l_a} = 0. \tag{2.8}$$

Continuity conditions apply at the cathode/separator (eq. 2.9a) and separator/anode (eq. 2.9b) boundaries [24, 34]:

$$-D_{e,eff,c}\cdot\left.\frac{\partial c_e(x,t)}{\partial x}\right|_{x=[l_y+l_c]^-} = -D_{e,eff,s}\cdot\left.\frac{\partial c_e(x,t)}{\partial x}\right|_{x=[l_y+l_c]^+}, \tag{2.9a}$$

$$-D_{e,eff,s}\cdot\left.\frac{\partial c_e(x,t)}{\partial x}\right|_{x=[l_y+l_c+l_s]^-} = -D_{e,eff,a}\cdot\left.\frac{\partial c_e(x,t)}{\partial x}\right|_{x=[l_y+l_c+l_s]^+}. \tag{2.9b}$$

Similarly to eq. (2.7), diffusion of lithium ions inside spherical solid phase material particles in the cathode and anode is governed by Fick's second law of diffusion. In spherical coordinates, the diffusion equation is as follows [34, 40]:

$$\frac{\partial c_s(r,t)}{\partial t} = \frac{1}{r^2}\frac{\partial}{\partial r}\left[r^2\cdot D_{s,i}\frac{\partial c_s(r,t)}{\partial r}\right], \qquad i\in\{c,a\}, \tag{2.10}$$

with boundary conditions

$$\left.\frac{\partial c_s(r,t)}{\partial r}\right|_{r=0} = 0, \tag{2.11a}$$

$$\left.\frac{\partial c_s(r,t)}{\partial r}\right|_{r=R_{p,i}} = -\frac{j(x,t)}{D_{s,i}}, \qquad i\in\{c,a\}, \tag{2.11b}$$

where r denotes the radial direction along which lithium ions diffuse within the solid phase material particles, $c_s(r,t)$ is the solid phase lithium ion concentration, $D_{s,i}$ is the diffusion coefficient in the solid phase, and $R_{p,i}$ is the radius of the particles. Consideration of the radial direction r introduces a second (pseudo) dimension, hence the name *P2D* model. [34, 40]

The conservation of charge in the solid phase of the cathode and anode sections is described by Ohm's law:

$$\frac{\partial}{\partial x}\left[\sigma_{eff,i}\cdot\frac{\partial}{\partial x}\Phi_s(x,t)\right] = a_i F j(x,t), \qquad i\in\{c,a\}, \tag{2.12}$$

where $\Phi_s(x,t)$ is the potential in the solid phase, F is the Faraday constant, and $\sigma_{eff,i}$ is the effective electronic conductivity of the electrodes, with $\sigma_{eff,i} = \sigma_i(1-\epsilon_i)$, where σ_i denotes the electronic conductivity of the (hypothetical) non-porous electrode, and ϵ_i is the porosity of the electrode. Boundary conditions eq. (2.13a) relate the solid phase potential to the applied current density $I_{app}(t)$ $[A/m^2]$, whereas the flux at the cathode/separator and separator/anode boundaries is zero (eq. 2.13b), as the entire current is carried by the ions [24, 41]:

$$\sigma_{eff,c} \cdot \frac{\partial \Phi_s(x,t)}{\partial x}\bigg|_{x=l_y} = \sigma_{eff,a} \cdot \frac{\partial \Phi_s(x,t)}{\partial x}\bigg|_{x=l_y+l_c+l_s+l_a} = -I_{app}(t), \tag{2.13a}$$

$$\frac{\partial \Phi_s(x,t)}{\partial x}\bigg|_{x=l_y+l_c} = \frac{\partial \Phi_s(x,t)}{\partial x}\bigg|_{x=l_y+l_c+l_s} = 0. \tag{2.13b}$$

A modified Ohm's law, which accounts for gradients of the lithium ion concentration, describes the conservation of charge in the electrolyte phase of the cathode, separator, and anode sections:

$$\begin{aligned} a_i F j(x,t) = &- \frac{\partial}{\partial x}\left[\kappa_{eff,i}(c_e) \cdot \frac{\partial}{\partial x}\Phi_e(x,t)\right] \\ &+ \frac{\partial}{\partial x}\left[\frac{2\kappa_{eff,i}(c_e)RT(x,t)}{F}(1-t_+)\frac{\partial}{\partial x} ln\, c_e(x,t)\right], \qquad i \in \{c,s,a\}, \end{aligned} \tag{2.14}$$

where $\kappa_{eff,i}(c_e)$ is the effective ionic conductivity[3] (see eq. 2.3b), $\Phi_e(x,t)$ is the potential in the electrolyte phase, R is the universal gas constant, and $T(x,t)$ is the temperature. As mentioned above, no lithium ions are exchanged between the electrolyte and solid phase in the separator, thus the source term $a_s F j(x,t) = 0$. Null flux boundary conditions apply at the cathode and anode side:

$$\frac{\partial \Phi_e(x,t)}{\partial x}\bigg|_{x=l_y} = \frac{\partial \Phi_e(x,t)}{\partial x}\bigg|_{x=l_y+l_c+l_s+l_a} = 0, \tag{2.15}$$

[3] Note that the ionic conductivity κ is typically modeled as a function of the lithium ion concentration c_e in the electrolyte, hence $\kappa = \kappa(c_e)$. In general, all three electrolyte transport parameters (i.e., diffusivity D_e, transference number t_+, and conductivity κ) are functions of both c_e and temperature T. Whereas the dependence on temperature is not considered for any parameter in isothermal P2D model formulations, the dependence on c_e is often neglected for D_e and t_+ and is therefore not indicated in the P2D model equations discussed in this chapter.

whereas continuity conditions apply at the cathode/separator and separator/anode boundaries:

$$-\kappa_{eff,c} \cdot \frac{\partial \Phi_e(x,t)}{\partial x}\bigg|_{x=[l_y+l_c]^-} = -\kappa_{eff,s} \cdot \frac{\partial \Phi_e(x,t)}{\partial x}\bigg|_{x=[l_y+l_c]^+}, \tag{2.16a}$$

$$-\kappa_{eff,s} \cdot \frac{\partial \Phi_e(x,t)}{\partial x}\bigg|_{x=[l_y+l_c+l_s]^-} = -\kappa_{eff,a} \cdot \frac{\partial \Phi_e(x,t)}{\partial x}\bigg|_{x=[l_y+l_c+l_s]^+}. \tag{2.16b}$$

Without loss of generality, Φ_e can be set to zero at the end of the anode in the P2D model formulation because only potential *differences* are measurable [24, 34, 41]:

$$\Phi_e(x,t)\Big|_{x=l_y+l_c+l_s+l_a} = 0. \tag{2.17}$$

In order to account for heat generation during battery charging and discharging, the P2D model may be extended by additional conservation equations that describe the thermal dynamics inside the battery cell. The interested reader is referred to *Torchio et al. 2016* [34] for the details.

Charge transfer kinetics at the electrode/electrolyte interface[4] is governed by Butler-Volmer kinetics (eq. 2.18), which expresses the ionic flux density $j(x,t)$ as a function of the overpotential $\eta_i(x,t)$ [24, 33, 34, 42]:

$$j(x,t) = \frac{2 \cdot i_{i,0}(c_s, c_e)}{F} \cdot sinh\left[\frac{0.5F}{RT(x,t)}\eta_i(x,t)\right], \qquad i \in \{c,a\}, \tag{2.18}$$

where $i_{i,0}(c_s, c_e)$ denotes the exchange current density. The overpotential $\eta_i(x,t)$ is defined by the solid phase potential $\Phi_s(x,t)$, electrolyte phase potential $\Phi_e(x,t)$, and open circuit potential $U_i(x,t)$:

$$\eta_i(x,t) = \Phi_s(x,t) - \Phi_e(x,t) - U_i(x,t), \qquad i \in \{c,a\}. \tag{2.19}$$

The open circuit potential $U_i(x,t)$ is a characteristic of the chemical composition of the electrodes and dependent on their lithiation state [42], which changes as the battery cell charges and discharges. The exchange current density $i_{i,0}$ is given as follows:

$$i_{i,0} = Fk_i\Big\{c_e(x,t) \cdot \big(c_{s,i}^{max} - c_s(R_{p,i},t)\big) \cdot c_s(R_{p,i},t)\Big\}^{0.5}, \qquad i \in \{c,a\}, \tag{2.20}$$

where k_i is a kinetic reaction rate constant, and $c_{s,i}^{max}$ denotes the maximum lithium ion concentration in the active material phase.

[4] The term *interface* (instead of *interphase*) is used here, as the interphase layer is typically not explicitly modeled in the P2D model.

The battery cell voltage corresponds to the difference between the solid phase potential at the cathode and anode current collector [41, 42]:

$$V(t) = \Phi_s(l_y, t) - \Phi_s(l_y + l_c + l_s + l_a, t). \tag{2.21}$$

The P2D model discussed above[5] consists of two PDEs (eq. 2.7 and eq. 2.10), two ordinary differential equations (ODEs) in space (eq. 2.12 and eq. 2.14), and one coupling algebraic equation (eq. 2.18). This system of equations can be solved using numerical methods, such as the finite difference method (FDM) or finite volume method (FVM). [34, 41]

[5]Some P2D model formulations include additional equations to model the thermal dynamics and additional phenomena, such as electrochemical double layer effects [34, 42].

2.3 BATTERY DEGRADATION

As batteries degrade with both time and use, their energy storage and power supply capabilities decrease until they no longer meet the requirements for the designated application. Accurate methods to monitor and control the battery degradation level (and associated decrease in *SoH* and increase in internal resistance) therefore play a vital role in ensuring its reliable operation. Models that formulate degradation as a function of battery operation can be roughly grouped into three categories: (i) physics-based models, (ii) semi-empirical models, and (iii) data-driven models. [10, 11, 29] This chapter starts by reviewing the main ageing processes in LIBs with graphite (anode) and transition metal oxide (cathode) based active materials. Then, different approaches are discussed to mathematically describe these processes, including physics-based models (chapter 2.3.2), semi-empirical models (chapter 2.3.3), and data-driven models (chapter 2.3.4).

2.3.1 *Ageing processes in lithium-ion batteries*

i.) Anode degradation

The main degradation mechanisms at the anode side include SEI formation, metallic lithium plating, and loss of active material.
Since lithiated carbon is not stable in air, LIB cells are assembled in their discharged state. Upon initial charging, lithium ions from the cathode along with organic compounds from the electrolyte solution react with the graphite anode, thereby forming an SEI layer with a thickness ranging from less than one up to tens of nanometers [43]. SEI formation irreversibly consumes lithium coming from the cathode, thereby reducing the amount of lithium available for cycling, resulting in lower battery capacity. Approximately 10% of the capacity is consumed during the first few cycles by irreversible SEI formation. The SEI is electrically insulating, ionically conducting, and ideally protects the anode from further reactions with the solvent. These properties make the SEI a vital component for good battery performance. [44, 45] Over time, the SEI layer slowly corrodes, which exposes the graphite anode to the electrolyte, leading to additional SEI growth and consequently, capacity loss and resistance increase. Elevated temperatures accelerate the dissolution rate. Upon charging and discharging, the graphite structure is lithiated and de-lithiated, which causes volume changes of approximately 10% in the c-direction of the crystallites. [44, 46–49] The resulting mechanical stress can lead to graphite exfoliation via particle cracking. This decreases the amount of available active material and creates additional surfaces for SEI growth. When a battery is stored at high SoC level, the anode is highly lithiated (i.e., at low potential) and lithium deposition on the anode becomes eventually thermodynamically possible for unbalanced cells. In this case, lithium ions are deposited on the anode surface as metallic lithium during charging instead of being intercalated into the anode. High charge rates can

additionally induce lithium plating if the diffusion of lithium ions into the graphite structure is slow. At low temperatures, the rate of diffusion is reduced, which favors lithium plating and dendrite growth. [44]

ii.) Cathode degradation

There is greater variation in cathode degradation, as ageing is highly material dependent and because there exists a wide variety of cathode materials in today's LIBs [44, 50]. The main degradation mechanisms include loss of active material and growth of the cathode surface film [44].
Loss of active material occurs when transition metals (Ni, Mn, Co, Fe) contained in the cathode structure dissolve in the electrolyte. This process is generally accelerated at high temperatures and high SoC levels. [44, 51, 52]
Like the anode, the cathode is covered by a surface film, referred to as *solid permeable interface* [53, 54], which, however, is much thinner than the SEI on the anode side. Charging and discharging leads to volume changes and mechanical stress, which can cause cracking, thereby creating additional surfaces for cathode/electrolyte reactions. [44, 50]
Cracking can also be caused by gas generation due to oxygen loss from the transition metal oxide structure at high temperatures or from electrolyte decomposition at high SoC levels. At higher temperatures (150 °C to 310 °C, depending on the material composition), the cathode itself can decompose, which leads to loss of active material, gas release, and thermal runaway. [44, 55]

iii.) Inactive material degradation

Inactive battery cell components, including binder materials contained in the anode and cathode, current collectors, and separator, are also subject to degradation. Binder materials can disintegrate at high temperatures or voltages, while current collectors may corrode when exposed to the electrolyte and high potentials. The separator is susceptible to mechanical damage due to dendrite growth, which in the worst case leads to internal short-circuits. [44, 50]

2.3.2 *Physics-based degradation models*

Physics-based degradation models are formulated in terms of PDEs for the conservation of mass, charge, and energy and provide a detailed mechanistic description of the ageing processes in the battery cell. These models are typically derived as an extension of *P2D* and related physics-based performance models by including additional equations for chemical side reactions and material fatigue processes. [10, 11, 18, 34, 56, 57]

2.3.3 *Semi-empirical degradation models*

2.3.3.1 *Degradation stress factors*

Semi-empirical models describe the ageing processes in battery cells on a macroscopic level by assuming that degradation is caused by a set of stress factors that can be described through parametric stress models derived from experimental ageing tests. Two ageing modes are commonly distinguished: calendar ageing, which occurs over time when the battery is disconnected from any load, and cycle ageing due to repeated charging and discharging. In the following, the main stress factors in today's LIBs are reviewed, including (i) depth of discharge (DoD), (ii) SoC level, (iii) charge and discharge rate, and (iv) temperature. [11, 46, 47, 51, 53, 58–63]

i.) DoD

Depth of discharge (DoD) is an important stress factor affecting battery lifetime: Experimental degradation tests on LIB cells with lithium nickel manganese cobalt oxide (NMC) cathodes have revealed a strong impact of DoD on cycle ageing [64, 65]. For instance, Ecker, Schmalstieg, and coworkers [47, 53] found a roughly quadratic relationship between DoD and ageing, which translates into 100 times more cycles (and thus a ten-fold higher lifetime energy throughput) for batteries exposed to shallow cycles (10% DoD) than for batteries exposed to full cycles (100% DoD). [47, 53, 63] LIB cells with lithium iron phosphate (LFP) cathodes are generally less affected by deep cycles, and the incurred ageing scales approximately linearly with DoD, giving rise to a cycle lifetime that corresponds to a fixed energy throughput. [66–68] Figure 2.2 shows Wöhler curves for LFP/Graphite and NMC/Graphite LIBs, describing the relationship between DoD and the number of cycles until they reach the end of their lifetime [7, 53, 66].

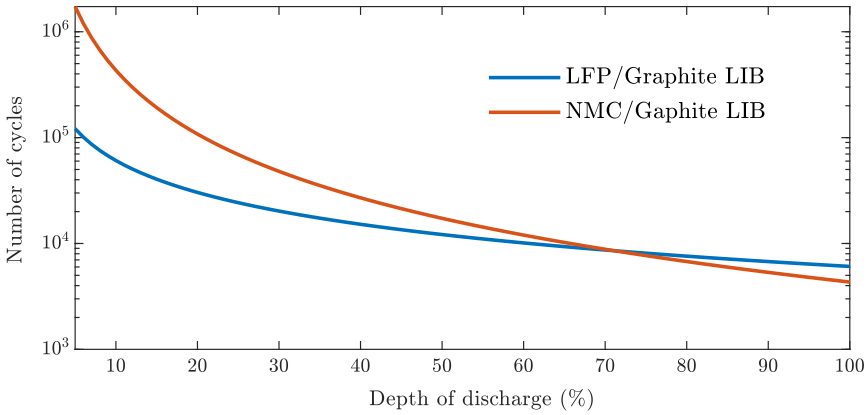

FIGURE 2.2: Wöhler curves for lithium iron phosphate vs. graphite (LFP/Graphite) and lithium nickel manganese cobalt oxide vs. graphite (NMC/Graphite) LIBs. The figure was created based on data provided in Refs. [7, 53, 66].

ii.) SoC level

Low and, in particular, high SoC levels have a detrimental impact on the calendar lifetime of batteries [44, 46, 50, 53]. In practical applications, over-charging and over-discharging are avoided by the BMS by enforcing lower and upper limits on the SoC level [63]. For cycle ageing, the impact of the SoC level has been found to be lowest for cycles centered at around 50% SoC [53, 61].

iii.) Charge and discharge rate

High charge and discharge currents accelerate the rate of battery degradation. This effect is amplified at low temperatures or if the excess heat generated at high rates cannot be sufficiently dissipated by the battery cooling system. [11, 44, 50, 59–64] The detrimental impact of high rates is generally less critical in stationary battery systems than in mobile applications due to moderate power rates (below $1\text{-}2\,MW/MWh$[6] in many cases) and temperature-controlled storage conditions.

iv.) Temperature

Elevated temperatures accelerate the rate of battery degradation, while high current rates at low temperatures can also increase cycle ageing. In stationary battery systems, temperature has generally a limited impact on battery lifetime due to temperature-

[6]The charge/discharge rate of a battery is often expressed in terms of the *C-rate*, which specifies the inverse time in hours for full charge or discharge. Hence, power rates of $1\text{-}2\,MW/MWh$ (charge or discharge in 0.5 - 1 hours) correspond to C-rates of 1 - 2. [22]

controlled storage conditions. [11, 44, 50, 59–61, 64]

2.3.3.2 *Parametric stress models*

A multitude of models have been developed to describe the interactions between different stress factors and to assess the combined impact of cycle and calendar ageing processes on battery degradation [11, 51, 69–71].

Xu et al. [11] developed a superposition-based approach in which battery degradation is modeled as the sum of calendar and cycle ageing:

$$L_{tot} = L_{cal} + L_{cyc}, \tag{2.22}$$

where L_{tot} denotes the total degradation incurring over a period of time, while L_{cal} and L_{cyc} denote degradation due to calendar and cycle ageing, respectively. The rate of calendar ageing is affected by the temperature and SoC level. Calendar ageing L_{cal} over a period of time t can therefore be expressed as a function of the elapsed time (t), average cell temperature ($\overline{T}$), and average SoC level ($\overline{\sigma}$) [11]:

$$L_{cal} = f_{cal}(t, \overline{T}, \overline{\sigma}). \tag{2.23}$$

The rate of cycle ageing is dependent on the number of cycles Z as well as the average SoC level (σ_c), depth of discharge (δ_c), current rate (r_c) [62], and average temperature T_c during each cycle. Cycle ageing L_{cyc} can therefore be expressed as follows [11]:

$$L_{cyc} = \sum_{c}^{Z} n_c \cdot f_{cyc}(\sigma_c, \delta_c, r_c, T_c), \tag{2.24}$$

where n_c indicates whether cycle c is a full ($n_c = 1$) or a half ($n_c = 0.5$) cycle. In eq. (2.24) every cycle is modeled as a single, independent stress event. This modeling approach assumes that battery degradation is a Markov process, that is, degradation is dependent only on the current battery state (i.e., degradation level) and operation of the battery during the considered time period and not on the degradation history of the battery. [11, 72]

The degradation model described by eq. (2.22) - (2.24) implies that the rate of degradation is the same as long as the operation of the battery does not change. This behavior, however, is typically not observed in battery ageing tests: The degradation rate of LIBs is not a linear process, neither with respect to time (calendar ageing) nor with the number of cycles (cycle ageing). Experimental studies have found higher degradation rates in new batteries (SoH: 100%) than in batteries at intermediate degradation levels (SoH: ca. 80 - 95%), followed by a rapid increase of the degradation rate once the

battery reaches the end of its lifetime (SoH: ca. 70 - 80%). [11, 46, 47, 69, 73, 74] The relationship between the degradation level SoH, which is of practical interest, and the degradation L_{tot}, computed by linearly aggregating ageing contributions according to eq. (2.22) - (2.24), can be modeled using power-law expressions [47, 69, 74]:

$$SoH = \left(1 - \alpha \cdot L_{tot}^{\beta}\right) \cdot 100\%, \tag{2.25}$$

where α and β are empirical fitting parameters. Note that for $\beta \in (0,1)$, degradation proceeds faster at the beginning (i.e., in the new battery) than at subsequent stages of the degradation trajectory. In LIBs, β typically takes a value between 0.5 and 1. [47, 69, 74]

Despite the widespread use of superposition-based models ($L_{tot} = L_{cal} + L_{cyc}$) described by eq. (2.22) [11, 47, 60], some battery degradation studies assume multiplicative ($L_{tot} = L_{cal} \cdot L_{cyc}$) [59] or maximum-based ($L_{tot} = max\{L_{cal}, L_{cyc}\}$) [7, 75, 76] functional relationships between calendar and cycle ageing modes. Overall, the large variety of degradation models indicates the further need for experimental ageing studies to parameterize models that generalize well to a wide range of battery chemistries and operation conditions.

2.3.3.3 *Cycle counting*

Cycle ageing L_{cyc} scales with the number of cycles as shown in eq. (2.24). Thus, cycle ageing can be assessed by counting the number of cycles normalized to reference conditions:

$$N_c^{ref} = \frac{n_c \cdot f_{cyc}(\sigma_c, \delta_c, r_c, T_c)}{f_{cyc}(\sigma_{ref}, \delta_{ref}, r_{ref}, T_{ref})}, \tag{2.26a}$$

$$N^{ref} = \sum_{c}^{Z} N_c^{ref}. \tag{2.26b}$$

In eq. (2.26a) cycle ageing during each cycle c is converted to the number of equivalent cycles N_c^{ref} by applying the normalization factor $f_{cyc}(\sigma_{ref}, \delta_{ref}, r_{ref}, T_{ref})$, which corresponds to the ageing during one full cycle under reference conditions. In eq. (2.26b) total cycle ageing is computed by summing up the ageing during each cycle. As it is common practice for battery manufacturers to provide estimates on the number of charge and discharge cycles until battery end of life, the ageing model described by eq. (2.26a) - (2.26b) allows for a direct assessment of the remaining cycle lifetime.[7] [7, 23]

[7] Whereas the cycle ageing model described by eq. (2.26a) - (2.26b) is mathematically equivalent to the one described by eq. (2.24), the former can more easily be parameterized using battery lifetime data provided in warranty sheets.

The SoC profile resulting from irregular battery operation typically consists of superimposed cycles with different cycle parameters, such as depth of discharge (δ_c) and average SoC level (σ_c). This impedes the direct assessment of cycle ageing from the SoC profile. Degradation models therefore rely on procedures that decompose the SoC profile into individual charge and discharge cycles that can be processed individually by applying eq. (2.26a) - (2.26b). The Rainflow cycle counting algorithm provides a method for time series decomposition. The algorithm takes an arbitrary SoC profile as input, decomposes the profile into individual charge and discharge cycles, and outputs the parameters of each cycle [11, 77]:

$$(\boldsymbol{\delta}, \boldsymbol{\sigma}, \mathbf{n}) = Rainflow(\mathbf{SoC}), \tag{2.27}$$

where $\boldsymbol{\delta}$, $\boldsymbol{\sigma}$ and $\mathbf{n}$ are vectors of length Z indicating the depth of discharge (δ_c), average SoC level (σ_c), and cycle count ($n_c \in \{0.5, 1\}$), respectively, of each cycle c identified by the algorithm. For a time horizon with T time steps, $\mathbf{SoC}$ is a vector of length $T+1$ (including $SoC_{t=0}$).

2.3.3.4 *Rainflow algorithm*

The Rainflow cycle counting algorithm (eq. 2.27) was originally proposed for material fatigue analysis [78–80] and has more recently been implemented in degradation models for battery lifetime assessment [58, 77, 81–84]. The algorithm is an iterative procedure that operates on a state of charge profile $\mathbf{SoC} \in \mathbb{R}^{T+1}$ and outputs a set of cycle parameters $\boldsymbol{\delta} \in \mathbb{R}^Z$, $\boldsymbol{\sigma} \in \mathbb{R}^Z$, and $\mathbf{n} \in \mathbb{R}^Z$. *Algorithm 1* details the Rainflow algorithm, while figure 2.3 and table 2.1 provide an example to illustrate the cycle counting procedure.

Algorithm 1: Rainflow cycle counting algorithm (adapted from Refs. [63, 77, 81])

Input: State of charge profile $\mathbf{SoC} \in \mathbb{R}^{T+1}$.

Output: Vectors of cycle parameters: depth of discharge $\boldsymbol{\delta} \in \mathbb{R}^{Z}$, average SoC level $\boldsymbol{\sigma} \in \mathbb{R}^{Z}$, and cycle count $\mathbf{n} \in \mathbb{R}^{Z}$, where Z denotes the number of cycles identified by the Rainflow algorithm.

Step 1 *Local extrema.* Find the vector of local extrema $\mathbf{y} = [y_1, y_2, \ldots, y_K]$ in the order of their occurrence in the state of charge profile. Local extrema correspond to transitions between battery charging and discharging.

Step 2 *Rainflow counting.*

- $k \leftarrow 1$ // start at first local extremum
- $K \leftarrow |\mathbf{y}|$ // set K to the length of the vector $\mathbf{y}$
- ***while*** $k \leq K - 3$ ***do***

  // compute amplitudes:
  - $\Delta y_1 = |y_k - y_{k+1}|, \quad \Delta y_2 = |y_{k+1} - y_{k+2}|, \quad \Delta y_3 = |y_{k+2} - y_{k+3}|$
  - ***if*** $\Delta y_2 \leq \Delta y_1$ ***and*** $\Delta y_2 \leq \Delta y_3$
    - count the cycle associated with y_{k+2} and y_{k+1} as a full cycle with depth of discharge $\delta = \Delta y_2$ and average SoC level $\sigma = (y_{k+2} + y_{k+1})/2$
    - the two parts of the time series are joined together by removing y_{k+2} and y_{k+1} and setting $y_{k+2} = y_k$
    - $k \leftarrow k + 2$ // move forward in time series
  - ***else***
    - $k \leftarrow k + 1$ // move forward in time series

Step 3 *Repeat counting.* Step 2 is repeated until no more full cycles are identified. Note that the length of the vector of local extrema ($\mathbf{y}$) decreases as more full cycles are identified in Step 2.

Step 4 *Treatment of residue.* The residue time series is treated by counting every two consecutive points as a half cycle.

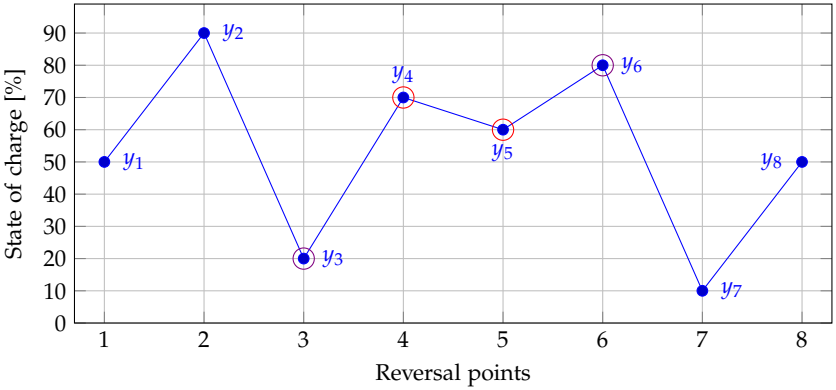

FIGURE 2.3: Illustration of a SoC profile with reversal points (local extrema) $y_1, y_2, \ldots, y_8$. The Rainflow algorithm identifies two full cycles between y_4 and y_5 (marked in red) and between y_3 and y_6 (marked in violet) as well as three half cycles.

TABLE 2.1: Output of the Rainflow algorithm for the SoC profile shown in figure 2.3. The following parameters are obtained for each cycle: cycle count (n_c), depth of discharge (δ_c), average SoC level (σ_c), and start and end points of each cycle.

cycle index (c)	n_c	δ_c	σ_c	start	end
1	1	10%	65%	y_4	y_5
2	1	60%	50%	y_3	y_6
3	0.5	40%	70%	y_1	y_2
4	0.5	80%	50%	y_2	y_7
5	0.5	40%	30%	y_7	y_8

2.3.4 *Data-driven degradation models*

In the past years, data-driven machine learning has emerged as an alternative modeling approach to determine and predict key variables of LIBs, such as SoC, SoH, and the remaining useful life. Whereas physics-based and semi-empirical degradation models assume functional relationships between input and output variables based on the battery dynamics, data-driven models employ fitting functions without consideration of the underlying physics. The ability of machine learning and deep learning algorithms to learn patterns and predictive relationships from data without explicitly being programmed, makes data-driven modeling a promising technique, especially when extensive amounts of experimental data are available for model training. [18, 29, 85–88] The main drawbacks of data-driven models are that they offer limited mechanistic insights and that they generally need to be re-trained when used in another application setting [18].

3

BATTERY CELL ASSESSMENT

This chapter presents a modeling framework for the technical, economic, and environmental assessment of battery cells. In a first step, the physics-based electrochemical P2D model is used to project practical specific energies of intercalation-based battery cells exposed to varying discharge rates. The derived performance parameters are subsequently used to parameterize a bottom-up battery cell costs model and to assess life cycle greenhouse gas (GHG) emissions. Overall, the modeling framework allows for a holistic assessment of key parameters that determine the future potential of both current and new battery technologies. This chapter starts with a brief comparison of lithium-ion batteries (LIBs) and sodium-ion (Na^+) batteries (NIBs). Then, the modeling framework is introduced, along with a critical discussion of the parameterization of the P2D model. Serving as a validation and case study for the developed framework, the chapter concludes with a comparative assessment of LIBs and NIBs. Based on the model results, guidelines and recommendations are suggested for future research on NIBs.

The content of this chapter has been published by **S. F. Schneider**, C. Bauer, P. Novák, and E. J. Berg, *Sustainable Energy & Fuels*, 2019, 3, 3061-3070 [89].

3.1 LITHIUM-ION AND SODIUM-ION BATTERIES

Their unmatched specific energy and reliable operation makes LIBs one of the most advanced battery technologies, which is reflected in the worldwide LIB market size of $37 billion in 2019 [6]. Due to rising concerns regarding the future costs and availability of lithium raw materials, NIBs are frequently discussed as a promising low-cost and environmentally more benign alternative to eventually complement LIBs. [90–93] Based on the larger size of Na^+ charge carriers compared to their Li^+ counterparts and the less negative standard potential ($E^0(Na^+/Na) = -2.71\,V$ (Ref. [94]) vs. $E^0(Li^+/Li) = -3.04\,V$ (Ref. [94])) of the governing electrochemical reaction, it is often argued that NIBs are not likely to be competitive with LIBs in terms of specific energy. Whereas such considerations inherent to the thermodynamic properties of a battery chemistry are relevant when assessing theoretical specific energies [15], it is often overlooked that the larger size of Na^+ charge carriers favors enhanced electrolyte mass transport [95] and faster reaction kinetics [95–98] at the electrode/electrolyte interface.

Aiming for a better understanding of the trade-offs existing between thermodynamic and kinetic parameters in LIB and NIB cells, this chapter presents a modeling framework to assess practical specific energies of LIB and NIB cells exposed to varying discharge rates. Based on this framework, the costs and manufacturing-related environmental impacts of LIB and NIB cells are quantified from a life cycle perspective.

State-of-the-art modeling approaches for battery cell assessment include the Argonne National Laboratory Battery Performance and Cost (BatPaC) model [99], the TIAX model [100], the simplified Energy-Cost model by Berg et al. [101], and other [19, 102, 103] valuable studies evaluating performance and costs. Many of these contributions enjoy widespread appreciation in both academia and industry, as they help to uncover trade-offs existing between competing battery chemistries, and because they can provide guidelines to improve the design of battery cells. More recently, comparative studies have been performed to assess costs [13] and environmental impacts [91] of LIBs and NIBs. A common short-coming of the above-discussed modeling approaches is that they typically rely on generic battery performance assumptions, e.g., in terms of constraints imposed on battery cell design to meet discharge power requirements instead of performance metrics derived from detailed physics-based models. Therefore, these models are not suited to study the impact of fundamental thermodynamic and kinetic parameters on the performance of different battery technologies. In the following, this research gap is addressed by integrating the P2D battery cell model [34] into a modeling framework that allows for a consistent assessment of specific energies, costs, and manufacturing-related GHG emissions of LIB and NIB cells. To evaluate the impact of faster kinetics in NIBs, the performance projections are performed for LIB and NIB cells exposed to varying discharge rates. Overall, the presented modeling framework helps to pinpoint key parameters governing the technical, economic, and environmental viability of LIB and NIB cells.

3.2 MODELING FRAMEWORK

3.2.1 *Overview*

Figure 3.1 summarizes the modeling framework developed in this study to assess performance, costs, and environmental impacts of LIB and NIB cells. In a first step, the P2D battery cell model is employed to project practical specific energies of LIB and NIB cells exposed to varying discharge rates. In a second step, the P2D model output, i.e., battery cell performance and material requirements for battery cell manufacturing, enables the parameterization of a bottom-up cost model and life cycle inventories. In a third step, battery cell manufacturing costs are computed, and life cycle assessment (LCA) is performed to quantify manufacturing-related GHG emissions. The es-

tablished modeling framework was used to assess NIB cells with the active material configuration $NaNi_{1/3}Co_{1/3}Mn_{1/3}O_2$ (cathode) vs. hard carbon (anode). The results of the assessment were compared against model results obtained for their state-of-the-art LIB analogue with the configuration $LiNi_{1/3}Co_{1/3}Mn_{1/3}O_2$ (cathode) vs. graphite (anode).

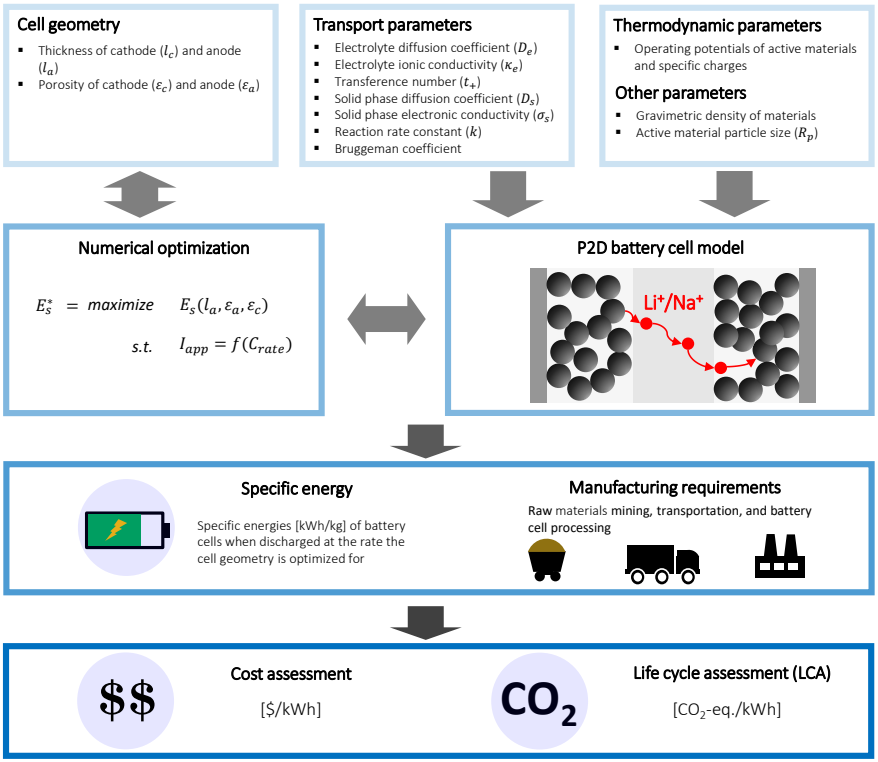

FIGURE 3.1: Modeling framework for battery cell assessment. Practical specific energies and battery cell manufacturing requirements derived using the P2D model constitute the input for the assessment of costs and GHG emissions. All calculations are performed on the battery cell level.

Whereas the further advancement of LIBs has received significant attention from academia and industry since their commercialization by Sony ca. 30 years ago, NIBs are currently a less mature technology in their prototyping stage. [5] It is therefore expected that ongoing research activities will eventually lead to the development of NIB active materials offering both higher voltage and higher specific charges than NIB active materials available today. Therefore, a second assessment was performed, which is intended to be unaffected by the different development stages of the two technologies. The assessment is representative of a hypothetical scenario where

differences in battery performance originate solely from fundamental thermodynamic and kinetic disparities inherent to LIBs and NIBs. For this scenario, NIB active materials are considered that display the same specific charges and gravimetric densities as $LiNi_{1/3}Co_{1/3}Mn_{1/3}O_2$ and graphite. Furthermore, it is assumed that the lower voltage in NIB cells compared to LIB cells amounts only to the difference in the electrochemical standard potentials, i.e., $0.33\,V$. Although this value refers to the difference in the reduction potentials for lithium and sodium in aqueous electrolyte, it is in agreement with first principles calculations that predict a voltage difference of $0.18 - 0.57\,V$ for different Li-ion and Na-ion based intercalation chemistries [104].

The remainder of this chapter is organized as follows: Chapter 3.2.2 provides an overview and critical discussion of input parameters for the P2D model. In chapter 3.2.3, the life cycle inventories collected for LIB and NIB cells are presented, along with a discussion of the empirical bottom-up battery cell cost model adapted from Patry et al. [19] and Berckmans et al. [105].

3.2.2 *Pseudo-two-dimensional model*

The P2D battery cell model has repeatedly proven to be suitable to accurately simulate the discharge behavior of battery cells and to optimize their design [25, 34, 42]. For a detailed review of the P2D model, the interested reader is referred to chapter 2.2 of this thesis.

In the following, the numerical implementation of the P2D model in MATLAB developed by Torchio et al. [34] is used to project practical specific energies of LIB and NIB cells exposed to discharge rates of $0.25\,C$, $4\,C$, and $10\,C$. Current densities associated with these discharge rates were defined as the ratio of the theoretical specific charges of active materials and the duration of full galvanostatic discharge, i.e., $4\,h$, $15\,min$, and $6\,min$. Table 3.1 shows selected input parameters for the P2D model. A complete list of model parameters is provided in table A1 in the appendix. As discussed above, two distinct active material configurations are considered for the NIB, denoted as the *present* scenario ($NaNi_{1/3}Co_{1/3}Mn_{1/3}O_2$ and hard carbon active materials), referring to the present state of development, and the *hypothetical* (yet unknown active materials) scenario. The hypothetical scenario is intended to be representative of the cell performance of NIBs that have enjoyed the same cumulative research and development efforts as LIBs today. Whereas a comparison of such hypothetical NIBs with current LIBs is not supposed to represent a comparison of future cells (since LIBs will also undergo further development), it allows the evaluation of achievable development goals for NIBs in terms of performance.

In order to account for uncertainties in the kinetic parameters that exist for NIBs because of limited experimental data availability, three different sub-scenarios are considered for each active material configuration, referred to as *pessimistic*, *base*, and *optimistic*. The resulting six NIB parameter sets correspond to six different types of NIB cells. Kinetic parameters in the electrode materials (i.e., solid phase diffusion coefficients and electronic conductivities) are not listed in table 3.1, as they are assumed to be identical for NIB and LIB cells. A comprehensive discussion of the P2D model parameters is provided in chapter A.1 in the appendix. Compared to kinetic and thermodynamic input parameters, which are an intrinsic property of the active materials, electrolyte solution, and other constituents of the battery cell, cell design parameters (i.e., electrode thickness and electrode porosity) can be chosen by battery manufactures such as to best match the technical requirements of the battery. In this regard, one may distinguish between *high energy* cells with thick electrodes and low electrode porosity and *high power* cells with thin electrodes and high electrode porosity. Whereas *high energy* cells have higher theoretical specific energy, they show inferior performance in high-power applications compared to *high power* cells, which retain a larger fraction of their theoretical specific energy when exposed to fast discharge. The optimal battery cell design is not only dependent on the anticipated discharge rate but also on the battery chemistry. The optimal set of design parameters is thus not *ex ante* known. For this reason, the P2D model was coupled to an optimization solver to numerically optimize the cell design parameters for maximum practical specific energy at the different discharge rates. Formally, the optimization of the battery cell design can be stated as follows:

$$
\begin{aligned}
E_s^* \quad = \quad & \\
& \underset{l_a,\epsilon_a,\epsilon_c}{\text{maximize}} \quad E_s(l_a,\epsilon_a,\epsilon_c), && \text{(3.1a)}\\
& \text{s.t.} \quad I_{app} \;=\; f(C_{rate}), && \text{(3.1b)}\\
& \qquad\quad \mathbf{b}_l \;\leq\; [l_a,\epsilon_a,\epsilon_c]^T \;\leq\; \mathbf{b}_u, && \text{(3.1c)}
\end{aligned}
$$

where the practical specific energy (E_s) is maximized in the objective function (3.1a), I_{app} is the applied current density (defined in terms of the *C-rate*), and $\mathbf{b}_l$ and $\mathbf{b}_u$ denote lower and upper bounds on the battery cell design parameters, respectively. The practical specific energy (E_s) is evaluated using the P2D model. It is dependent on the thickness of the anode (l_a), the porosity of the anode (ϵ_a), and the porosity of the cathode (ϵ_c). Notably, the objective function (3.1a) is *not* dependent on the thickness of the cathode (l_c). This is because balanced capacities are assumed for the anode and

cathode, hence the four cell design parameters l_a, l_c, ϵ_a, and ϵ_c are not independent. The thickness of the cathode (l_c) can be computed as follows:

$$l_c = l_a \cdot \frac{c_{s,a}^{max}}{c_{s,c}^{max} - c_{s,c}^{init}} \cdot \frac{1 - \epsilon_a - \epsilon_{f,a}}{1 - \epsilon_c - \epsilon_{f,c}}, \tag{3.2a}$$

where $c_{s,a}^{max}$ and $c_{s,c}^{max}$ are the maximum solid phase Li^+ or Na^+ concentration in the anode and cathode active material, respectively, $c_{s,c}^{init}$ is the initial solid phase Li^+ or Na^+ concentration in the cathode active material, and $\epsilon_{f,a}$ and $\epsilon_{f,c}$ denote the filler fraction in the anode and cathode, respectively (see table A1 in the appendix for the details).

It should be noted that the objective function (3.1a) is nonsmooth and typically nonconvex, which the optimization solver should be able to handle. Previous studies have relied either on derivative-based local solvers [102, 106] or derivative-free global approaches [102, 107] to tackle the challenge of optimizing battery cell geometry. In this thesis work, the *fmincon* interior-point solver from the MATLAB optimization toolbox [108] was used. The solver was run from 500 randomly selected starting points to ensure (near-)global optimality of the solution. In addition, particle swarm optimization from the MATLAB optimization toolbox [109] was used. Whereas similar results were obtained employing the two solvers, particle swarm optimization was more effective in terms of the number of required objective function evaluations.

TABLE 3.1: Scenarios for LIB and NIB cells and P2D model parameters collected from Refs. [38, 42, 96–98, 110–113]. A complete list of model parameters is provided in table A.1 in the appendix.

Scenario label	LIB	NIB present base	NIB present optimistic	NIB present pessimistic	NIB hypothetical base	NIB hypothetical optimistic	NIB hypothetical pessimistic
Electrolyte conductivity (κ_e)	$f(c_e)$	$1.2 \cdot \kappa_e^{LIB}$	$1.5 \cdot \kappa_e^{LIB}$	$1.0 \cdot \kappa_e^{LIB}$	$1.2 \cdot \kappa_e^{LIB}$	$1.5 \cdot \kappa_e^{LIB}$	$1.0 \cdot \kappa_e^{LIB}$
Electrolyte diffusivity (D_e)	$3 \cdot 10^{-10}\, m^2\, s^{-1}$	$1.28 \cdot D_e^{LIB}$	$2.00 \cdot D_e^{LIB}$	$1.00 \cdot D_e^{LIB}$	$1.28 \cdot D_e^{LIB}$	$2.00 \cdot D_e^{LIB}$	$1.00 \cdot D_e^{LIB}$
Transference number (t_+)	0.4	0.5	0.5	0.4	0.5	0.5	0.4
Reaction rate constant (k)	$2 \cdot 10^{-11}\, m^{2.5}\, mol^{-0.5}\, s^{-1}$	$10^2 \cdot k^{LIB}$	$10^3 \cdot k^{LIB}$	$1 \cdot k^{LIB}$	$10^2 \cdot k^{LIB}$	$10^3 \cdot k^{LIB}$	$1 \cdot k^{LIB}$
Specific charge anode	$372\, Ah kg^{-1}$	$329\, Ah kg^{-1}$	$329\, Ah kg^{-1}$	$329\, Ah kg^{-1}$	$372\, Ah kg^{-1}$	$372\, Ah kg^{-1}$	$372\, Ah kg^{-1}$
Specific charge cathode	$155\, Ah kg^{-1}$	$119\, Ah kg^{-1}$	$119\, Ah kg^{-1}$	$119\, Ah kg^{-1}$	$155\, Ah kg^{-1}$	$155\, Ah kg^{-1}$	$155\, Ah kg^{-1}$
Open circuit voltage	See A.1	See A.1	See A.1	See A.1	$LIB - 0.33\, V$	$LIB - 0.33\, V$	$LIB - 0.33\, V$
Gravimetric density anode active material	$2{,}200\, kg\, m^{-3}$	$1{,}700\, kg\, m^{-3}$	$1{,}700\, kg\, m^{-3}$	$1{,}700\, kg\, m^{-3}$	$2{,}200\, kg\, m^{-3}$	$2{,}200\, kg\, m^{-3}$	$2{,}200\, kg\, m^{-3}$
Gravimetric density cathode active material	$4{,}750\, kg\, m^{-3}$	$4{,}750\, kg\, m^{-3}$	$4{,}750\, kg\, m^{-3}$	$4{,}750\, kg\, m^{-3}$	$4{,}750\, kg\, m^{-3}$	$4{,}750\, kg\, m^{-3}$	$4{,}750\, kg\, m^{-3}$

3.2.3 *Manufacturing costs and life cycle assessment*

Practical specific energies and optimized LIB and NIB cell designs constitute the basis for the computation of material requirements used to assess costs and manufacturing-related life cycle GHG emissions. Table 3.3 lists the different battery cell components, material purchase costs, and the collected data sets for LCA. The functional unit for both the cost assessment and LCA is defined as the manufacturing of $1\,kWh$ of battery cell capacity without consideration of the battery use phase and end of lifetime aspects. GHG emissions were computed according to IPCC 2013 (100 year time frame) using the Python-based Brightway LCA framework [114]. Ecoinvent version 3.3 (system model *Allocation, cut-off by classification*) [115] served as the background database providing GHG emissions of all modeled battery materials and energy carriers with the associated supply chains. The calculations were performed for battery cells in standard industrial pouch format, where multiple electrode *sandwiches* consisting of anode current collector, anode, separator, cathode, and cathode current collector are stacked on top of each other. Because of the stacked arrangement of electrode sandwiches, the current collector thickness specified in table 3.3 corresponds to half of the actual thickness of the copper and aluminum sheets. Due to the unavailability of industrial data, it is assumed that the thickness of the NIB anode aluminum current collector is equal to the thickness of the LIB anode copper one. It should be noted, however, that this assumption is possibly favoring NIBs, as it is currently not clear whether the mechanical stability of aluminum allows for the processing of aluminum sheets with a thickness of only $8\,\mu m$. Following Patry et al. [19], a scrap rate of 9% is assumed for all components of the battery cell *sandwich*.

For the assessment of battery cell costs, the empirical bottom-up cost model developed by Patry et al. [19] is adapted. The total manufacturing costs are modeled as the sum of material purchase costs, process costs, and overhead costs. To account for the increasing worldwide manufacturing capacities since the publication of their study, learning curves are applied to compute battery process and overhead costs. Assuming an average annual growth of the LIB manufacturing capacity of 26% [14] between 2014 and 2019, process costs are discounted using a factor $D_{process} = 0.396$, and overhead costs are discounted using a factor $D_{overhead} = 0.629$ (see Ref. [105] for the details). Whereas the material purchase costs can be computed directly from the P2D model output, the process costs are estimated based on the underlying idea that they are dependent on the occupation time of production lines per kWh of battery cell capacity manufactured. [19] In this thesis work, it is assumed that the production line occupation times are inversely proportional to the areal specific energy of the electrode sandwiches the battery cells are composed of. More precisely, process costs (\$ per kWh) are modeled as the sum of a constant cost term (c_{const}) and a term that scales inversely with the areal

specific energy of the electrode sandwich ($A_{sandwich}$). $A_{sandwich,ref}$ is used to denote the areal specific energy of a reference sandwich, and c_{var} is a proportionality factor:

$$Process_{2014} = c_{const} + c_{var} \cdot \frac{A_{sandwich,ref}}{A_{sandwich}}, \tag{3.3a}$$

$$Process_{2019} = D_{process} \cdot Process_{2014}. \tag{3.3b}$$

The process cost modeling approach employed in this thesis differs somewhat from the original one [19] mainly in that the process costs are modeled as a function of the areal specific energy instead of the electrode thickness. The generalized approach used in this thesis is considered suitable to model LIB and NIB cells with disparate electrode porosities (anode porosities 17% - 30% and cathode porosities 18 - 47%). $A_{sandwich,ref}$ is defined as the areal specific energy of LIB 4C sandwiches (i.e., $A_{sandwich,ref} = 83\,Wh\,m^{-2}$). The process costs of LIB 4C cells are assumed to be equal to the process costs specified by Patry et al. [19] for an automotive NMC battery cell with $50\,\mu m$ anode thickness (i.e., $Process_{2014} = 69\$$ per kWh). A comparison with the process costs of automotive NMC battery cells with $100\,\mu m$ anode thickness ($Process_{2014} = 44\$$ per kWh) [19] allows for a parameterization of eq. (3.3a) ($c_{const} = 20\$$ per kWh and $c_{var} = 49\$$ per kWh).

Energy requirements for LCA calculations are based on Ref. [116] (see table 3.3 for the details). Furthermore, it is assumed that the water and energy requirements for battery cell manufacturing are proportional to the process costs. This modeling approach is based on the rationale that the water and energy requirements are dependent on the occupation time of production lines in a similar functional manner as the process costs. It should be noted that this approach allows only for an approximate estimation of the actual water and energy requirements.

Overhead costs ($ per kWh) are computed from the material purchase and process costs using the following empirical equation:

$$Overhead_{2014} = 0.66 \cdot Process_{2014} + 0.056 \cdot \left(Purchase + 1.66 \cdot Process_{2014}\right), \tag{3.4a}$$

$$Overhead_{2019} = D_{overhead} \cdot Overhead_{2014}. \tag{3.4b}$$

TABLE 3.3: LIB and NIB materials and processing steps, material purchase costs, and data sets for LCA. Required quantities of each battery cell component were derived from the output of the P2D model. Purchase costs of $NaPF_6$ and $NaNi_{1/3}Co_{1/3}Mn_{1/3}O_2$ are estimated based on the purchase costs of their lithium analogues by conceptually replacing Li by Na. Li_2CO_3 and Na_2CO_3 raw material costs are 13.9$ per kg [117] and 0.5$ per kg [13], respectively. If not specified otherwise, LCA data sets were adapted from a general LIB inventory source [7] using ecoinvent version 3.3 [115] as a background database. Used acronyms: carboxymethyl cellulose (CMC), styrene butadiene rubber (SBR), polyvinylidene fluoride (PVDF), polyvinyl fluoride (PVF), N-methyl-2-pyrrolidione (NMP), ethylene carbonate (EC), dimethyl carbonate (DMC), polypropylene (PP), polyethylene (PE).

Component	Materials and processing steps	Material purchase costs	Data sets for LCA
Current collectors LIB	• Aluminum current collector, thickness 10 μm (cathode side) • Sheet rolling aluminum • Copper current collector, thickness 4 μm (anode side) • Sheet rolling copper	• Aluminum: 15$/$kg$ [118] • Copper: 25$/$kg$ [118]	• Market for aluminum scrap, new • Market for copper • Sheet rolling
Current collectors NIB	• Aluminum current collector, thickness 10 μm (cathode side) • Aluminum current collector, thickness 4 μm (anode side) • Sheet rolling aluminum	• Aluminum: 15$/$kg$ [118]	• Market for aluminum scrap, new • Sheet rolling
Anode paste LIB	• 93 wt.%: graphite (active material) • 3 wt.%: binder (70 wt.% CMC + 30 wt.% SBR) • 4 wt.%: carbon additive	• Graphite: 15$/$kg$ [13] • Binder: 10$/$kg$ [101] • Carbon additive: 20$/$kg$ [118]	• Market for anode, graphite, for Li-ion battery • Market for CMC, powder • Market for SBR • Market for carbon black
Anode paste NIB	• 93 wt.%: hard carbon (active material) • 3 wt.%: binder (70 wt.% CMC + 30 wt.% SBR) • 4 wt.%: carbon additive	• Hard carbon: 15$/$kg$ [13] • Binder: 10$/$kg$ [101] • Carbon additive: 20$/$kg$ [118]	• Hard carbon from sugar precursor, inventory from Peters et al. [91] • Market for CMC, powder • Market for SBR • Market for carbon black
Cathode paste LIB	• 93 wt.%: $LiNi_{1/3}Co_{1/3}Mn_{1/3}O_2$ (active material) • 3 wt.%: PVF (binder), proxy for PVDF [12, 20] • 4 wt.%: carbon additive • NMP solvent	• $LiNi_{1/3}Co_{1/3}Mn_{1/3}O_2$: 20$/kg [13] • Binder: 10$/$kg$ [101] • Carbon additive: 20$/$kg$ [118] • NMP solvent costs are included in the process costs	• $LiNi_{1/3}Co_{1/3}Mn_{1/3}O_2$ • Market for PVF, proxy for PVDF [12, 20] • Market for carbon black • Market for NMP

Cathode paste NIB	• 93 wt.%: $NaNi_{1/3}Co_{1/3}Mn_{1/3}O_2$ (active material) • 3 wt.%: PVF (binder), proxy for PVDF [12, 20] • 4 wt.%: carbon additive • NMP solvent	• $NaNi_{1/3}Co_{1/3}Mn_{1/3}O_2$: 12.8$\$/kg$ (computed) • Binder: 10$\$/kg$ [101] • Carbon additive: 20$\$/kg$ [118] • NMP solvent costs are included in the process costs	• $NaNi_{1/3}Co_{1/3}Mn_{1/3}O_2$ inventory adapted from Ref. [7] • Market for PVF, proxy for PVDF [12, 20] • Market for carbon black • Market for NMP
Electrolyte LIB	• 12.7 wt.%: $LiPF_6$ salt • 87.3 wt.%: electrolyte solvent (30 wt.% EC + 70 wt.% DMC)	• Electrolyte (salt+solvent) 18$\$/kg$ [118]	• Market for $LiPF_6$ • Market for ethylene carbonate (proxy for electrolyte solvent mixture)
Electrolyte NIB	• 14.0 wt.%: $NaPF_6$ salt • 86.0 wt.%: electrolyte solvent (30 wt.% EC + 70 wt.% DMC)	• Electrolyte (salt+solvent) 17.6$\$/kg$ (computed)	• $NaPF_6$ inventory from Peters et al. [91] • Market for ethylene carbonate (proxy for electrolyte solvent mixture)
Separator LIB/NIB	• Separator, thickness 25μm, porosity 39% (50 wt.% PP + 50 wt.% PE) • Extrusion, plastic film	• Separator: 120$\$/kg$ [118]	• Market for PP • Market for PE • Market for extrusion, plastic film
Cell container	• Mass breakdown LIB/NIB cell: 97 wt.% electrode *sandwich*, 3 wt.% cell container	• Cell container costs are included in process costs	• Tab aluminum • Tab copper • Multilayer pouch
Water for cell manufacturing	• LIB 4C cell: 32.55kg per kWh of capacity • Other cells: proportional to process costs	• Included in process costs	• Market for water, decarbonized, at user
Energy for cell manufacturing	• LIB 4C cell: 40kWh per kWh of capacity (50% electricity, 50% heat) [116] • Other cells: proportional to process costs	• Included in process costs	• Market for electricity, medium voltage, country: South Korea [7] • Heat production, natural gas, furnace

3.3 MODEL RESULTS

3.3.1 *Present sodium-ion batteries*

Figure 3.2a compares practical specific energies projected for LIB ($LiNi_{1/3}Co_{1/3}Mn_{1/3}O_2$ vs. graphite) and NIB ($NaNi_{1/3}Co_{1/3}Mn_{1/3}O_2$ vs. hard carbon) cells exposed to discharge rates of $0.25\,C$, $4\,C$, and $10\,C$. Serving as a first validation of the developed modeling framework, a good agreement is observed between the practical specific energies projected for LIB 4C cells and NMC-based LIB cells currently used in electric vehicles (present work: $198.6\,Wh\,kg^{-1}$ (without cell packaging) and $192.6\,Wh\,kg^{-1}$ (including cell packaging); automotive cells: typically ca. $150\text{-}200\,Wh\,kg^{-1}$ [119]). Compared to their LIB counterparts, lower practical specific energies are projected for NIB cells at all discharge rates. However, a closer look at figure 3.2a reveals that the gap in practical specific energy between NIB and LIB cells is dependent on the discharge rate. For the *base* scenario, the gap in specific energy decreases from 45% ($0.25\,C$) to 41% ($4\,C$) and 37% ($10\,C$). These findings confirm that the enhanced kinetic processes in NIB cells have a significant impact on the high-power performance. However, for the particular NIB considered, this effect is not sufficient to compensate for the lower specific charges and voltage of the active materials.

It should be noted that the specific energies computed for LIB and NIB cells are of course sensitive to the parameterization of the P2D model. [120] In order to account for this uncertainty, not only a *base* scenario but also a *pessimistic* and *optimistic* one is considered for NIB cells (see table 3.1). The goal of this sensitivity analysis is to account for the main sources of uncertainty present in the assessment and hence to establish reliable ranges for the practical specific energy of NIB cells. In addition to that, another battery performance assessment is performed, where the practical specific energies of current LIB cells are compared to theoretical specific energies of NIB cells. For fixed battery active materials and cell design, such an assessment provides a theoretical upper bound for the specific energy one may expect for NIB cells. Assuming the same cell designs as for the NIB-B cells shown in figure 3.2a, theoretical specific energies amount to $152\,Wh\,kg^{-1}$ ($0.25\,C$ cell design), $131\,Wh\,kg^{-1}$ ($4\,C$ cell design), and $120\,Wh\,kg^{-1}$ ($10\,C$ cell design). It is evident that the theoretical specific energies of NIB cells are significantly lower than the practical specific energies of their LIB counterparts ($262\,Wh\,kg^{-1}$, $199\,Wh\,kg^{-1}$, and $158\,Wh\,kg^{-1}$, respectively).

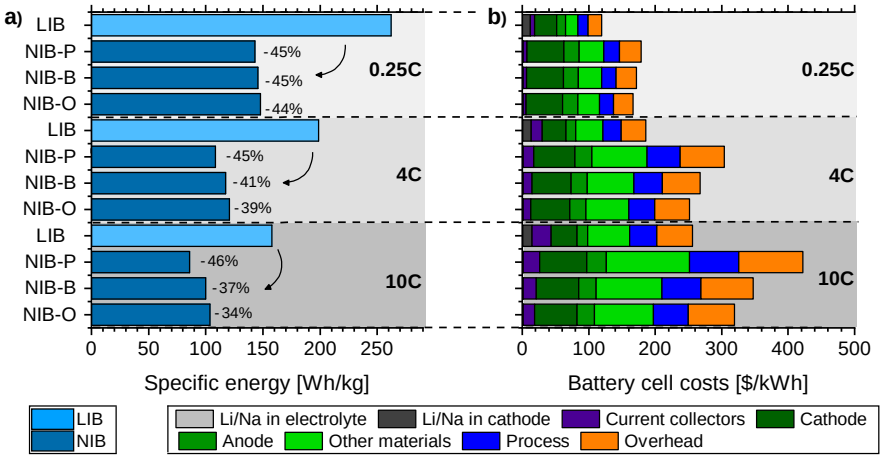

FIGURE 3.2: (a) Practical specific energies projected for LIB ($LiNi_{1/3}Co_{1/3}Mn_{1/3}O_2$ vs. graphite) and NIB ($NaNi_{1/3}Co_{1/3}Mn_{1/3}O_2$ vs. hard carbon) cells exposed to different discharge rates. The values are specified for the electrode *sandwich*, i.e., cell packaging is not included. (b) Manufacturing costs projected for LIB and NIB cells designed for varying discharge rates. The following contributions are shown: costs related to lithium and sodium raw materials for electrolyte (light grey) and cathode active material (dark grey) production, current collectors (violet), cathode active material costs without lithium and sodium raw materials (dark green), anode active material costs (medium green), other material purchase costs (light green), process costs (blue), and overhead costs (orange). Three scenarios are considered for NIB cells in (a) and (b): NIB present pessimistic (NIB-P), NIB present base (NIB-B), and NIB present optimistic (NIB-O).

Figure 3.2b shows LIB ($LiNi_{1/3}Co_{1/3}Mn_{1/3}O_2$ vs. graphite) and NIB ($NaNi_{1/3}Co_{1/3}Mn_{1/3}O_2$ vs. hard carbon) cell manufacturing costs computed as the sum of material purchase costs, process costs, and overhead costs. A comparison of both the cost structure and the total cell costs with industrial data shows that the developed modeling framework provides accurate cost estimates: while 186$ per *kWh* are projected for LIB 4C cells in this thesis work, Ref. [121] specifies 180$ per *kWh* for automotive LIB cells (NMC cathode). Material purchase costs account for 65% (this work) and 60%-70% [121] of total cell costs. For the material purchase costs, figure 3.2b further distinguishes between costs related to lithium (Li_2CO_3) and sodium (Na_2CO_3) raw materials, current collectors (i.e., aluminum and copper sheets), cathode active material costs (without Li/Na), anode active material costs, and contributions from other cell components. While sodium raw material costs are almost negligible (1.0-1.4$ per *kWh* of NIB cell capacity), lithium raw material costs are ca. 10 times higher (12-15$ per *kWh* of LIB cell capacity). However, despite ongoing discussions about rising lithium costs in the last years [13], lithium raw material costs amount to only 5.8-10.2% of the total LIB cell manufacturing costs. This calculation is based on the annual average price of battery-grade Li_2CO_3 in the year 2017, which was 13.9$ per *kg* [117]. Even in the case of an increase of the Li_2CO_3 price to 25$ per

kg, which may be considered the *worst-case* scenario [122], lithium raw material costs would only amount to 22 - 27 $ per *kWh* of LIB cell capacity. Apart from replacing lithium by sodium-based materials, additional cost savings can be achieved in NIBs by using aluminum instead of copper as the anode current collector. These cost savings are most pronounced for high power cells (LIB 10C vs. NIB 10C), where the combined expenditures for aluminum and copper can be reduced by 8.9 $ per *kWh*. Total material purchase costs are consistently higher for NIB than LIB cells, which can be attributed to lower practical specific energies of NIB cells and thus higher material requirements per *kWh* of capacity. Similarly, higher process costs are projected for NIB cells due to longer production line occupation times as a result of larger electrode areas per *kWh* of capacity.

In line with the above discussion of battery cell manufacturing costs, higher GHG emissions are projected for NIB cells (see figure 3.3), which can again be attributed to lower practical specific energies and thus higher material and material processing requirements. Due to comparatively high GHG emissions associated with cathode active materials ($LiNi_{1/3}Co_{1/3}Mn_{1/3}O_2$ and $NaNi_{1/3}Co_{1/3}Mn_{1/3}O_2$) and large quantities required, the cathode paste accounts for 41 - 60% of the total GHG emissions. Energy requirements for battery cell manufacturing contribute 20 - 37% to the total GHG emissions, while the sum of all other contributions is, on average, only 21%.

A comparison of the above findings with the results of an existing study evaluating NIBs from a life cycle perspective [91] reveals that the present work arrives at somewhat different conclusions. While Peters et al. [91] found GHG emissions of NIBs to be in the same range or even slightly lower compared to LIBs, the present work projects GHG emissions that are 45 - 78% higher for NIBs. Although the authors in Ref. [91] homogenized battery cell manufacturing energy requirements and electricity mixes to improve the comparability of the results with existing LCA studies on LIBs, they state that the comparability is still limited. The limited comparability may in part be due to the lack of consistency in the battery performance assumptions, as the specific energies of LIBs and NIBs were collected from different literature sources. The present analysis relies on more consistent performance data due to the use of a physics-based battery cell model for the parameterization of life cycle inventories, hence the results presented herein should be more reliable.

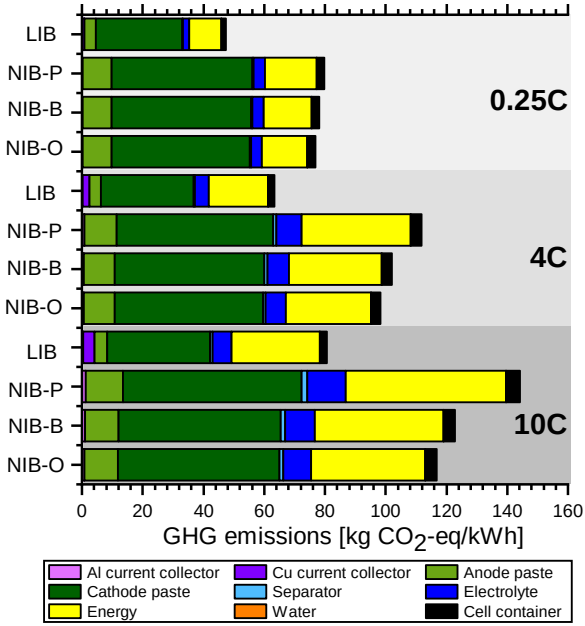

FIGURE 3.3: Manufacturing-related GHG emissions of LIB and NIB cells considering raw materials, energy carriers, manufacturing facilities, and their supply chains. Three scenarios are considered for NIB cells: NIB present pessimistic (NIB-P), NIB present base (NIB-B), and NIB present optimistic (NIB-O).

3.3.2 *Hypothetical sodium-ion batteries*

Figure 3.4 compares projected practical specific energies of LIB cells ($LiNi_{1/3}Co_{1/3}Mn_{1/3}O_2$ vs. graphite) and hypothetical NIB cells. Whereas the same specific charges and gravimetric densities are assumed for LIB and NIB active materials, NIB cells are expected to display an open circuit voltage that is $0.33\,V$ lower than for LIB cells, corresponding to the difference in the standard electrochemical potentials of Li^+/Li and Na^+/Na. At low discharge rates of $0.25\,C$, lower practical specific energies are projected for NIB cells, which can be attributed to their lower voltage. At high discharge rates, NIB cells are projected to be at least on par with their LIB counterparts. For the *base* scenario, the practical specific energy of NIB cells is 4% higher at $4\,C$ discharge and 12% higher at $10\,C$ discharge. At fast discharge rates, even in the absence of faster kinetic processes (*pessimistic* scenario), almost the same practical specific energy is projected for NIB cells. This is because of the increasing impact of the low-mass aluminum anode collector in NIB cells with decreasing electrode thickness, i.e., the lower mass of the aluminum current collector compared

to the copper one can compensate for the lower NIB cell voltage.

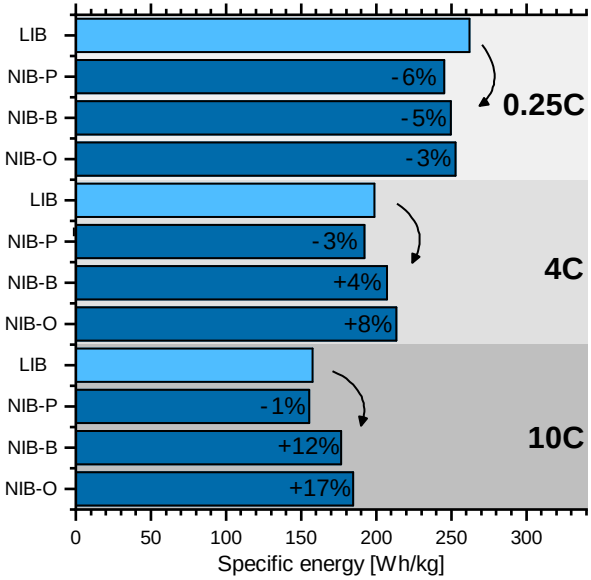

FIGURE 3.4: Practical specific energies projected for LIB ($LiNi_{1/3}Co_{1/3}Mn_{1/3}O_2$ vs. graphite) and hypothetical NIB cells exposed to varying discharge rates. Three scenarios are considered for NIB cells: NIB hypothetical pessimistic (NIB-P), NIB hypothetical base (NIB-B), and NIB hypothetical optimistic (NIB-O). The values are specified for the electrode *sandwich*, i.e., cell packaging is not included.

The strong inverse correlation found between the practical specific energy and both the costs and the GHG emissions implies that NIBs can only reasonably compete with LIBs if similar specific energies can be achieved for NIB cells. In comparison, other drivers, such as the choice of Li-ion and Na-ion based materials and anode current collector (copper vs. aluminum) will only play a secondary role as long as the supply chains of lithium raw materials and copper are not endangered. As NIBs may potentially reach similar or even slightly higher specific energies than LIBs in high-power applications, NIBs could become a viable alternative to LIBs even in the absence of interrupted lithium supply. However, a meaningful quantitative assessment of costs and GHG emissions is difficult to perform, as the chemical composition of active materials for prospective (hypothetical) NIBs, future material supply chains, location of production, and commodity prices are hard to predict.

3.4 SUMMARY

Intrigued by the promises of the NIB research community, the goal of this chapter was to perform a realistic assessment of current and prospective (hypothetical) NIB cells. The following three key metrics indispensable for the successful market implementation of NIBs were considered: (1) battery performance, i.e., practical specific energies at different discharge rates, (2) costs, and (3) environmental impacts evaluated based on manufacturing-related GHG emissions from a life cycle perspective. To ensure consistency in the assessment of the different metrics, a physics-based electrochemical battery cell model was employed to parameterize a bottom-up cost model and life cycle inventories. A comparison of the model results obtained for active material configurations considered representative of LIBs and NIBs (i.e., $LiNi_{1/3}Co_{1/3}Mn_{1/3}O_2$ vs. graphite and $NaNi_{1/3}Co_{1/3}Mn_{1/3}O_2$ vs. hard carbon, respectively) suggests that NIBs need further improvement in order to become competitive with LIBs. A strong inverse correlation was found between the practical specific energy of battery cells and both their manufacturing costs and environmental impacts. By contrast, other drivers, such as cost savings due to the replacement of lithium-based raw materials by sodium-based ones, were found to play only a minor role.

Overall, the comparative assessment of different cell chemistries performed in this chapter identified two targets that are of utmost importance for battery research: (i) increasing the specific charges and gravimetric densities[1] of the active materials and (ii) increasing the operating voltage of the battery cell. The impact of other key parameters, including the lifetime, on the viability of stationary energy storage in rechargeable batteries will be discussed in the following chapters.

[1] For a given number of stored charge carriers, higher gravimetric densities reduce the thickness of the electrodes. This does not only increase the (theoretical) volumetric energy density of battery cells but also reduces the transport distances of charge carriers inside the porous electrodes, which allows for faster charge and discharge rates.

4

BATTERIES IN STATIONARY APPLICATIONS

This chapter presents a modeling framework for the technical and economic assessment of stationary battery systems providing different services, including demand peak shaving (PS), price arbitrage (PA), and frequency regulation (FR). The chapter starts by reviewing approaches to integrate battery degradation models (see chapter 2.3) into energy economic models for battery dispatch optimization, thereby allowing battery operators to take into account the costs of battery usage in battery charge/discharge scheduling. Drawing from the ideas discussed in this brief literature review, an optimization model is developed, which maximizes the lifetime revenues of stationary battery systems providing (combined) PS and PA services. The chapter concludes by presenting a simulation model to analyze the provision of FR, such as primary control reserves (PCR). A number of case studies that cover a wide range of electricity market conditions, along with a numerical validation of the developed modeling framework, will be provided in chapter 5.

Parts of this chapter have been published by **S. F. Schneider**, P. Novák, and T. Kober, *IEEE Transactions on Sustainable Energy*, January 2021, 12, 1, 148-157, DOI: 10.1109/TSTE.2020.2988205 [123]

4.1 BATTERY DEGRADATION IN DISPATCH MODELS

As batteries degrade with time and use, their energy storage capabilities decrease until they are no longer suitable for the designated application. The rate of degradation is heavily dependent on the application case and operation pattern. It has therefore been recognized that battery degradation should be considered as an operational cost factor in dispatch scheduling, as the battery system may otherwise experience premature failure due to excessive usage. Eventually, neglecting the degradation of battery system components, mainly the battery cells, could result in suboptimal dispatch schedules and an incorrect assessment of the economic revenues of stationary battery systems. [10, 16, 58, 62, 77, 124, 125]

The challenges that arise when battery degradation models are integrated into an optimization framework for dispatch scheduling are two-fold: First, accurate degradation models, such as physics-based electrochemical ones [16], make the dispatch problem[1] more complex, thus relatively simple degradation models are generally employed to

[1] In operational decision-making, the term *dispatch problem* refers to an optimization model that determines the optimal charge and discharge power of battery systems.

preserve the tractability of the optimization model. For instance, battery degradation is often modeled as a linear function of the optimization variables (i.e., charge and discharge power during each discrete time period), giving rise to linear dispatch problems. Second, it is not *a priori* evident how exactly battery degradation should be converted to an economic cost [72]. In the below section, the focus is on the latter of these two challenges. An in-depth discussion of battery degradation models with varying degrees of accuracy and computational complexity is provided in chapter 2.3.

Assigning a cost to battery degradation is often performed based on battery system investment (or battery cell replacement) costs[2] and battery lifetime metrics [58]. The costs of battery degradation (γ) can be expressed as the product of the incurred degradation $\left(L_{tot}^{N}\right)$ and the battery costs (c_{bat}):

$$\gamma(\mathbf{P}^{ch}, \mathbf{P}^{dis}) = L_{tot}^{N}(\mathbf{P}^{ch}, \mathbf{P}^{dis}) \cdot c_{bat}. \tag{4.1}$$

In eq. (4.1), the degradation (L_{tot}^{N}) is normalized to the unit interval, that is, $L_{tot}^{N} \in [0,1]$, so that $L_{tot}^{N} = 0$ for a new battery and $L_{tot}^{N} = 1$ for a battery at the end of its lifetime (see chapter 5.2 for a discussion of different battery end of life criteria). The degradation is dependent on battery charge and discharge, denoted by the vectors $\mathbf{P}^{ch}$ and $\mathbf{P}^{dis}$, respectively.[3]

A common approach to account for battery degradation in dispatch scheduling is to introduce a penalty term in the objective function that subtracts from the revenues the costs related to battery degradation. Optimization problem (4.2a) - (4.2b) provides a generic framework for dispatch scheduling, where the objective function (4.2a) is maximized by finding optimal dispatch actions ($\mathbf{P}^{ch}, \mathbf{P}^{dis}$).

$$\underset{\mathbf{P}^{ch}, \mathbf{P}^{dis}}{\text{maximize}} \quad R(\mathbf{P}^{ch}, \mathbf{P}^{dis}) - \gamma(\mathbf{P}^{ch}, \mathbf{P}^{dis}), \tag{4.2a}$$

$$\text{s.t.} \quad \left(\mathbf{P}^{ch}, \mathbf{P}^{dis}\right) \in \mathcal{F}. \tag{4.2b}$$

In the objective function (4.2a), $R(\mathbf{P}^{ch}, \mathbf{P}^{dis})$ denotes the revenues of the battery, which are, like the costs of battery degradation, dependent on the charge and discharge power. Eq. (4.2b) denotes the set of all constraints. [58, 72, 126–128]

[2] The existing literature does not always distinguish between costs of battery cells and battery systems. In the following, the generic term *battery costs* is used to refer to either the cell or system costs.

[3] Semi-empirical approaches to model battery degradation are discussed in chapter 2.3.3, where parametric stress models are used to assess the degradation from the battery operation profile. As the operation profile is defined in terms of the charge and discharge power, the incurred degradation (L_{tot}^{N}) is expressed as a function of the charge power ($\mathbf{P}^{ch}$) and discharge power ($\mathbf{P}^{dis}$) in eq. (4.1). $\mathbf{P}^{ch}$ and $\mathbf{P}^{dis}$ are vectors of length T, with (P_t^{ch}, P_t^{dis}), $t = 1, 2, \ldots, T$, denoting the power charged to/discharged from the battery during each time step t.

From eq. (4.2a) - (4.2b) follows a simple criterion for dispatch scheduling (eq. 4.3), which states that additional revenue opportunities should be exploited as long as the marginal revenues ($\partial R / \partial L_{tot}^{N}$) exceed the marginal costs of battery degradation ($\partial \gamma / \partial L_{tot}^{N}$) [58, 72]:

$$\frac{\partial R}{\partial L_{tot}^{N}} > \frac{\partial \gamma}{\partial L_{tot}^{N}} = c_{bat}. \tag{4.3}$$

The criterion defined by eq. (4.3) provides a simple approach to account for battery degradation in dispatch scheduling. However, this modeling approach may lead to suboptimal long-term dispatch schedules, as batteries degrade not only when in use (cycle degradation) but also with time (calendar degradation). Therefore, the battery may be underutilized if operated only when the marginal revenues exceed the marginal degradation costs, hence the achievable lifetime revenues may be underestimated [72]. In order to overcome these issues, alternative modeling approaches have been proposed for the long-term dispatch scheduling of batteries. [72, 76, 128] Albeit different in terms of scope, application case, and degradation model employed, these approaches have in common that they aim to maximize the lifetime revenues of battery systems by bridging dispatch actions planned across different short to long-term time scales.

The remainder of this chapter is organized as follows: Chapter 4.2 presents an optimization model for the long-term dispatch scheduling of stationary battery systems providing (combined) PS and PA services, referred to as *PSPA model*. Chapter 4.3 presents a methodology for time series clustering that aims to reduce the run time of the PSPA model by selecting from a large data set a small number of representative load profiles and electricity price curves. Chapter 4.4 presents a simulation model to analyze the provision of PCR, referred to as *PCR model*. Chapter 4.5 discusses the key assumptions made in the PSPA and PCR models for battery degradation assessment. Chapter 4.6 summarizes the work presented in this chapter.

4.2 MODEL FOR PEAK SHAVING AND PRICE ARBITRAGE

4.2.1 *General set-up*

This chapter presents the *PSPA model* for the dispatch scheduling of stationary battery systems providing (combined) PS and PA services. The objective is to optimize battery dispatch so as to maximize the combined revenues from PS and PA over the lifetime of a battery. Battery dispatch is formulated as a tri-objective stepwise optimization problem: (1) maximizing PA revenues, (2) minimizing peak load expenditures (which is equivalent to maximizing PS revenues), (3) minimizing battery degradation. In case only one service is provided (i.e., PS or PA alone), battery dispatch simplifies to a bi-objective optimization problem. In the following, the more general case of three objectives is discussed, while model adaptations for the bi-objective setting are indicated where appropriate.
For operational decision-making, the PSPA model first solves a number of short-term dispatch problems multiple times to generate a set of Pareto optimal trade-off solutions[4] between the three objectives. As peak load expenditures usually occur on a monthly basis, these calculations are repeated for each month so that one Pareto set is computed for each month of battery operation. In the following, the term *PSPA project* is used to refer to all months of battery operation, with the duration of the PSPA project typically being 15 years. Subsequently, the model solves a second optimization problem to select Pareto optimal solutions for each month so as to maximize the combined revenues from PS and PA over the entire PSPA project duration. When providing the configuration of the battery system (i.e., size of energy and power units) as input, the PSPA model optimizes battery dispatch as described above and outputs the achievable lifetime revenues. As the optimal configuration is not *ex ante* known, these calculations are performed for multiple possible configurations from which the PSPA model identifies the most suitable one based on battery profitability. Figure 4.1 summarizes the conceptual building blocks of the PSPA model. A list of input parameters and variables used in the PSPA model is provided in table A2 and A3 in the appendix.

Input data: To reduce the run time of the PSPA model, a set of typical dispatch periods is considered. To this end, agglomerative hierarchical clustering [130] is performed on load and electricity price profiles of the entire year. The goal is to obtain a set of n *typical* dispatch periods, $i = 1,2,\ldots,n$, with vectors of loads $\mathbf{L}_i$ [MW] and prices $\mathbf{p}_i$ [EUR/MWh] of length T. In this thesis, dispatch periods of 24 - 72 hours with a time step length of 15 - 60 minutes will be considered, hence $T \in [24,288]$. $N_{m,i}$ is used to

[4] In multi-objective optimization, a solution is referred to as *Pareto optimal* if no objective can be further improved without compromising at least one of the other objectives [129].

denote the number of dispatch periods of type i in each month $m = 1,2,\ldots,12$ of a year. A discussion of the clustering algorithm is provided in chapter 4.3.

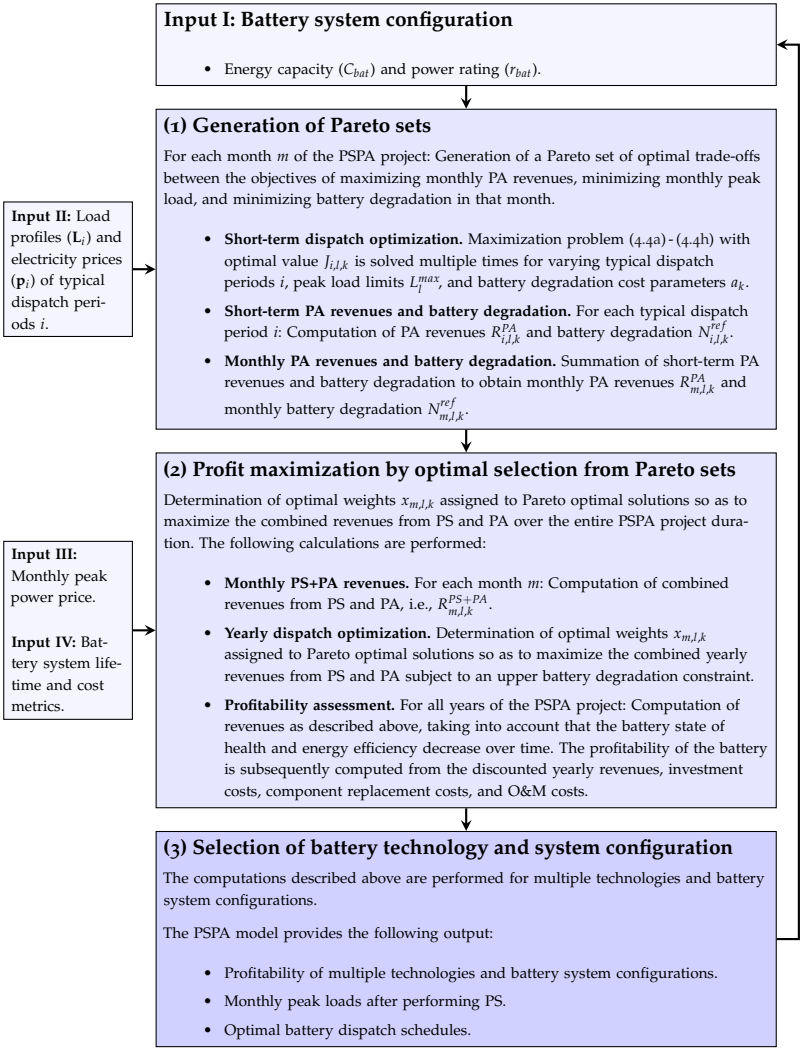

FIGURE 4.1: Flowchart showing the conceptual building blocks of the PSPA model.

4.2.2 *Generation of Pareto sets*

(See building block (1) in figure 4.1 for an overview of the calculation steps discussed below.)

Short-term dispatch optimization (4.4a) - (4.4h): The goal is to optimize battery charge and discharge in each discrete time period $t \in \mathcal{T} = \{1,2,\dots,T\}$ for maximum net revenues. For each dispatch period of type i and parameter values L_l^{max} and a_k, $l \in \mathcal{L} = \{1,2,\dots,L\}$, $k \in \mathcal{K} = \{1,2,\dots,K\}$, maximum net revenues $J_{i,l,k}$ are defined as the PA revenues minus the costs of battery degradation (eq. 4.4a). The costs of battery degradation are proportional to the number of equivalent cycles (N^{ref}) computed using the Rainflow algorithm: $N^{ref} = Rainflow(\mathbf{P}^{ch}, \mathbf{P}^{dis}, W) = \sum_c n_c (\delta_c / \delta_{ref})^W$, where n_c and δ_c are the cycle count ($n_c = 0.5$ for half cycles and $n_c = 1$ for full cycles) and depth of discharge, respectively, of each cycle c identified by the Rainflow algorithm, δ_{ref} denotes the depth of discharge of a reference cycle, and W is the technology-specific *Wöhler* coefficient.[5] The parameter a_k [EUR/cycle] converts the number of cycles to the costs of battery degradation.
Constraint (4.4b) ensures that the load does not exceed the anticipated monthly peak load L_l^{max}. Note that this constraint is not implemented if the battery is used only for PA. Constraint (4.4c) describes the evolution of the battery state of charge (SoC) level as determined by the vectors of the charge ($\mathbf{P}^{ch}$) and discharge ($\mathbf{P}^{dis}$) power $[MW]$. τ $[h]$, SoH_{bat} $[-]$, and η^{tot} $[-]$ denote the time step length, the current battery state of health (SoH), and the one-way energy efficiency of the battery system, respectively. Note that the battery state of health and energy efficiency decrease over time (see chapter 4.5). Constraint (4.4d) limits the battery SoC to the possible range. Constraint (4.4e) ensures that the SoC is equal to an anticipated value SoC^{end} at the end of the dispatch period. Constraints (4.4f) and (4.4g) ensure that the battery is operated within its charge and discharge power limit, respectively. An additional constraint (4.4h) is necessary to avoid simultaneous battery charging and discharging in the case of negative electricity prices. This constraint is needed for energy-economic models to ensure realistic charging and discharging of batteries. Without constraint (4.4h), mathematically optimal solutions could include simultaneous charging and discharging of batteries during time periods with negative electricity prices.

[5] In this thesis, a polynomial degradation *stress function* (see Ref. [81]) of the form $f_{cyc}(\delta) = \delta^W$ is used to model the degradation per cycle of depth δ. The degradation stress function $f_{cyc}(\delta)$ is parameterized by the *Wöhler* coefficient W. Typically, $W \in [1,2]$ for LIBs [53, 66].

$$J_{i,l,k} \quad =$$

$$\underset{\mathbf{P}^{ch},\mathbf{P}^{dis}}{\text{maximize}} \quad \sum_{t=1}^{T} \tau \left(P_t^{dis} - P_t^{ch} \right) p_{i,t} - \; a_k \cdot Rainflow\Big(\mathbf{P}^{ch},\mathbf{P}^{dis},W\Big) \tag{4.4a}$$

$$\text{s.t.} \quad P_t^{ch} - P_t^{dis} \leq L_l^{max} - L_{i,t}, \quad t \in \mathcal{T}, \tag{4.4b}$$

$$SoC_t = SoC^{init} + \frac{\tau}{C_{bat}\, SoH_{bat}} \sum_{t'=1}^{t} \left(\eta^{tot} P_{t'}^{ch} - \frac{1}{\eta^{tot}} P_{t'}^{dis} \right), \; t \in \mathcal{T}, \tag{4.4c}$$

$$0 \leq SoC_t \leq 1, \qquad t \in \mathcal{T}, \tag{4.4d}$$

$$SoC_{t=T} \; = \; SoC^{end}, \tag{4.4e}$$

$$0 \leq P_t^{ch} \leq r_{bat}\, C_{bat}\, SoH_{bat}, \qquad t \in \mathcal{T}, \tag{4.4f}$$

$$0 \leq P_t^{dis} \leq r_{bat}\, C_{bat}\, SoH_{bat}, \qquad t \in \mathcal{T}, \tag{4.4g}$$

$$P_t^{ch} \cdot P_t^{dis} = 0, \qquad t \in \mathcal{T}. \tag{4.4h}$$

In optimization problem (4.4a) - (4.4h), calendar ageing is not considered, as it is assumed that calendar ageing is not dependent on battery dispatch. For cycle ageing, stress factors other than the depth of discharge (δ), such as the SoC level (σ) and the current rate (r), are neglected. A discussion of these model assumptions is provided in chapter 4.5.

A common approach for selecting parameter values a_k in the objective function (4.4a) is based on the principle that the marginal revenues should at least compensate the marginal costs of battery degradation (see chapter 4.1). Hence, $a_k = c_{bat} / EoL_{cyc}$, where c_{bat} $[EUR]$ denotes the battery costs, and EoL_{cyc} is the cycle lifetime of the battery (number of equivalent cycles). In the PSPA model, a different approach is employed: instead of selecting values a_k as described above, *optimal* values a^* are determined endogenously. This ensures that the lifetime revenues of the battery are maximized. Note that under *non-optimal* values a_k, the battery would be underutilized (if the value a_k is too high) or overutilized (if the value a_k is too low). Both situations lead to suboptimal dispatch schedules, hence the lifetime revenues of the battery would be underestimated (see also Ref. [72]).

Shi et al. [81] proved that the number of equivalent cycles (N^{ref}) as computed using the Rainflow algorithm is convex in the dispatch actions ($\mathbf{P}^{ch}$,$\mathbf{P}^{dis}$) if the degradation stress function $f_{cyc}(\delta)$ is convex in the depth of discharge (δ) [81]. $f_{cyc}(\delta)$ expresses the degradation per cycle of depth δ. It is usually a convex function for LIBs [47, 53, 63, 66–68, 81]. Optimization problem (4.4a) - (4.4g) is therefore convex, and the globally optimal solution can be found using local optimization solvers. However, in the (typical)

case that the Wöhler coefficient $W \neq 1$, the objective function (4.4a) is not continuously differentiable, which the solver should be able to handle.[6] If $W = 1$, battery degradation depends linearly on the charge (P_t^{ch}) and discharge (P_t^{dis}) actions, $t = 1,2,\ldots,T$. In this case, the optimization problem (4.4a) - (4.4g) can be reformulated as a linear programming (LP) problem with the objective function (4.5):

$$\underset{\mathbf{P}^{ch},\mathbf{P}^{dis}}{\text{maximize}} \quad \sum_{t=1}^{T} \tau \left(P_t^{dis} - P_t^{ch} \right) p_{i,t} - \; a_k \cdot \sum_{t=1}^{T} \frac{\tau}{2\delta_{ref}} \left(\frac{\eta^{tot} P_t^{ch}}{C_{bat} SoH_{bat}} + \frac{P_t^{dis}}{C_{bat} SoH_{bat} \eta^{tot}} \right) \tag{4.5}$$

The LP problem with objective function (4.5) and constraints (4.4b) - (4.4g) can be solved using standard LP solvers. In order to implement the nonlinear constraint (4.4h), the problem can be reformulated as a mixed-integer linear programming (MILP) problem by defining additional binary variables that indicate whether the battery is charging or discharging [132]. The MILP problem can be solved using standard MILP solvers. The linear reformulation of constraint (4.4h) renders the feasible region of the optimization problem convex. If the objective function (4.4a) is nonlinear (i.e., $W \neq 1$), the nonlinear programming (NLP) problem (4.4a) - (4.4h), which is *nonconvex* because of the constraint (4.4h), can therefore be reformulated as a *convex* mixed-integer nonlinear programming (MINLP) problem. Despite its convexity, the MINLP problem is difficult to solve, as the optimization solver must be able to handle both the additional binary variables and the objective function (4.4a), which is not continuously differentiable in the nonlinear case. The NLP problem (4.4a) - (4.4h) was therefore *not* reformulated as a MINLP problem but solved directly using the SLSQP solver from the Python SciPy optimization library [131]. The solver was able to handle both the nonsmooth objective function (i.e., eq. (4.4a) with $W \neq 1$) and the nonlinear constraint (4.4h).[7]

Short-term PA revenues and battery degradation: Given optimal battery charge ($\mathbf{P}_*^{ch}$) and discharge ($\mathbf{P}_*^{dis}$) for a dispatch period of type i (obtained by computing maximum net revenues $J_{i,l,k}$), the PA revenues ($R_{i,l,k}^{PA}$) and the number of equivalent cycles ($N_{i,l,k}^{ref}$) are computed:

[6] The SLSQP solver provided in the Python SciPy optimization library [131] proved to be suitable to solve the optimization problem (4.4a) - (4.4h). By contrast, a number of other tested open-source and commercial nonlinear optimization solvers were not able to handle the discontinuous derivatives of the objective function (4.4a).

[7] In the majority of the case studies modeled in this thesis, implementation of the nonlinear constraint (4.4h) was not necessary, as the electricity price is usually non-negative. In order to solve optimization problems with both nonlinear objective function (i.e., eq. (4.4a) with $W \neq 1$) and nonlinear constraint (4.4h), the SLSQP solver was run from multiple randomly selected starting points. As the output of the solver was not sensitive to the starting point, it is assumed that the SLSQP solver is able to find the globally optimal solution of the optimization problem (4.4a) - (4.4h). A short overview of global optimization methods using multiple starting points is provided in Ref. [133].

$$R^{PA}_{i,l,k} = \sum_{t=1}^{T} \tau \left(P^{dis}_{*t} - P^{ch}_{*t} \right) p_{i,t}\,, \tag{4.6}$$

$$N^{ref}_{i,l,k} = Rainflow\left(\mathbf{P}^{ch}_{*}, \mathbf{P}^{dis}_{*}, W\right). \tag{4.7}$$

Monthly PA revenues and battery degradation: For each month m, the PA revenues ($R^{PA}_{m,l,k}$) and the number of equivalent cycles ($N^{ref}_{m,l,k}$) are the sum of the values over the typical dispatch periods:

$$R^{PA}_{m,l,k} = \sum_{i} N_{m,i} \cdot R^{PA}_{i,l,k}, \tag{4.8}$$

$$N^{ref}_{m,l,k} = \sum_{i} N_{m,i} \cdot N^{ref}_{i,l,k}, \tag{4.9}$$

where $N_{m,i}$ denotes the number of dispatch periods of type i in each month m.

4.2.3 *Profit maximization by optimal selection from Pareto sets*

(See building block (2) in figure 4.1 for an overview of the calculation steps discussed below.)

Monthly PS+PA revenues: Introducing a peak power price p^{month}_{peak} allows for the computation of combined monthly revenues from PS and PA:

$$R^{PS+PA}_{m,l,k} = R^{PA}_{m,l,k} + p^{month}_{peak} \left(\max \left\{ L_{i,t} : N_{m,i} \neq 0,\ t \in \mathcal{T} \right\} - L^{max}_{l} \right). \tag{4.10}$$

Yearly dispatch optimization (4.11a) - (4.11e): In the objective function (4.11a), yearly total revenues are maximized. The decision variables $x_{m,l,k} \in [0,1]$ assign weights to Pareto optimal solutions (between revenues $R^{PS+PA}_{m,l,k}$ (eq. 4.10) and degradation $N^{ref}_{m,l,k}$ (eq. 4.9) in month m). Constraint (4.11b) limits the number of cycles to EoL_{cyc}/EoL_{cal} (i.e., ratio of cycle and calendar lifetime) to ensure that the battery remains operational until the end of its calendar lifetime (see chapter 4.5 for a discussion of long-term dispatch optimization via constraint (4.11b)). Constraint (4.11c) ensures that the weights assigned in each month sum up to 1. Constraint (4.11d) ensures that in each month m the weight is assigned to one common peak capacity L^{max}_{l}, resulting in binary variables $\tilde{x}_{m,l} := \sum_{k \in \mathcal{K}} x_{m,l,k}$. The MILP problem (4.11a) - (4.11e) can be solved using standard MILP solvers, such as MATLAB intlincon.

$$R_{y*}^{PS+PA} =$$

$$\underset{x}{\text{maximize}} \quad \sum_{m\in\mathcal{M}}\sum_{l\in\mathcal{L}}\sum_{k\in\mathcal{K}} x_{m,l,k}\cdot R_{m,l,k}^{PS+PA} \tag{4.11a}$$

$$\text{s.t.} \quad \sum_{m\in\mathcal{M}}\sum_{l\in\mathcal{L}}\sum_{k\in\mathcal{K}} x_{m,l,k}\cdot N_{m,l,k}^{ref} \;\leq\; \frac{EoL_{cyc}}{EoL_{cal}}, \tag{4.11b}$$

$$\sum_{l\in\mathcal{L}}\sum_{k\in\mathcal{K}} x_{m,l,k} = 1, \qquad m\in\mathcal{M}, \tag{4.11c}$$

$$\sum_{k\in\mathcal{K}} x_{m,l,k} = \Big\{0,1\Big\}, \qquad m\in\mathcal{M},\; l\in\mathcal{L}, \tag{4.11d}$$

$$0\leq x_{m,l,k}\leq 1, \qquad m\in\mathcal{M},\; l\in\mathcal{L},\; k\in\mathcal{K}. \tag{4.11e}$$

Profitability assessment: Revenues R_{y*}^{PS+PA} for subsequent years of the PSPA project are computed as described above taking into account that the state of health and energy efficiency of the battery system deteriorate over time (see chapter 4.5). The economic assessment of different technologies and system configurations is performed based on battery *profitability*, which is computed from the total discounted revenues generated over the lifetime of the battery and the battery system investment, component replacement, and O&M costs (see chapter 5.1 for the details).

4.2.4 *Remark on alternative model formulations*

As an alternative to the modeling approach employed in the PSPA model, the long-term dispatch of battery systems could also be optimized using decomposition methods. Decomposition methods provide a powerful mathematical framework to solve a complex optimization problem by breaking it up into smaller sub-problems that are solved independently. The solution to the original problem is found in an iterative procedure that terminates as the variables shared between the sub-problems converge to their optimal value. For an overview of primal and dual decomposition methods, the interested reader is referred to Ref. [134] and references cited therein. Decomposition of an optimization model for battery dispatch scheduling is discussed in Ref. [76]. The new algorithmic approach implemented in the PSPA model shares some of the characteristics of decomposition methods in that the original problem (i.e., yearly dispatch optimization of battery systems) is solved by breaking it up into smaller sub-problems (i.e., short-term dispatch optimization) that are solved independently. [76, 134]

In the PSPA model, the short-term dispatch schedules are computed for a wide range of degradation cost parameters (a) and peak load limits (L^{max}). While the high number

of sub-problems increases the computational cost, the model implementation offers the advantage that the model results can be quickly recomputed for a wide range of battery cycle lifetimes (EoL_{cyc}), battery calendar lifetimes (EoL_{cal}), and peak load tariffs (p_{peak}^{month}) once the Pareto sets have been computed. For this reason, the first run of the PSPA model takes considerably longer than the subsequent model runs, which can be completed in a fraction of the time.[8] This is because the Pareto sets do not need to be recomputed if the other parameters of the battery system and the electricity market conditions do not change.[9] The user of the PSPA model can therefore quickly perform sensitivity analysis on the parameters EoL_{cyc}, EoL_{cal}, and p_{peak}^{month}. This is useful, for instance, to assess the impact of battery development targets, including the cycle (EoL_{cyc}) and calendar (EoL_{cal}) lifetime, on battery profitability.

[8] Once the Pareto sets have been computed, only the MILP problem (4.11a) - (4.11e) must be solved. Note that solving the MILP problem (4.11a) - (4.11e) is usually much faster than solving the (possibly nonlinear) short-term dispatch problem (4.4a) - (4.4g).

[9] If other parameters change, such as the energy capacity (C_{bat}), the power rating (r_{bat}), or the energy efficiency (η^{tot}) of the battery system, the Pareto sets must be recomputed.

4.3 TIME SERIES CLUSTERING

The goal of clustering is to group a large number of objects into a smaller number of mutually exclusive clusters such that the members in each cluster are similar to each other according to some suitable criterion [135]. Agglomerative hierarchical clustering algorithms start with single objects, i.e., clusters that contain only one member. Similar clusters are iteratively joined together until only one cluster remains that contains all objects. In each iteration the number of clusters is reduced by one. Compared to alternative clustering algorithms, such as k-means, hierarchical clustering offers the advantage of being completely reproducible: the algorithm always provides the same clustering output for the same input data set. [130, 136] In the PSPA model, agglomerative hierarchical clustering is employed to find a small number n of typical dispatch periods, $i = 1,2,\ldots,n$, with vectors of loads $\mathbf{L}_i$ and prices $\mathbf{p}_i$. The goal is to find dispatch periods that are representative of the load and price data of the entire year. This reduces the number of optimization problems that must be solved and thus the run time of the PSPA model. In the following, two procedures are presented for time series clustering: (i) clustering of price data (algorithm 2) and (ii) combined clustering of load and price data (algorithm 3). The two procedures are similar both conceptually and algorithmically. However, algorithm 2 is simpler in that the clustering is performed on a yearly basis without preserving monthly features in the input data set. N_i is used in algorithm 2 to denote the number of dispatch periods of type i. By contrast, algorithm 3 was developed specifically for the clustering of load and price time series used in the modeling of PS. As monthly features in the load data can have a big impact on PS revenues if peak load expenditures must be paid, algorithm 3 aims to preserve monthly features, such as the highest load in each month. $N_{m,i}$ is used in algorithm 3 to denote the number of dispatch periods of type i in each month m.

4.3.1 *Clustering of price data*

Algorithm 2 is used for the clustering of dispatch periods with vectors of prices $\mathbf{p}_d$, $d \in \mathcal{D} = \{1,2,\dots,D\}$, where D denotes the number of dispatch periods ($D = 365$ per year for 1-day dispatch periods and $D \approx 122$ per year for 3-day dispatch periods). $\mathbf{p}_d$ are vectors of length T, where T is the number of time steps in a dispatch period. Before clustering, step {2} of the algorithm reduces the dimensionality of the vectors from T to F by extracting a small number F of features that have a significant impact on PA revenues. Step {3} performs agglomerative hierarchical clustering on the feature vectors $\mathbf{x}_d \in \mathbb{R}^F$.

Algorithm 2: Clustering of price time series

Input: Price data for one year $p_{d,t}$, $d \in \mathcal{D} = \{1,2,\dots,D\}$, $t \in \mathcal{T} = \{1,2,\dots,T\}$.

Output: Set of n typical dispatch periods with price vectors $\mathbf{p}_i$, $i = 1,2,\dots,n$, of length T.

{1} *Normalize to unit interval.* Note that this step is shown for the sake of completeness only. It can be omitted, as the output of the clustering algorithm is not sensitive to input normalization if only time series data of one type is clustered (i.e., only price data).

$$p_{d,t}^{Norm} = \frac{p_{d,t} - min\left\{p_{d,t} : d \in \mathcal{D},\, t \in \mathcal{T}\right\}}{max\left\{p_{d,t} : d \in \mathcal{D},\, t \in \mathcal{T}\right\} - min\left\{p_{d,t} : d \in \mathcal{D},\, t \in \mathcal{T}\right\}}.$$

{2} *Feature extraction.* For each dispatch period d, time series features $x_{f,d}$, $f = 1,2,\dots,F$, are computed:

$$x_{1,d} = w_1 \left[\frac{1}{T} \sum\nolimits_{t \in \mathcal{T}} p_{d,t}^{Norm}\right],$$

$$x_{2,d} = w_2 \left[\sqrt{\frac{1}{T-1} \sum\nolimits_{t \in \mathcal{T}} \left(p_{d,t}^{Norm} - \frac{1}{T} \sum\nolimits_{t \in \mathcal{T}} p_{d,t}^{Norm}\right)^2}\right],$$

$$x_{3,d} = w_3 \left[\max\left\{p_{d,t}^{Norm} \,:\, t \in \mathcal{T}\right\} - \min\left\{p_{d,t}^{Norm} \,:\, t \in \mathcal{T}\right\}\right],$$

where $x_{1,d}$ denotes the mean of the (normalized) electricity price in dispatch period d, $x_{2,d}$ is the standard deviation, and $x_{3,d}$ is the price spread. The weights w_1, w_2, and w_3 are hyperparameters that determine the relative importance of the features during clustering.

The weights can be tuned to improve the performance of the clustering algorithm so as to minimize the deviation between the PSPA model results obtained with the clustered and unclustered data. For the price data sets considered in this thesis, the following weights proved to be suitable and hence were used for the clustering: $w_1 = 1$, $w_2 = 5$, $w_3 = 1$.

{3} *Agglomerative hierarchical clustering.* The MATLAB function *clusterdata* (Ward's minimum variance algorithm, see Ref. [137]) is used for agglomerative hierarchical clustering. The clustering is performed on the feature vectors $\mathbf{x}_d = [x_{1,d},\ x_{2,d},\ x_{3,d}]^T$, $d \in \mathcal{D}$.

{4} *Select representative days.* First, the centroid $\mathbf{p}_i^c$ (vector of length T) is computed for each typical dispatch period i:

$$\mathbf{p}_i^c = \tfrac{1}{N_i} \sum\nolimits_{d \in \mathcal{D}_i} \mathbf{p}_d,$$

where $\mathcal{D}_i$ denotes the set of dispatch periods assigned to cluster i, and N_i is the number of dispatch periods in $\mathcal{D}_i$.

For each dispatch period of type i, the representative price vector $\mathbf{p}_i$ is obtained by finding the vector $\mathbf{p}_{d^*}$ with the smallest Euclidian distance from the centroid vector $\mathbf{p}_i^c$:

$$\mathbf{p}_i = \mathbf{p}_{d^*},\ \ d^* = \arg\min\nolimits_{d \in \mathcal{D}_i} \left\| \mathbf{p}_d - \mathbf{p}_i^c \right\|_2.$$

4.3.2 *Combined clustering of price and load data*

Algorithm 3 is used for the clustering of dispatch periods with vectors of loads $\mathbf{L}_d$ and prices $\mathbf{p}_d$, $d \in \mathcal{D} = \{1,2,\ldots,D\}$, where D denotes the number of dispatch periods ($D = 365$ per year for 1-day dispatch periods and $D \approx 122$ per year for 3-day dispatch periods). $\mathbf{L}_d$ and $\mathbf{p}_d$ are vectors of length T, where T is the number of time steps in a dispatch period. Before clustering, step {2} of the algorithm reduces the dimensionality of the data set from $2T$ (the dimensionality of both the price vectors and the load vectors is T, hence the dimensionality of the data set is $2T$) to F by extracting a small number F of features that have a significant impact on PS and PA revenues. Step {3} performs agglomerative hierarchical clustering on the feature vectors $\mathbf{x}_d \in \mathbb{R}^F$. In step {4}, representative vectors of loads ($\mathbf{L}_i$) and prices ($\mathbf{p}_i$) are selected based on similarities with the centroid load vector ($\mathbf{L}_i^c$) in each dispatch period of type i. Note that this clustering approach gives higher priority to preserving similarities in load profiles than prices during clustering and is thus suitable if load-related features have a big impact on the achievable revenues.

Algorithm 3: Combined clustering of load and price time series

---

Input: Load $L_{d,t}$ and price $p_{d,t}$ data for one year, $d \in \mathcal{D} = \{1,2,\ldots,D\}$, $t \in \mathcal{T} = \{1,2,\ldots,T\}$.

Output: Set of n typical dispatch periods with vectors of loads $\mathbf{L}_i$ and prices $\mathbf{p}_i$, $i = 1,2,\ldots,n$, of length T.

{1} *Normalize to unit interval.*

$$p_{d,t}^{Norm} = \frac{p_{d,t} - min\left\{p_{d,t} : d\in\mathcal{D},\, t\in\mathcal{T}\right\}}{max\left\{p_{d,t} : d\in\mathcal{D},\, t\in\mathcal{T}\right\} - min\left\{p_{d,t} : d\in\mathcal{D},\, t\in\mathcal{T}\right\}},$$

$$L_{d,t}^{Norm} = \frac{L_{d,t} - min\left\{L_{d,t} : d\in\mathcal{D},\, t\in\mathcal{T}\right\}}{max\left\{L_{d,t} : d\in\mathcal{D},\, t\in\mathcal{T}\right\} - min\left\{L_{d,t} : d\in\mathcal{D},\, t\in\mathcal{T}\right\}}.$$

{2} *Feature extraction.* For each dispatch period d, time series features $x_{f,d}$, $f = 1,2,\ldots,F$, are computed:

$$x_{1,d} = w_1\left[\tfrac{1}{T}\sum\nolimits_{t\in\mathcal{T}} p_{d,t}^{Norm}\right],$$

$$x_{2,d} = w_2\left[\sqrt{\tfrac{1}{T-1}\sum\nolimits_{t\in\mathcal{T}}\left(p_{d,t}^{Norm} - \tfrac{1}{T}\sum\nolimits_{t\in\mathcal{T}} p_{d,t}^{Norm}\right)^2}\right],$$

$$x_{3,d} = w_3\left[\max\left\{p_{d,t}^{Norm} \;:\; t\in\mathcal{T}\right\} - \min\left\{p_{d,t}^{Norm} \;:\; t\in\mathcal{T}\right\}\right],$$

$$x_{4,d} = w_4\left[max\left\{L_{d,t}^{Norm} \;:\; t\in\mathcal{T}\right\}\right],$$

where $x_{1,d}$ denotes the mean of the (normalized) electricity price in dispatch period d, $x_{2,d}$ is the standard deviation, and $x_{3,d}$ is the price spread. $x_{4,d}$ denotes the (normalized) peak load in dispatch period d. The weights w_1, w_2, w_3, and w_4 are hyperparameters that determine the relative importance of the features during clustering. They can be tuned to improve the performance of the clustering algorithm so as to minimize the deviation between the PSPA model results obtained with the clustered and unclustered data. For the data sets considered in this thesis, the following weights proved to be suitable and hence were used for the clustering: $w_1 = 1$, $w_2 = 5$, $w_3 = 1$, $w_4 = 7$.

{3} *Agglomerative hierarchical clustering.* The MATLAB function *clusterdata* (Ward's minimum variance algorithm, see Ref. [137]) is used for agglomerative hierarchical clustering. The clustering is performed on the feature vectors $\mathbf{x}_d = [x_{1,d},\ x_{2,d},\ x_{3,d},\ x_{4,d}]^T$, $d \in \mathcal{D}$.

{4} *Select representative days.* First, the centroid load $\mathbf{L}_i^c$ (vector of length T) is computed for each typical dispatch period i:

$$\mathbf{L}_i^c = \tfrac{1}{N_i} \sum\nolimits_{d \in \mathcal{D}_i} \mathbf{L}_d,$$

where $\mathcal{D}_i$ denotes the set of dispatch periods assigned to cluster i, and N_i is the number of dispatch periods in $\mathcal{D}_i$.

The representative dispatch periods i (with load and price vectors $\mathbf{L'}_i$ and $\mathbf{p}_i$, respectively) are defined as those dispatch periods d^* in the input data set with load vectors $\mathbf{L}_{d^*}$ that have the smallest Euclidian distance from the centroid load vectors $\mathbf{L}_i^c$:

$$(\mathbf{L}_i^{'}, \mathbf{p}_i) = (\mathbf{L}_{d^*}, \mathbf{p}_{d^*}),\ \ d^* = \arg\min_{d \in \mathcal{D}_i} \left\| \mathbf{L}_d - \mathbf{L}_i^c \right\|_2.$$

To ensure that the monthly peak loads are, on average, identical before and after clustering, the representative load vectors $\mathbf{L'}_i$ are scaled by a factor $\frac{\overline{P_u}}{\overline{P_c}}$:

$$\mathbf{L}_i = \mathbf{L}_i^{'} \cdot \tfrac{\overline{P_u}}{\overline{P_c}},$$

where $\overline{P_u}$ and $\overline{P_c}$ are the average monthly peak loads in the unclustered and clustered data, respectively.

Instead of N_i, algorithm 3 outputs $N_{m,i}$, denoting the number of dispatch periods of type i in each month m. N_i is obtained from $N_{m,i}$ by counting the number of typical dispatch periods in all 12 months of the year, i.e., $N_i = \sum_{m=1}^{12} N_{m,i}$.

4.4 MODEL FOR PRIMARY CONTROL RESERVES

4.4.1 *Overview*

This chapter presents the *PCR model* for the techno-economic assessment of stationary battery systems providing frequency regulation (FR) services, including primary control reserves (PCR). The provision of other services such as PS and PA is not considered in the PCR model.

The goal of PCR is to reduce deviations from the default (i.e., nominal) grid frequency in the case that the supply and demand of electricity are not balanced. Energy storage units providing PCR are bound to the regulatory framework defined by the responsible transmission system operator (TSO). In the PCR model, the framework for Switzerland [138] is considered, which is largely identical to the regulatory conditions in other European countries. [7, 138–140]
In order to reduce deviations from the nominal grid frequency ($f^{nom} = 50\,Hz$), PCR units must follow a control signal proportional to the current frequency deviation so that power is withdrawn from the grid if $f > f^{nom}$, whereas power is provided to the grid if $f < f^{nom}$. As the control signal may not be zero-mean[10] and due to internal energy losses in the battery system, suitable strategies must be implemented to actively manage the battery SoC level to ensure that the battery system remains operational at (almost) all times. [138, 139] Two common strategies for SoC control rely on scheduled power exchanges in electricity markets that are triggered by threshold [141, 142] or moving average [139, 143, 144] based control schemes. In the threshold based control scheme, charge/discharge power is traded on the electricity market as soon as the SoC level exceeds an upper threshold value or falls below a lower threshold value. That is, triggered by deviations from a reference SoC level, the SoC controller of the battery system initiates mechanisms to restore the SoC level via charge/discharge power traded on electricity markets. In contrast to the threshold based control scheme, the moving average based control scheme controls the SoC by compensating for power losses and gains incurred during a certain time period in the past. Regardless of the SoC control scheme applied, the physical delivery of the charge/discharge power occurs in parallel with the provision of the PCR service (see figure 4.3 for an illustration of the different power flows between the battery system and the electricity grid). Notably, efficient SoC control requires that the battery system has access to electricity markets with short lead times and short contract durations, such as the intraday electricity market. This ensures that the SoC level can be restored quickly after following an unbalanced control signal, which guarantees the continuous

[10] The control signal is not zero-mean if the grid frequency is higher or lower than $50\,Hz$ for extended periods of time.

availability of the battery system for PCR provision.

Instead of relying on scheduled power exchanges in electricity markets, the battery SoC could also be restored through bilateral energy contracts (e.g., with a utility) or by pooling the battery system with a generating unit. [138, 143] In the PCR model, battery systems are assumed to be operated independently of any generating units. Therefore, SoC control must be achieved via contracts traded on electricity markets.

The PCR model adopts a moving average based SoC control scheme similar to the one proposed by Borsche et al. [143] and used in Ref. [139] to analyze the provision of PCR services under different regulatory conditions. Notably, moving average based strategies offer high control flexibility, as SoC restoration is initiated already in the presence of small deviations from the reference SoC level. By contrast, threshold based strategies trigger power exchanges less frequently, hence they may require more time for SoC restoration. In the PCR model, access to electricity markets with different lead times and contract durations is represented by different sets of SoC control scheme parameters. This allows for a technical and economic assessment of PCR provided under a wide range of electricity market conditions.

The conceptual building blocks of the PCR model are summarized in figure 4.2. In a first step (S1), the PCR model evaluates the *theoretical PCR capacity* that can be offered while respecting both the physical constraints of the battery system and the regulatory conditions. Operational limits on battery degradation are neglected in step (S1). In a second step (S2), a degradation model evaluates the expected number of cycles the battery system would incur when providing the theoretical PCR capacity. If the number of cycles complies with an operational limit on battery degradation, the *offered PCR capacity* corresponds to the theoretical one (S3a). Otherwise, the offered PCR capacity is determined in an incremental procedure (S3b). Calculation steps (S1) - (S3) are repeated for all years of battery operation (further referred to as *PCR project duration*, which is typically 15 years), taking into account that the battery state of health and energy efficiency decrease over time. When providing the configuration of the battery system (i.e., size of energy and power units) as input, the PCR model simulates battery operation, evaluates the amount of PCR capacity that can be offered in each year, and outputs the achievable lifetime revenues. As the optimal configuration is not *ex ante* known, these calculations are performed for multiple possible configurations from which the PCR model identifies the most suitable one based on battery profitability. A list of input parameters and variables used in the PCR model is provided in tables A2 and A4 in the appendix.

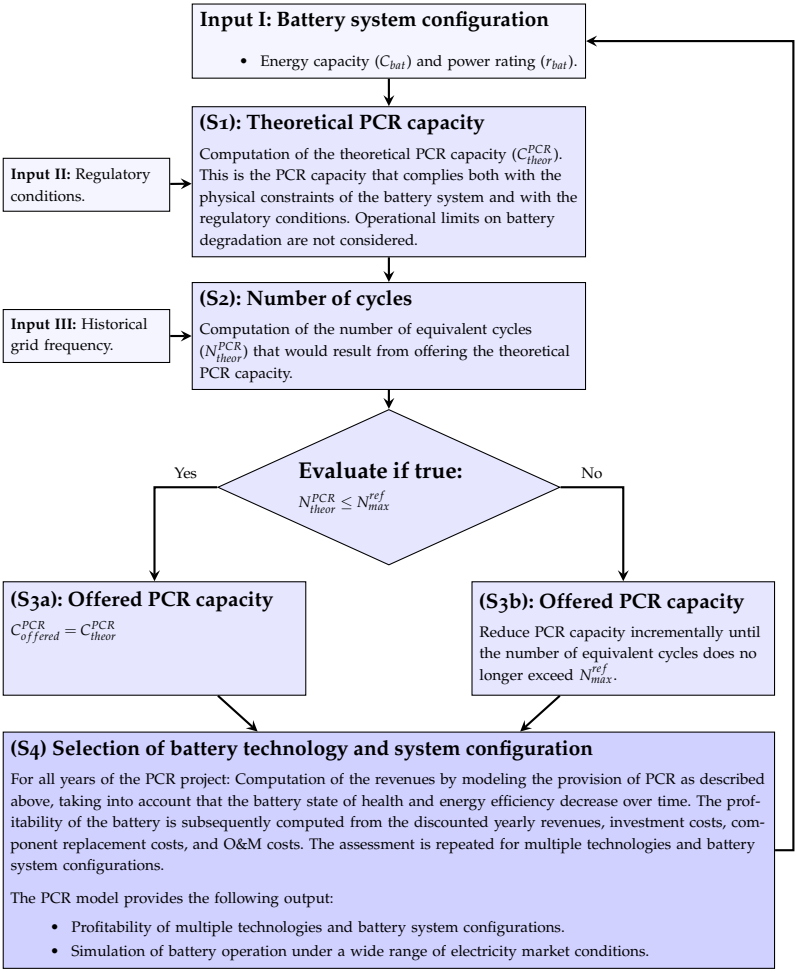

FIGURE 4.2: Flowchart showing the conceptual building blocks of the PCR model.

4.4.2 *Theoretical PCR capacity*

In the PCR model, the theoretical PCR capacity is defined as the maximum regulation capacity that can be provided while respecting both the physical battery system constraints (i.e., limits on the usable energy capacity and limits on the charge and discharge rate) and the regulatory conditions. In the following, the regulatory conditions defined by *Swissgrid* [138], the responsible TSO in Switzerland, are considered. For each year of battery operation, the theoretical PCR capacity is the highest capacity the battery system can provide under a *prequalification* time series of the grid frequency ($\mathbf{f}^p$) as defined by Swissgrid's prequalification criteria (see below). This is expressed by optimization problem (4.12a)-(4.12b), which defines the theoretical PCR capacity (C^{PCR}_{theor}) as the highest capacity $C^{PCR} \in \mathcal{C}^{\mathcal{PCR}}$ that is compatible with battery SoC constraints at all times, where $\mathcal{C}^{\mathcal{PCR}}$ denotes the set of tradable capacities.[11] Constraint (4.12b) ensures that the SoC profile that results from providing C^{PCR} is physically possible, that is, between 0% and 100% at all times. As discussed in the below sections, the SoC profile depends on C^{PCR}, the prequalification time series of the grid frequency ($\mathbf{f}^p$), and multiple parameters related to the battery system configuration and SoC control scheme.

$$C^{PCR}_{theor} = \underset{C^{PCR} \in \mathcal{C}^{\mathcal{PCR}}}{\text{maximize}} \quad C^{PCR}, \tag{4.12a}$$

$$\text{s.t.} \quad SoC_t\left(C^{PCR}, \mathbf{f}^p\right) \in [0,1], \quad t \in \{1,2,\ldots,T_p\}. \tag{4.12b}$$

In eq. (4.12b), SoC_t, $t = 1,2,\ldots,T_p$, denotes the battery state of charge level, and $\mathbf{f}^p$ is the prequalification time series of the grid frequency (vector of length T_p).

The prequalification time series of the grid frequency ($\mathbf{f}^p$) can be derived from the regulatory conditions defined by the TSO. The prequalification requirements of Swissgrid stipulate that battery systems and other storage units with limited energy capacity must be continuously available for PCR provision during *normal* evolution of the grid frequency. This is the case as long as none of the following three criteria is met: (i) $|f_t - f^{nom}| \geq 200\,mHz$, (ii) $|f_t - f^{nom}| \geq 100\,mHz$ for more than $5\,min$, (iii) $|f_t - f^{nom}| \geq 50\,mHz$ for more than $15\,min$. Hence, $\mathbf{f}^p$ is the following time series of the grid frequency: $49.80\,Hz$ for $5\,min$, $49.90\,Hz$ for $10\,min$, and $49.95\,Hz$ for an indefinite

[11] In Switzerland, market participants can provide PCR capacities between $1\,MW$ and $25\,MW$ [145]. In the PCR model, it is assumed that battery operators have the option to pool multiple independent battery systems into one bigger storage unit. Therefore, a smaller granularity of $0.01\,MW$ is assumed, hence the set of tradable capacities $\mathcal{C}^{\mathcal{PCR}} = \{0.01, 0.02, \ldots, 25.00\}$.

time duration.[12] In addition to continuous availability during *normal* evolution of the grid frequency, an energy reserve of $15\,min$ must be kept, also referred to as *15 min criterion*, which means that the battery system must be able to provide the full[13] PCR capacity for additional $15\,min$. [138, 139] Under the $15\,min$ criterion, the allowed SoC range is more narrow than in (4.12a) - (4.12b). In the general case of keeping an energy reserve τ^{Res} $[h]$, the theoretical PCR capacity is computed as follows:

$$C^{PCR}_{theor} = \underset{C^{PCR} \in \mathcal{C}^{PCR}}{\text{maximize}} \; C^{PCR}, \tag{4.13a}$$

$$\text{s.t. } SoC_t(C^{PCR}, \mathbf{f}^p) \in \left[\frac{C^{PCR}\tau^{Res}}{C_{bat}\, SoH_{bat}\, \eta^{tot}}, 1 - \frac{C^{PCR}\tau^{Res}\eta^{tot}}{C_{bat}\, SoH_{bat}} \right], \quad t \in \{1, 2, \ldots, T_p\}, \tag{4.13b}$$

where C_{bat} $[MWh]$, SoH_{bat} $[-]$ and η^{tot} $[-]$ denote the energy capacity, the state of health, and the one-way energy efficiency of the battery system, respectively. Note that the original optimization problem (4.12a) - (4.12b) is recovered if $\tau^{Res} = 0$.

The evolution of the battery SoC is modeled by eq. (4.14) [143]. The grid frequency is typically measured every second, hence the time step length $\tau := 1\,s$ in the PCR model.

$$SoC_{t+1} = SoC_t + \begin{cases} \frac{\tau \cdot C^{PCR}}{3{,}600\, C_{bat}\, SoH_{bat}}\, \eta^{tot}\, P^{Ext}_t & \text{if} \quad P^{Ext}_t \geq 0, \\ \frac{\tau \cdot C^{PCR}}{3{,}600\, C_{bat}\, SoH_{bat}}\, \frac{1}{\eta^{tot}}\, P^{Ext}_t & \text{if} \quad P^{Ext}_t < 0, \end{cases} \tag{4.14}$$

where P^{Ext}_t $[MW/MW]$ denotes the power exchanged between the electricity grid and the battery system. A positive sign indicates battery charging and a negative sign battery discharging. P^{Ext}_t is the sum of two power flows (eq. 4.15): (i) the power for PCR provision (P^{PCR}_t) $[MW/MW]$ and (ii) the power for SoC control (P^{WP}_t) $[MW/MW]$, referred to as the *working point* of the battery system. [143] All quantities in eq. (4.15) have units $[MW/MW]$, as they denote power flows per MW of offered PCR capacity.

$$P^{Ext}_t = P^{PCR}_t + P^{WP}_t. \tag{4.15}$$

Figure 4.3 shows a schematic of a battery system providing PCR.

[12] For *positive* deviations from the nominal frequency, $\mathbf{f}^p$ is the following time series: $50.20\,Hz$ for $5\,min$, $50.10\,Hz$ for $10\,min$, and $50.05\,Hz$ for an indefinite time duration. As the reference SoC value $SoC^{init} = 50\%$ in the PCR model, consideration of the prequalification time series for *negative* frequency deviations is sufficient.

[13] Providing the *full* PCR capacity corresponds to supplying either $-1\,MW$ or $+1\,MW$ of regulation power per MW of offered PCR capacity (see the below sections for more details).

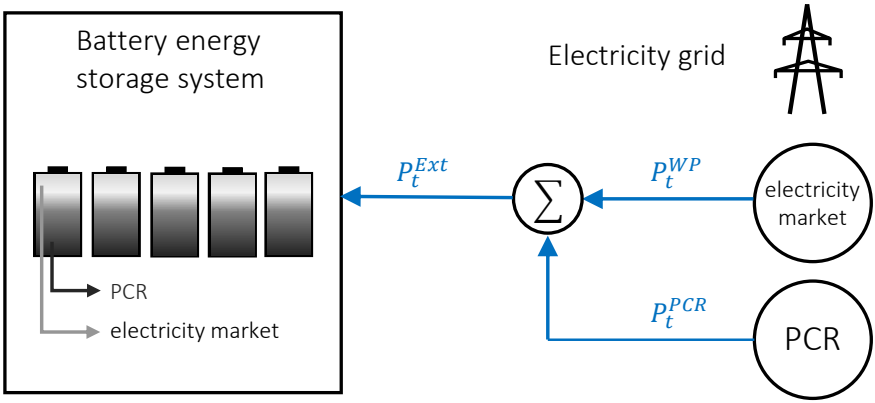

FIGURE 4.3: Illustration of a battery system providing PCR. The blue arrows denote varying power flows: (i) the power flow for providing the PCR service (P_t^{PCR}), (ii) the power flow for SoC control via the electricity market (P_t^{WP}), and (iii) the total power exchanged between the electricity grid and the battery system (P_t^{Ext}). The direction of the arrows indicates the direction of power flows. (For instance, if $P_t^{Ext} > 0$, power is supplied from the electricity grid to the battery energy storage system, and the battery system is charging. Conversely, if $P_t^{Ext} < 0$, power is supplied from the battery energy storage system to the electricity grid, and the battery system is discharging.) The figure illustrates that one part of the battery's charge/discharge power capacity is used for SoC control via the electricity market (light grey), while another part of the power capacity is reserved for the provision of the PCR service (dark grey).

Due to limits on the charge and discharge rate of the battery system, complete restoration of the SoC level may not always be possible. Therefore, the following distinction is made: The *anticipated* working point ($P_t^{WP_{ant}}$) $[MW/MW]$ denotes the working point as determined by the SoC control scheme, whereas the *actual* working point (P_t^{WP}) introduced above is the working point that complies with the battery system constraints. If the anticipated working point complies with the battery system constraints, $P_t^{WP} = P_t^{WP_{ant}}$. The *difference* between the *anticipated* and *actual* working point is denoted as $P_t^{WP_{diff}}$ $[MW/MW]$:

$$P_t^{WP_{diff}} = P_t^{WP_{ant}} - P_t^{WP}. \tag{4.16}$$

The working point is subject to the following conditions of the electricity market: (i) electricity contracts can be traded only for certain time periods[14], and (ii) electricity contracts are typically subject to a lead time (i.e., time lag) between power exchange scheduling and physical delivery. The SoC control scheme (eq. 4.17) is compatible with these conditions and hence is used to compute the anticipated working point ($P_t^{WP_{ant}}$). It should be noted that eq. (4.17) is used to compute the *anticipated* working point, whereas the *actual* working point is given by eq. (4.19). To illustrate the working prin-

[14] For instance, on the intraday electricity market, electricity contracts can be closed every 15 *min* with a contract duration of 15 *min*. [146]

ciple of SoC restoration via eq. (4.17), a numerical example for the computation of the anticipated working point is provided in *Numerical example I*.

$$P_k^{WP_{ant}} = \sum_{k'}^{k'+\tau_{MA}-1} \frac{(-P_{k'}^{PCR} + P_{k'}^{Loss})}{\tau_{MA}} + P_{k-\tau_{WP}}^{WP_{diff}}, \quad \text{with} \quad k' = \left\lfloor \frac{k-\tau_{LT}-1}{\tau_{WP}} \right\rfloor \cdot \tau_{WP} - \tau_{MA} + 1, \tag{4.17}$$

where $\lfloor \cdot \rfloor$ is the floor operator and P_t^{Loss} denotes energy losses in the battery system (eq. 4.20). τ_{LT}, τ_{WP}, and τ_{MA} are the parameters of the SoC control scheme:

- $\tau_{LT} \geq 0$ $[s]$ denotes the *lead time* (i.e., time lag) between power exchange scheduling and physical delivery.
- $\tau_{WP} \geq 1$ $[s]$ denotes the *contract duration* for scheduled power exchanges.
- $\tau_{MA} \geq 1$ $[s]$ denotes the duration of the *averaging period* considered for the computation of the working point.

Numerical example I: Working principle of the SoC control scheme (eq. 4.17), inspired by Ref. [143]

Parameters: Define the parameters of the SoC control scheme (example): $\tau_{LT} = 1800\,s$, $\tau_{WP} = 900\,s$, and $\tau_{MA} = 900\,s$. These parameter values are representative of an electricity market with $15\,min$ contracts with $30\,min$ lead time and for an averaging period of $15\,min$.

Example: Consider the period with time steps $k' \in [901, 1800]$ (shown in green in the below illustration). At time step 1800, eq. (4.17) is used to compute the working point that will be applied during later time steps $k \in [3601, 4500]$ (shown in blue). The goal of setting the working point is (i) to cancel out imbalances in the control signal [143] during time steps [901, 1800], (ii) to compensate for power losses (eq. 4.20) [143] incurred during time steps [901, 1800], and (iii) to compensate for possible imbalances incurred during the averaging period [1, 900] that cannot be compensated during the period [2701, 3600].

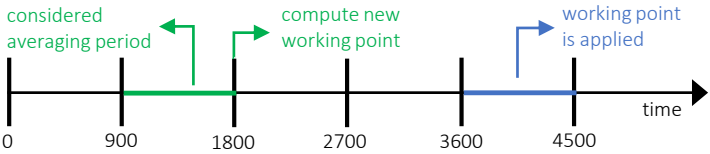

The parameters of the SoC control scheme have an important impact on how fast imbalances can be compensated and thus on the PCR capacity the battery system

is able to provide. In general, long lead times (τ_{LT}) and long contract durations (τ_{WP}) impede fast SoC restoration, whereas short lead times (τ_{LT}) and short contract durations (τ_{WP}) support fast SoC restoration. The parameters τ_{LT} and τ_{WP} are representative of the conditions of the electricity market. By contrast, the averaging period (τ_{MA}) is a parameter that can be selected by the battery operator. In general, the shorter the averaging period, the faster imbalances can be compensated. In this context it is important to note that a new working point can only be set if a new energy contract can be traded. As a new working point is set at the end of each averaging period, the duration of the averaging period must be at least equal to the contract duration. In the PCR model, $\tau_{MA} = \tau_{WP}$, as this parameter choice offers the greatest possible flexibility for SoC control.

The working point must be set to a value that complies with the charge and discharge power limits of the battery system. In addition, the battery system must be able to provide the full regulation capacity ($P_t^{PCR} \in [-1,1]$) also during SoC restoration [138], which reduces the range of feasible working points. Eq. (4.18) defines the range of feasible working points:

$$|P_t^{WP}| \leq \frac{r_{bat}\, C_{bat}\, SoH_{bat}}{C^{PCR}} - 1, \qquad \forall t. \tag{4.18}$$

Three cases are distinguished to compute the actual working point:

$$P_t^{WP} = \begin{cases} P_t^{WP_{ant}} & \text{if} \quad |P_t^{WP_{ant}}| \leq \frac{r_{bat}\, C_{bat}\, SoH_{bat}}{C^{PCR}} - 1, \\ \frac{r_{bat}\, C_{bat}\, SoH_{bat}}{C^{PCR}} - 1 & \text{if} \quad P_t^{WP_{ant}} > \frac{r_{bat}\, C_{bat}\, SoH_{bat}}{C^{PCR}} - 1, \\ -1 \cdot \left(\frac{r_{bat}\, C_{bat}\, SoH_{bat}}{C^{PCR}} - 1\right) & \text{if} \quad P_t^{WP_{ant}} < -1 \cdot \left(\frac{r_{bat}\, C_{bat}\, SoH_{bat}}{C^{PCR}} - 1\right), \end{cases} \tag{4.19}$$

where in the first case the anticipated working point is compatible with constraint (4.18), hence $P_t^{WP} = P_t^{WP_{ant}}$, and $P_t^{WP_{diff}} = 0$. In the second and third case, the anticipated working point is *not* feasible due to limits on the battery charge and discharge power, respectively. Therefore, the (actual) working point is set to a lower (case 2) or less negative (case 3) value. This ensures that the battery system is able to provide the full regulation capacity while restoring its SoC level.

Power losses in the battery system (P_t^{Loss}) $[MW/MW]$ are modeled as follows [143]:

$$P_t^{Loss} = \begin{cases} (1 - \eta^{tot}) P_t^{Ext} & \text{if} \quad P_t^{Ext} \geq 0, \\ (1 - \frac{1}{\eta^{tot}}) P_t^{Ext} & \text{if} \quad P_t^{Ext} < 0, \end{cases} \tag{4.20}$$

where η^{tot} $[-]$ denotes the one-way energy efficiency of the battery system.

The control signal (P_t^{PCR}) is proportional to the deviation between the actual (f_t) and nominal (f^{nom}) grid frequency. If $f_t \geq 50.20\,Hz$, the full *negative* PCR capacity is activated. If $f_t \leq 49.80\,Hz$, the full *positive* PCR capacity is activated. [138, 142]

$$P_t^{PCR} = \begin{cases} +1 & \text{if} \quad f_t > 50.20, \\ \frac{f_t - f^{nom}}{0.20} & \text{if} \quad f_t \in [49.80, 50.20], \\ -1 & \text{if} \quad f_t < 49.80. \end{cases} \tag{4.21}$$

4.4.3 *Offered PCR capacity*

Constraint (4.22) is introduced to limit the number of cycles per year (N^{ref}) to N_{max}^{ref}, which is defined as the ratio of the cycle (EoL_{cyc}) and calendar (EoL_{cal}) battery lifetime. This ensures that the battery remains operational until the end of its calendar lifetime. A more detailed discussion of long-term dispatch planning via constraint (4.22) is provided in chapter 4.5.

$$N^{ref} \;\leq\; N_{max}^{ref} \;:=\; \frac{EoL_{cyc}}{EoL_{cal}}. \tag{4.22}$$

The number of cycles (N^{ref}) is modeled as discussed for the PSPA model (see chapter 4.2):

$$N^{ref} = \sum_c n_c \cdot \left(\frac{\delta_c}{\delta_{ref}}\right)^W, \tag{4.23}$$

where n_c and δ_c are the cycle count ($n_c = 0.5$ for half cycles and $n_c = 1$ for full cycles) and depth of discharge, respectively, of each cycle c identified by the Rainflow algorithm, δ_{ref} denotes the depth of discharge of a reference cycle, and W is the technology-specific Wöhler coefficient.

First, the number of cycles (N^{ref}) is evaluated that the battery would incur when providing the theoretical PCR capacity (C_{theor}^{PCR}) under a historical time series of the grid frequency. If $N^{ref} \leq N_{max}^{ref}$, provision of the theoretical PCR capacity is considered to be compatible with constraint (4.22). Hence, the offered PCR capacity $C_{offered}^{PCR} = C_{theor}^{PCR}$. Otherwise, the (offered) PCR capacity is decreased until the constraint (4.22) is

satisfied.[15]

In eq. (4.24), the yearly revenues $\left(R_y^{PCR}\right)$ are computed. R_y^{PCR} is dependent on the offered PCR capacity $\left(C_{offered}^{PCR}\right)$[16] $[MW]$, the average remuneration for PCR provision $\left(\overline{\pi}^{PCR}\right)$[17] $[EUR/(MW \cdot yr)]$, and the costs of SoC restoration. The costs of SoC restoration are computed from the working point of the battery $\left(P_t^{WP}\right)$ and the electricity costs $\left(\pi_t^{WP}\right)$ $[EUR/MWh]$ during each time step.

$$R_y^{PCR} = C_{offered}^{PCR} \cdot \left(\overline{\pi}^{PCR} - \frac{\tau}{3600} \sum_{t=1}^{T} P_t^{WP} \pi_t^{WP} \right), \tag{4.24}$$

where $\tau := 1s$ is the time step length and $T = 31{,}536{,}000$ is the number of time steps per year.

The revenues R_y^{PCR} are computed for each year of the PCR project as described above taking into account that the state of health and energy efficiency of the battery system deteriorate over time (see chapter 4.5). The economic assessment of different technologies and system configurations is performed based on battery profitability.

[15] As mentioned above, the PCR model assumes that any integer multiple of $0.01\,MW$ up to $25\,MW$ can be provided, i.e., $C_{offered}^{PCR} \in \{0.01, 0.02, \ldots, 25.00\}$. Hence, the offered PCR capacity is determined by subtracting from the theoretical PCR capacity $0.01\,MW$ multiple times until constraint (4.22) is satisfied.

[16] The PCR model assumes that the battery system provides the same PCR capacity over the entire year.

[17] In the case of *pay-as-bid* PCR capacity auctions, $\overline{\pi}^{PCR}$ denotes the average remuneration for *accepted* PCR bids (see chapter 5.5.1 for the details).

4.5 DEGRADATION MODEL

This chapter details the assumptions made in the PSPA and PCR models for battery degradation and lifetime assessment and provides a discussion of possible model limitations. First, a short overview of stress factors affecting cycle and calendar ageing is given, along with a critical evaluation of stress factors that are neglected in the PSPA and PCR models. Then, the model assumptions are discussed that allow formulating the long-term dispatch scheduling of stationary battery systems as an allocation problem. This discussion motivates the implementation of an operational constraint in the PSPA and PCR models that limits the number of cycles per year to the ratio of the cycle and calendar battery lifetime. Last, a simple empirical model is presented that relates the output of the used semi-empirical degradation model to battery performance metrics of practical interest, including SoH and energy efficiency.

4.5.1 *Model assumptions*

Cycle ageing is assessed by counting the number of equivalent cycles (N^{ref}):

$$N^{ref} = \sum_{c} n_c \cdot \left(\frac{\delta_c}{\delta_{ref}} \right)^{W}, \tag{4.25}$$

where n_c and δ_c are the cycle count ($n_c = 0.5$ for half cycles and $n_c = 1$ for full cycles) and depth of discharge, respectively, of each cycle c identified by the Rainflow algorithm, δ_{ref} denotes the depth of discharge of a reference cycle, and W is the technology-specific Wöhler coefficient.

In contrast to cycle ageing (eq. 4.25), calendar ageing is not explicitly modeled, because it is assumed to be constant (i.e., not dependent on battery dispatch). As such, the stress factors that are considered in the PSPA and PCR models include time (t) (calendar ageing) and the depth of discharge (δ_c) (cycle ageing). Other stress factors that could have an impact on battery ageing, such as the SoC level ($\overline{\sigma}$ and σ_c), current rate (r_c), and temperature ($\overline{T}$ and T_c), are neglected (see chapter 2.3.3 for a review of semi-empirical degradation models). In the following, the validity of these assumptions is discussed for the application cases considered in the PSPA and PCR models.

- *Average SoC level ($\overline{\sigma}$).* The adverse impact of high SoC levels on calendar ageing (see chapter 2.3) is neglected for the following reasons: The SoC of battery systems providing PS and PA is bound to 50% at the beginning and end of each dispatch period if $SoC^{init} = 50\%$ in eq. (4.4c) and $SoC^{end} = 50\%$ in eq. (4.4e), which

are generally suitable model assumptions. Hence, the batteries generally experience moderate SoC levels. Similarly, battery systems providing PCR are operated at a SoC level close to 50% most of the time when a moving-average based SoC control scheme is applied.

- *Average cycle SoC (σ_c).* The average SoC during charge/discharge cycles is not considered as a stress factor, as ageing is lowest for cycles that are centered at a SoC level close to 50% [53, 61]. This is generally the case for batteries providing PS, PA, and PCR services.

- *Temperature ($\overline{T}$ and T_c).* Battery systems in stationary applications are typically operated under temperature-controlled conditions in order to keep the battery cells close to the ideal operating temperature. Hence, the detrimental impact of extreme temperatures on calendar and cycle ageing can be neglected. It should be noted that temperature control may have cost implications, resulting in higher investment and O&M costs for battery systems with high power ratings (see chapter 5.1 for a discussion of battery system costs).

- *Current rate (r_c).* In many stationary applications, battery systems are operated at moderate current rates most of the time. For instance, when deployed on the day-ahead market where electricity is traded in hourly blocks, batteries are charged or discharged only one time every hour, hence $r_c \leq 1\,MW/MWh$. Depending on the billing scheme and regulatory framework, battery systems providing PS and PCR services may experience higher current rates but generally do so only for relatively short periods of time. For theses reasons, the current rate (r_c) is not considered as a stress factor in the PSPA and PCR models.

4.5.2 *Long-term dispatch scheduling*

A practical approach to parameterize battery degradation models relies on cycle and calendar lifetime data provided by battery manufacturers. Under this modeling approach, batteries are considered operational until they reach the end of either the cycle or calendar lifetime.[18] [7, 23] This allows the long-term battery dispatch planning to be formulated as an allocation problem. The objective is to distribute the charge and discharge cycles (i.e., cycle lifetime) over the calendar lifetime of the battery so

[18] This modeling approach assumes that cycle and calendar ageing processes are completely independent phenomena. This assumption is not generally valid from an electrochemical point of view, and the lifetime of batteries performing a very low or a very high number of cycles per year may be underestimated using this approach. In these cases, additive ($L_{tot} = L_{cal} + L_{cyc}$) or multiplicative ($L_{tot} = L_{cal} \cdot L_{cal}$) models could potentially provide more accurate estimates for the battery lifetime (see chapter 2.3.3.2 for a discussion of additive, multiplicative, and maximum-based degradation models). In the following, a maximum-based approach is employed, as it allows for the parameterization of the degradation model using cycle and calendar lifetime data provided by battery manufacturers. A short discussion of alternative PSPA and PCR model formulations that are compatible with additive and multiplicative degradation models is provided in chapter 6.

as to maximize the lifetime revenues. In the PSPA and PCR models presented in chapter 4.2 and 4.4, respectively, the lifetime revenues are determined in a two-step procedure: The first step entails the short-term dispatch modeling, whereas the second step allocates the number of cycles within each year. [72, 75]

The operational constraint (4.26) limits the number of cycles per year to the ratio of the cycle and calendar battery lifetime (see eq. (4.11b) for the PSPA model and eq. (4.22) for the PCR model):

$$N^{ref} \leq \frac{EoL_{cyc}}{EoL_{cal}}. \tag{4.26}$$

Eq. (4.26) ensures (i) that the battery remains operational until the end of its calendar lifetime (hence, the battery lifetime $EoL_{bat} = EoL_{cal}$), and (ii) that the battery performs the same number of cycles in each year.[19] Under constraint (4.26), the long-term dispatch scheduling of battery systems simplifies to solving an independent allocation problem for each year and subsequently aggregating the (discounted) yearly revenues to assess the lifetime revenues. It should be noted that this modeling approach does not allow the battery operator to account for possible long-term changes in the revenue opportunities. For instance, if the marginal revenues per unit degradation ($\partial R / \partial N^{ref}$) decrease over time due to changing electricity market conditions, the battery system should be operated more frequently in the first years than in subsequent years. Similarly, under high discount rates (and thus decreasing *discounted* marginal revenues), battery systems should be operated more frequently at the beginning of their lifetime (see Ref. [72]). Hence, in order to ensure optimality of the long-term dispatch schedules, constraint (4.26) should be implemented only if the revenue opportunities are expected to be relatively similar in each year.[20]

4.5.3 *Battery performance deterioration*

Batteries that perform the same number of cycles in each year incur degradation linearly in time. The cumulative degradation ($L^N_{tot} \in [0,1]$) incurred up to year y can therefore be expressed as follows:

$$L^N_{tot}(y) = \frac{y}{EoL_{bat}}, \tag{4.27}$$

[19] More precisely, the battery system performs the same number of cycles if the constraint (4.26) is binding (i.e., the cycle lifetime constitutes a limiting factor, which often is the case). By contrast, if constraint (4.26) is *not* binding, the number of cycles may vary somewhat across different years.

[20] Chapter 5 presents case studies for the deployment of stationary battery systems under different electricity market scenarios. Whereas each scenario is defined in terms of historical or simulated electricity market data for one year, the data is considered representative for all years of battery operation. Hence, the modeling approach of solving independent allocation problems for each year is suitable.

where EoL_{bat} denotes the lifetime of the battery in years. It should be noted that this modeling approach assumes that battery degradation is a Markov process, that is, the rate of degradation is not dependent on the degradation history of the battery [72].

The relationship between the cumulative degradation (L_{tot}^{N}) and performance metrics of practical interest, including the battery state of health (SoH_{bat}) and the energy efficiency of the battery pack (η^{bat}), can be modeled using empirical relationships [47, 69, 74, 147]. In the PSPA and PCR models, the battery state of health (SoH_{bat}) is computed as follows:

$$SoH_{bat}(y) = 1 - (1 - SoH_{EoL})\sqrt{L_{tot}^{N}(y)}, \tag{4.28}$$

where SoH_{EoL} is the battery state of health at the end of its lifetime, denoting the ratio of the current and initial energy capacity.

The energy efficiency of the battery pack (η^{bat}) is modeled using eq. (4.29), which is derived from empirical degradation tests on NMC Li-ion batteries [147]. The energy efficiency is expressed as a function of the state of health:

$$\eta^{bat} = \left(1 - \frac{1 - \eta^{bat,0}}{1 - \sqrt{0.9582}}\right) \cdot \left(1 - \sqrt{-0.2303(1 - SoH_{bat}) + 0.9582}\right), \tag{4.29}$$

where $\eta^{bat,0}$ denotes the energy efficiency of the new battery pack. The one-way energy efficiency of the battery system (η^{tot}) is the product of the battery pack efficiency (η^{bat}) and the efficiency of the power components (η^{iv}), which includes AC/DC inverters and transformers:

$$\eta^{tot} = \eta^{bat}\eta^{iv}. \tag{4.30}$$

While the efficiency of power components (η^{iv}) is assumed to be constant, the efficiency of the battery pack (η^{bat}) is subject to degradation and hence decreases over time.

The energy efficiencies in eq. (4.30) are dependent on the current rate. In contrast to the battery pack efficiency (η^{bat}), which decreases at higher current rates, the efficiency of the power units (η^{iv}) generally increases. [62] As a consequence, the efficiency of the battery system (η^{tot}) is relatively constant over a wide range of current rates. Therefore, the dependency on the current rate is neglected in the PSPA and PCR models.

4.6 SUMMARY

In this chapter, a modeling framework for the technical and economic assessment of battery systems deployed in different stationary applications was presented. First, the *PSPA model* was developed, which is a multi-objective optimization model that maximizes the lifetime revenues of battery systems providing (combined) PS and PA services. Implementation of the Rainflow cycle counting algorithm ensures that the degradation of batteries can be modeled using technology-specific empirical fitting functions, which allows for an advanced representation of cycle degradation in the optimization model. Second, a methodology for time series clustering was presented that is used in the PSPA model to select a small number of representative load profiles and electricity price curves from larger data sets. Then, the *PCR model* was developed, which is a simulation model to analyze the provision of PCR under different electricity market conditions. The chapter concluded with a critical discussion of the assumptions made in the PSPA and PCR models for battery degradation and lifetime assessment. In the following chapter, the developed modeling framework will be applied to various case studies and business cases.

5

CASE STUDIES

Based on the modeling framework outlined in chapter 4, this chapter discusses a number of case studies to assess the provision of PS, PA, and PCR services under a wide range of electricity market conditions. First, a battery system cost model is presented, which will be used to assess and compare the profitability of varying battery system configurations. Then, the operation, profitability, and technical suitability of battery systems providing PS, PA, and PCR services is analyzed. Based on the results, the chapter concludes by providing suggestions on the prioritization of different research and development targets related to the performance of today's battery systems.

5.1 BATTERY SYSTEM PROFITABILITY

The profitability of battery systems is evaluated based on the ratio of the lifetime revenues and lifetime costs:

$$PI_{bat} := \frac{R_{LT}}{c_{LT}}, \tag{5.1}$$

where PI_{bat} is the profitability index, R_{LT} $[EUR]$ denotes the lifetime revenues, and c_{LT} $[EUR]$ denotes the lifetime costs. The lifetime revenues (R_{LT}) are the sum of all discounted revenues of the battery system during its lifetime. The lifetime costs (c_{LT}) are all discounted costs, including the investment costs of the battery system, replacement costs of battery system components, and O&M costs. The profitability index defined in eq. (5.1) differs somewhat from more commonly used definitions of the profitability index (see Ref. [148]), which account for replacement and O&M costs as negative cash flows prorated to the lifetime revenues (R_{LT}). The definition in eq. (5.1) is used in this thesis, as it provides a proportional relationship between battery profitability and the lifetime costs, which will allow for a straightforward evaluation of battery system cost reduction targets. Profitability indices higher than one indicate that the lifetime revenues exceed the lifetime costs, hence battery deployment is profitable. By contrast, battery deployment is not profitable if $PI_{bat} < 1$.

The lifetime revenues (R_{LT}) are the sum of the discounted revenues in each year:

$$R_{LT} = \sum_{y=1}^{EoL_{bat}} R_y \left(1 + \frac{r_d}{100}\right)^{-y}, \tag{5.2}$$

where R_y denotes the revenues in each year, r_d [%] is the discount rate, and EoL_{bat} is the lifetime of the battery packs.

The battery system is considered operational until the battery packs reach the end of their lifetime. If the lifetime of the battery packs (EoL_{bat}) exceeds the lifetime of AC/DC power inverters (L_{iv}), the inverters must be replaced, which increases the lifetime costs (c_{LT}). Conversely, if $EoL_{bat} < L_{iv}$, the AC/DC power inverters are assumed to still have an economic value when the battery packs reach the end of their lifetime, which reduces the lifetime costs (c_{LT}).

The lifetime costs (c_{LT}) are modeled by eq. (5.3). They include the investment costs of the battery system (c_{sys}), the replacement costs of AC/DC power inverters, and the sum of the discounted O&M costs over all years:

$$c_{LT} = c_{sys} + \underbrace{\phi_{iv}^{Rep} \cdot C_{bat} \cdot r_{bat} \cdot c_{iv}}_{\substack{\text{replacement costs AC/DC} \\ \text{power inverters}}} + \underbrace{\sum_{y=1}^{EoL_{bat}} c_{O\&M} \cdot \left(1 + \frac{r_d}{100}\right)^{-y}}_{\text{O\&M costs}}. \tag{5.3}$$

The replacement costs of AC/DC power inverters in eq. (5.3) depend on the costs of the AC/DC power inverters (c_{iv}) $[EUR/MW]$, the power rating of the battery system (r_{bat}) $[MW/MWh]$, the energy capacity of the battery system (C_{bat}) $[MWh]$, and the replacement cost factor $\left(\phi_{iv}^{Rep}\right)$ $[-]$. The replacement cost factor is modeled by eq. (5.4). It depends on the lifetime of the battery packs (EoL_{bat}), the lifetime of AC/DC power inverters (L_{iv}), and the discount rate (r_d). If $EoL_{bat} = L_{iv}$, the replacement cost factor $\phi_{iv}^{Rep} = 0$. Otherwise, ϕ_{iv}^{Rep} takes a negative ($EoL_{bat} < L_{iv}$) or positive ($EoL_{bat} > L_{iv}$) value:

$$\phi_{iv}^{Rep} = \begin{cases} -\left(\frac{L_{iv} - EoL_{bat}}{L_{iv}}\right)\left(1 + \frac{r_d}{100}\right)^{-EoL_{bat}} & \text{if} \quad EoL_{bat} < L_{iv}, \\ 0 & \text{if} \quad EoL_{bat} = L_{iv}, \\ \left(1 + \frac{r_d}{100}\right)^{-L_{iv}} - \left(\frac{2 \cdot L_{iv} - EoL_{bat}}{L_{iv}}\right)\left(1 + \frac{r_d}{100}\right)^{-EoL_{bat}} & \text{if} \quad L_{iv} < EoL_{bat} \leq 2L_{iv}, \\ \left(1 + \frac{r_d}{100}\right)^{-L_{iv}} + \left(1 + \frac{r_d}{100}\right)^{-2L_{iv}} - \left(\frac{3 \cdot L_{iv} - EoL_{bat}}{L_{iv}}\right)\left(1 + \frac{r_d}{100}\right)^{-EoL_{bat}} & \text{if} \quad 2L_{iv} < EoL_{bat} \leq 3L_{iv}. \end{cases} \tag{5.4}$$

The yearly O&M costs ($c_{O\&M}$) $[EUR/yr]$ in eq. (5.3) are assumed to amount to 2% of the battery system investment costs [141]:

$$c_{O\&M} = 0.02\, c_{sys}. \tag{5.5}$$

The battery system costs (c_{sys}) $[EUR]$ are modeled by eq. (5.6). They are the sum of the investment costs of the battery packs and the investment costs of battery power

components. The latter scale mainly with the maximum charge/discharge power of the battery system. They include the costs of the energy management system, thermal management system, cooling system, AC/DC power inverters, and transformers. [4, 7]

$$c_{sys} = \underbrace{C_{bat} \cdot c_{pack}}_{\substack{\text{battery pack} \\ \text{costs}}} + \underbrace{C_{bat} \cdot r_{bat} \cdot c_{power}}_{\substack{\text{power component} \\ \text{costs}}}, \tag{5.6}$$

where c_{pack} $[EUR/MWh]$ denotes the battery pack costs, and c_{power} $[EUR/MW]$ are the costs of battery power components.

The costs of battery packs (c_{pack}) with different power ratings (r_{bat}) are modeled based on cost estimates for NMC/Graphite LIB cells optimized for varying low to very high discharge rates. This modeling approach accounts for the fact that, for the same capacity, *high power* cells are significantly more expensive than *high energy* cells due to higher material requirements and manufacturing processes that are more resource and labor intensive. Figure 5.1 shows cost estimates for battery cells (blue) and battery packs (red). For the details of the cost assessment, the interested reader is referred to chapter 3 of this thesis and references cited therein.

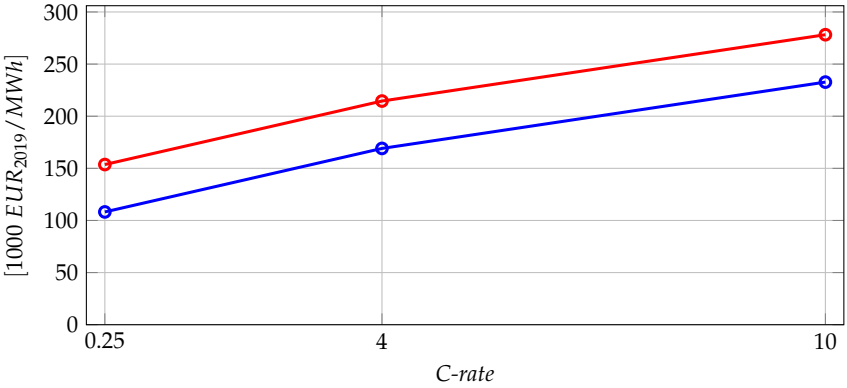

FIGURE 5.1: Costs of battery cells (blue circles) and battery packs (red circles) optimized for varying galvanostatic discharge rates: $0.25\,C$ ($r_{bat} \approx 0.25\,MW/MWh$), $4\,C$ ($r_{bat} \approx 4\,MW/MWh$), and $10\,C$ ($r_{bat} \approx 10\,MW/MWh$). Cost estimates for battery cells and battery packs optimized for other C-rates are obtained by linear interpolation (solid lines). Battery pack assembly costs of 45,000 EUR_{2019}/MWh are assumed [121]. The details of the battery cell cost model are discussed in chapter 3 of this thesis and references cited therein.

5.2 BATTERY RESEARCH TARGETS

In order to evaluate which technical performance metrics have the greatest impact on the economic viability of stationary battery systems, the economic benefits of

improving the following parameters are examined: (i) cycle lifetime (number of equivalent cycles until the battery packs reach 80% SoH), (ii) calendar lifetime (number of years until the battery packs reach 80% SoH), (iii) second life usability (indicating whether or not the battery packs can be operated beyond 80% SoH[1]), and (iv) energy efficiency of new[2] battery packs. The goal is to assess the economic benefits of improving each of these parameters from a base value (representative of today's LIBs) to an enhanced target value that could be attained within the next decade or so with continued research efforts. Consideration of two values for each parameter results in 15 development scenarios (table 5.1). Scenario 0 is representative of the performance of today's LIBs. Scenarios 1 - 4 refer to the improvement of a single parameter. Scenarios 5 - 15 refer to the improvement of two or more parameters at the same time. The parameter values were selected based on Refs. [7, 149].

Figure 5.2 shows the deterioration of battery performance under the development scenarios defined in table 5.1. The x-axes are normalized by the number of years until the battery packs reach 80% SoH. As discussed in chapter 4.5, battery packs are considered operational until they reach the end of either the cycle or calendar lifetime. Hence, for battery packs that perform the same number of cycles in each year (corresponding to the ratio of the cycle and calendar lifetime), the lifetime of the battery coincides with its calendar lifetime (EoL_{cal}^{80}). The decline in SoH (blue) is assumed to follow a square-root dependence on time, whereas the evolution of the energy efficiency (orange) is modeled based on empirical relationships between SoH and energy efficiency (see chapter 4.5 for the details). Battery packs without a second life (left) are considered operational until they reach 80% SoH. By contrast, battery packs with a second life (right) are assumed to be operational for twice the number of years. The evolution of the battery system energy efficiency is shown for battery packs with initial energy efficiencies of 95% (solid orange lines) and 97% (dashed orange lines).

The remainder of this chapter is organized as follows: Chapter 5.3 - 5.5 present an economic assessment of stationary battery systems under the development scenarios in table 5.1. Based on the results, chapter 5.6 ranks the relative importance of the different research targets by their economic benefits from the viewpoint of a battery system operator providing PS, PA, and PCR services.

[1] Experimental degradation studies have found a rapid increase of the degradation rate in battery cells that are nearing the end of their lifetime. The onset of accelerated degradation at ca. 80% SoH could be avoided by improving the materials and design of the battery cells. [11, 73, 88]

[2] As discussed in chapter 4.5, both the SoH and energy efficiency deteriorate as the battery cells degrade.

TABLE 5.1: Development scenarios for LIBs. The labels of the scenarios 1 - 15 indicate the parameters that are improved with respect to the performance of today's LIBs (scenario 0): cycle lifetime (Cy), calendar lifetime (Ca), energy efficiency (η), and second life (SL) usability. The second life (SL) usability indicates whether or not battery packs can be operated beyond 80% SoH. The columns on the right-hand side show the parameter values: EoL_{cyc}^{80} and EoL_{cal}^{80} denote the number of cycles and the number of years until the battery packs reach 80% SoH, respectively. By contrast, EoL_{cyc} and EoL_{cal} denote the number of cycles and the number of years until the battery packs reach the end of their lifetime, respectively. For battery packs that reach the end of their lifetime at 80% SoH (no SL), $EoL_{cyc} = EoL_{cyc}^{80}$ and $EoL_{cal} = EoL_{cal}^{80}$. By contrast, for battery packs that can be operated beyond 80% SoH, $EoL_{cyc} = 2\,EoL_{cyc}^{80}$ and $EoL_{cal} = 2\,EoL_{cal}^{80}$. The last column of the table indicates the energy efficiency of new battery packs ($\eta^{bat,0}$). The efficiency of power inverters ($\eta^{iv} = 97\%$) is considered separately. The parameters for the different development scenarios were selected based on Refs. [7, 149].

#	Scenario label	EoL_{cyc}^{80} $[cycles]$	EoL_{cal}^{80} $[yr]$	EoL_{cyc} $[cycles]$	EoL_{cal} $[yr]$	$\eta^{bat,0}$ [%]
0	*base (today)*	6,000	15	6,000	15	95
1	Cy	25,000	15	25,000	15	95
2	Ca	6,000	20	6,000	20	95
3	η	6,000	15	6,000	15	97
4	SL	6,000	15	12,000	30	95
5	$Cy + Ca$	25,000	20	25,000	20	95
6	$Cy + \eta$	25,000	15	25,000	15	97
7	$Cy + SL$	25,000	15	50,000	30	95
8	$Ca + \eta$	6,000	20	6,000	20	97
9	$Ca + SL$	6,000	20	12,000	40	95
10	$\eta + SL$	6,000	15	12,000	30	97
11	$Ca + \eta + SL$	6,000	20	12,000	40	97
12	$Cy + \eta + SL$	25,000	15	50,000	30	97
13	$Cy + Ca + SL$	25,000	20	50,000	40	95
14	$Cy + Ca + \eta$	25,000	20	25,000	20	97
15	$Cy + Ca + \eta + SL$	25,000	20	50,000	40	97

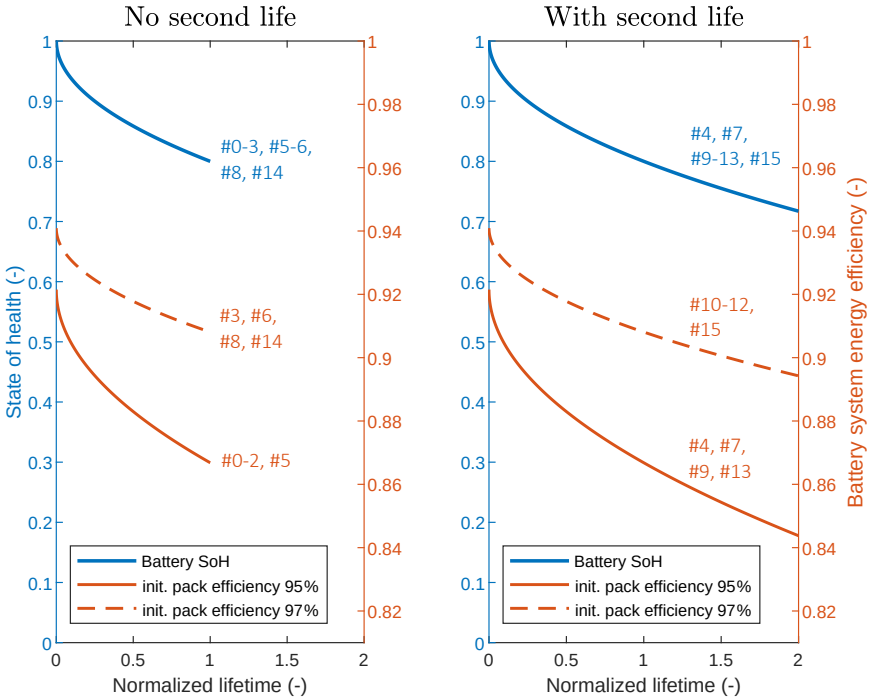

FIGURE 5.2: Deterioration of battery performance under the development scenarios (#0 - 15) defined in table 5.1. The x-axes are normalized by the number of years until the battery packs reach the end of their first lifetime (which is assumed to be the case after 15 - 20 years). The decline of the battery SoH is shown in blue. The evolution of the battery system energy efficiency (η^{tot}) is shown in orange for battery packs with initial efficiencies $\eta^{bat,0} = 95\%$ (solid lines) and $\eta^{bat,0} = 97\%$ (dashed lines). The efficiency of the battery system is the product of the battery pack and inverter efficiency: $\eta^{tot} = \eta^{bat} \cdot \eta^{iv}$. The figure was created based on data provided in Refs. [69, 147].

5.3 CASE STUDIES FOR PRICE ARBITRAGE

This chapter discusses the economics of using rechargeable batteries for PA, where revenues are generated by exploiting temporal price differences on electricity markets.

5.3.1 *Model input data*

In order to analyze the provision of PA services under a wide range of electricity market conditions, the following case studies are considered (see figure 5.3):

- Case study I (*PAd18*): PA on the day-ahead electricity market in Switzerland from October 2017 to September 2018.
- Case study II (*PAd19*): PA on the day-ahead electricity market in Switzerland in the year 2019.
- Case study III (*PAi18*): PA on the intraday electricity market in Germany in the year 2018.
- Case study IV (*PAi19*): PA on the intraday electricity market in Germany in the year 2019.
- Case study V (*PA30*): PA in Switzerland in the year 2030 (simulated prices).
- Case study VI (*PA50*): PA in Switzerland in the year 2050 (simulated prices).

In each case study, the PSPA model input comprises historical or simulated time series data of the electricity price for one year. In case studies I - IV, historical data from *EPEX spot* is used. In case studies V - VI, simulated prices from Ref. [150] are used, which were obtained using a detailed electricity market model. In order to analyze the impact of future electricity market conditions with high price volatility on PA revenues, the *energy-only market* (EOM) scenario (see Ref. [150]) is considered in this thesis. Besides increased shares of renewable energy sources, the EOM scenario assumes that pure electricity markets are implemented in Switzerland and neighboring countries, in which the entire income of flexible power plants is generated by selling electricity on the wholesale market, i.e., power plants are not additionally remunerated for their capacity [150].

Figure 5.3 shows the electricity prices considered as case studies. The electricity prices V - VI (light blue) are shown on a different scale, as the price peaks are significantly higher than in case studies I - IV (dark blue).

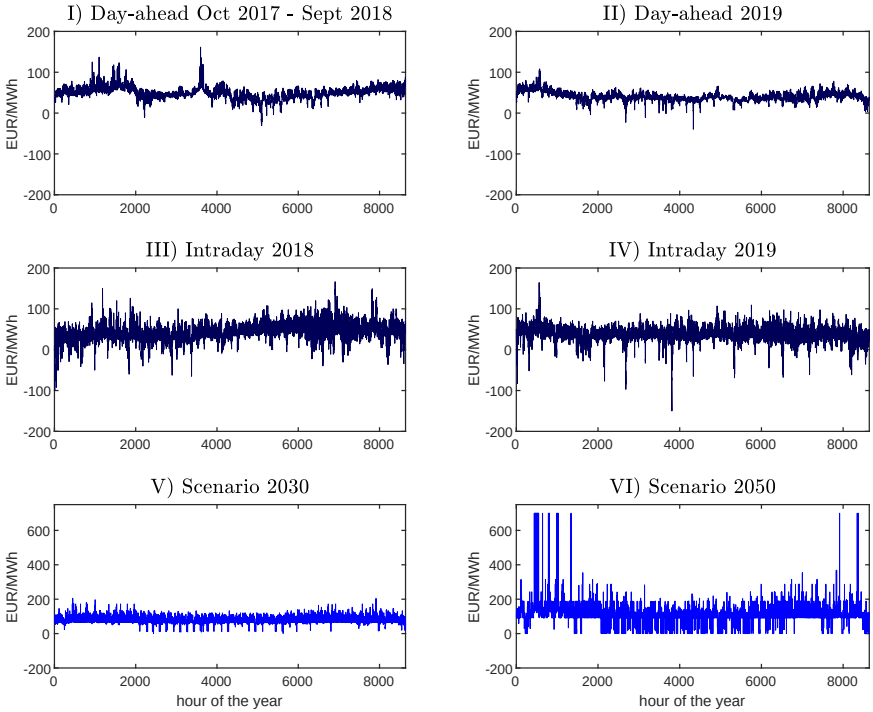

FIGURE 5.3: Electricity prices considered as case studies. I-II): day-ahead electricity market (1 year, Switzerland, hourly resolution). III-IV): intraday electricity market (1 year, Germany, 15*min* resolution). V-VI): Simulated electricity prices for the years 2030 and 2050 (1 year, Switzerland, hourly resolution).

The following model assumptions are made:

- The battery operator is assumed to be a price taker, hence the electricity prices are provided as an external model input.
- Perfect foresight of the electricity price is assumed to ensure that the battery operator can realize the maximum possible PA revenues. In practice, the revenues might be somewhat lower due to forecast errors in the electricity price and thus suboptimal dispatch schedules. However, the negative impact of forecast errors on PA revenues could be mitigated by adapting (i.e., recomputing) the dispatch schedules as more recent forecasts become available.
- The same electricity price data is used to assess PA revenues in all years of battery operation.
- The operation of battery systems is optimized for non-overlapping dispatch periods (i.e., optimization horizons) of 3 days. The battery SoC at the beginning (SoC^{init}) and end (SoC^{end}) of each dispatch period is set to 50%.
- For each year, the operation of battery systems is modeled for 10 *typical* dispatch periods. The *typical* time series of the electricity price were obtained by applying the clustering algorithm described in chapter 4.3.1.

5.3.2 *Clustering of electricity prices*

Figure 5.4 provides an example illustrating the clustering of time series, showing *typical* electricity prices on the German intraday market in 2019 (case study IV). The data was obtained by applying the clustering algorithm described in chapter 4.3.1.[3] For each dispatch period of 72 hours, the *representative* time series (as defined by the clustering algorithm) is highlighted in red. All other time series assigned to the same dispatch period are shown in black.

[3] The performance of the clustering algorithm was validated by comparing model results obtained using the clustered input data (i.e., electricity prices during 10 typical dispatch periods) against model results obtained using the full data set (i.e., electricity prices of the full year). In general, the absolute deviation between the different model results in terms of the yearly PA revenues is less than 5 - 10%.

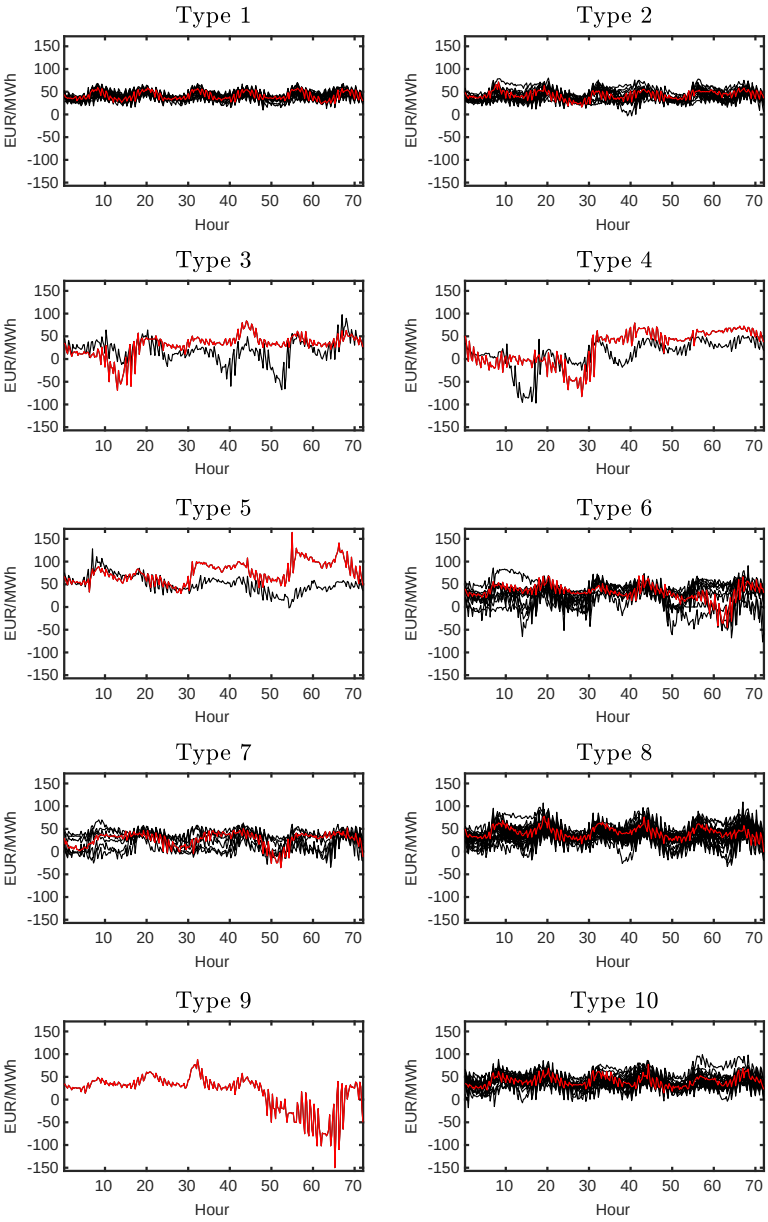

FIGURE 5.4: An example illustrating the clustering of time series, showing *typical* electricity prices on the German intraday electricity market in 2019 (case study IV). The data was obtained by applying the clustering algorithm described in chapter 4.3.1. For each dispatch period of 72 hours, the representative time series is highlighted in red. All other time series assigned to the same dispatch period are shown in black.

5.3.3 *Battery system operation*

Figure 5.5 and 5.6 show optimal dispatch schedules for battery systems performing PA on the German intraday electricity market. The charge and discharge power is illustrated for dispatch periods of *type* 6 (see figure 5.4) with an optimization horizon of 72 hours and a time step length of 15 minutes. While dispatch periods of *type* 6 are shown as an *example* to illustrate the charge and discharge power, all 10 typical dispatch periods of the whole year were considered for the economic assessment of battery systems. Figure 5.5 shows model results for batteries with Wöhler coefficients $W = 1$, such as LIBs with LFP cathodes [66–68] (see chapter 2.3.3.1). The degradation of these batteries is roughly proportional to the cycle depth (δ) of charge and discharge cycles, that is, $N^{ref} \propto \delta$, where N^{ref} denotes the number of equivalent cycles. Figure 5.6 shows the same model results for batteries with Wöhler coefficients $W = 2$, such as LIBs with NMC cathodes [47, 53, 63] (see chapter 2.3.3.1). The degradation of these batteries scales approximately with the square of the cycle depth, that is, $N^{ref} \propto \delta^2$. Both figures show optimal dispatch schedules for varying values of the degradation cost parameter: $a = 15\,EUR/cycle$ (left), $a = 30\,EUR/cycle$ (middle), and $a = 60\,EUR/cycle$ (right). The top rows show the electricity prices during the dispatch period. The second rows show the battery charge (positive) and discharge (negative) power. The third rows illustrate the evolution of the battery SoC. The last rows show the cumulative degradation.

A comparison of the dispatch schedules obtained for varying values of the degradation cost parameter reveals that the operation of battery systems is strongly affected by the penalty imposed on degradation: For low penalties ($a = 15\,EUR/cycle$), battery systems perform 5.1 - 7.5 equivalent cycles during the dispatch period, whereas higher penalties reduce the degradation to 2.7 - 3.1 ($a = 30\,EUR/cycle$) or 1.2 - 1.3 ($a = 60\,EUR/cycle$) equivalent cycles. The results illustrate that, as expected, higher penalties on battery degradation reduce the number of cycles at the expense of lower PA revenues (see the legends of figure 5.5 and 5.6 for the details).

Regardless of the penalty imposed on degradation, the dispatch schedules are fundamentally different for batteries with $W = 1$ (figure 5.5) and $W = 2$ (figure 5.6). Batteries with $W = 1$ are operated either at zero or at the maximum charge/discharge power most of the time and experience mainly *deep* cycles. By contrast, batteries with $W = 2$ are charged and discharged more frequently but generally only at a fraction of the maximum rate. As a consequence, these batteries perform significantly more *shallow* than *deep* cycles, especially under high penalties on battery degradation. The differences in the dispatch schedules can be ascribed to the different marginal degradation cost functions of the two battery technologies: Whereas batteries with $W = 1$ incur con-

stant marginal degradation costs ($\partial\gamma/\partial\delta$) for charging and discharging, the marginal costs of degradation increase linearly with DoD (δ) for batteries with $W = 2$:

$$\frac{\partial\gamma}{\partial\delta} = \frac{a}{\delta_{ref}} \qquad \text{for} \quad W = 1, \tag{5.7a}$$

$$\frac{\partial\gamma}{\partial\delta} = \frac{2a}{\delta_{ref}^2}\,\delta \qquad \text{for} \quad W = 2, \tag{5.7b}$$

where a $[EUR/cycle]$ is the degradation cost parameter, and $\delta_{ref} := 80\%$ denotes the DoD of a reference cycle.

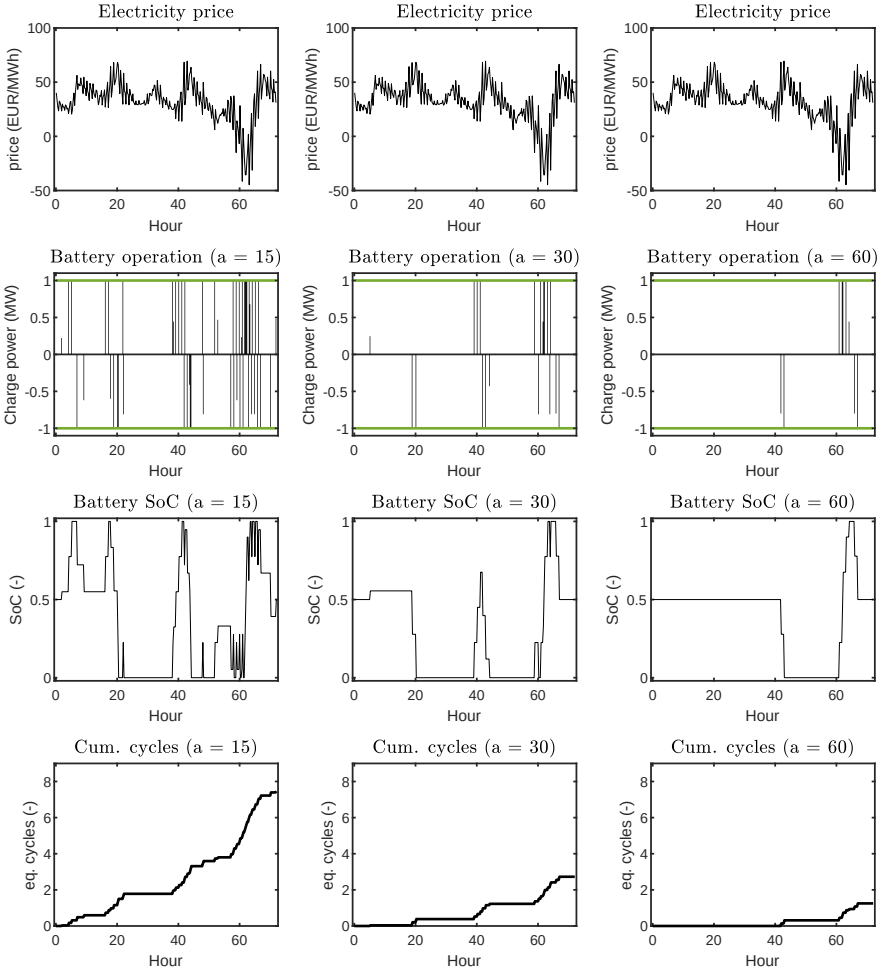

FIGURE 5.5: Optimal dispatch schedules for batteries with Wöhler coefficients $W = 1$ performing PA on the German intraday market. The battery charge and discharge power is illustrated for dispatch periods of *type* 6 (see figure 5.4). The model results were obtained for battery systems with the following parameters: energy capacity (C_{bat}): $1\,MWh$, power rating (r_{bat}): $1\,MW/MWh$, battery state of health (SoH_{bat}): 100%, energy efficiency of the battery system (η^{tot}): 90%, state of charge at the beginning (SoC^{init}) and end (SoC^{end}) of the dispatch period: 50%. The figure shows optimal dispatch schedules for varying values of the degradation cost parameter: $a = 15\,EUR/cycle$ (left), $a = 30\,EUR/cycle$ (middle), and $a = 60\,EUR/cycle$ (right). The top row shows the electricity prices during the dispatch period. The second row shows the battery charge (positive) and discharge (negative) power, which is constrained to $\pm 1\,MW$ (green lines) due to the limited power rating of the battery system. The third row illustrates the evolution of the battery SoC. The bottom row shows the cumulative degradation (number of equivalent cycles (N^{ref}) at 80% DoD reference condition). Higher values of the degradation cost parameter reduce the number of equivalent cycles (N^{ref}) at the expense of lower PA revenues (R^{PA}): $N^{ref} = 7.46\ cycles$ and $R^{PA} = 253\,EUR$ ($a = 15\,EUR/cycle$); $N^{ref} = 2.73\ cycles$ and $R^{PA} = 155\,EUR$ ($a = 30\,EUR/cycle$); $N^{ref} = 1.25\ cycles$ and $R^{PA} = 103\,EUR$ ($a = 60\,EUR/cycle$).

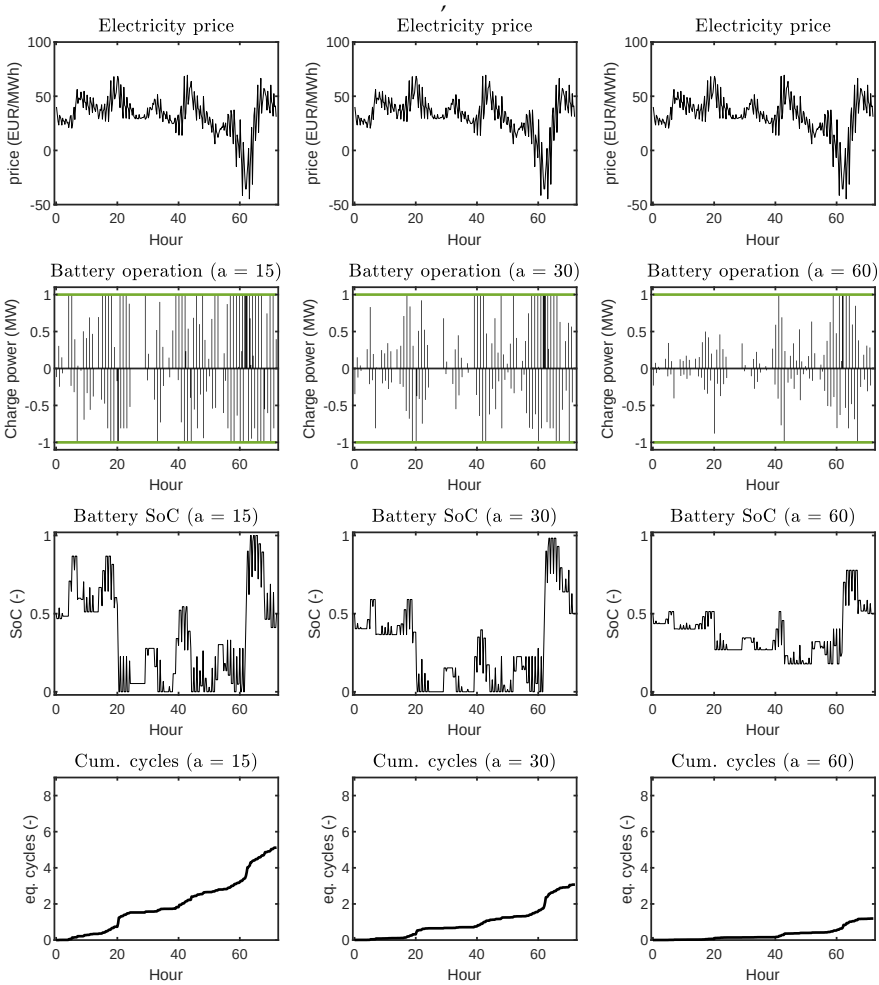

FIGURE 5.6: Optimal dispatch schedules for batteries with Wöhler coefficients $W = 2$ performing PA on the German intraday market. The battery charge and discharge power is illustrated for dispatch periods of *type* 6 (see figure 5.4). The model results were obtained for battery systems with the following parameters: energy capacity (C_{bat}): $1\,MWh$, power rating (r_{bat}): $1\,MW/MWh$, battery state of health (SoH_{bat}): 100%, energy efficiency of the battery system (η^{tot}): 90%, state of charge at the beginning (SoC^{init}) and end (SoC^{end}) of the dispatch period: 50%. The figure shows optimal dispatch schedules for varying values of the degradation cost parameter: $a = 15\,EUR/cycle$ (left), $a = 30\,EUR/cycle$ (middle), and $a = 60\,EUR/cycle$ (right). The top row shows the electricity prices during the dispatch period. The second row shows the battery charge (positive) and discharge (negative) power, which is constrained to $\pm 1\,MW$ (green lines) due to the limited power rating of the battery system. The third row illustrates the evolution of the battery SoC. The bottom row shows the cumulative degradation (number of equivalent cycles (N^{ref}) at 80% DoD reference condition). Higher values of the degradation cost parameter reduce the number of equivalent cycles (N^{ref}) at the expense of lower PA revenues (R^{PA}): $N^{ref} = 5.12$ *cycles* and $R^{PA} = 287\,EUR$ ($a = 15\,EUR/cycle$); $N^{ref} = 3.07$ *cycles* and $R^{PA} = 243\,EUR$ ($a = 30\,EUR/cycle$); $N^{ref} = 1.19$ *cycles* and $R^{PA} = 163\,EUR$ ($a = 60\,EUR/cycle$).

5.3.4 *Profitability assessment*

Figure 5.7 shows the profitability (left) and optimal configuration (right) of battery systems performing PA under different electricity market conditions. Whereas the *optimal* power rating (r^*_{bat}), which is defined in terms of maximizing the profitability index (PI_{bat}) of the battery system, lies in a narrow range between 0.3 and 0.5 MW/MWh, the profitability varies considerably across the considered market scenarios. Assuming current investment costs for battery systems (see table A2 in the appendix for the parameters of the cost model), the deployment of batteries would be economically viable ($PI_{bat} = 127\%$ for $W = 1$ and $PI_{bat} = 133\%$ for $W = 2$) only under the electricity prices projected for the year 2050 (*PA50* scenario). In the other case studies, the profitability index is considerably lower than 100% (red line), ranging from 10.8% (*PAd19* scenario, $W = 1$) to 46.7% (*PA30* scenario, $W = 2$). Hence, the lifetime costs exceed the lifetime revenues by a factor of 2.1 (*PA30* scenario, $W = 2$) up to a factor of 9.3 (*PAd19* scenario, $W = 1$).[4] These results suggest that today's LIBs would need further technical improvement and significant cost reduction in order to reach economic viability when used only for PA. It should be noted that current battery system costs (year 2019) are assumed throughout this thesis. As the anticipated decline in costs is not taken into account, the profitability of battery systems providing PA on future electricity markets (*PA30* and *PA50* scenarios) is generally underestimated. A literature survey of cost projections for utility-scale battery systems for the years 2020 to 2050 is provided in Ref. [151].

The model results in figure 5.7 are shown for batteries with Wöhler coefficients $W = 1$ (e.g., LIBs with LFP cathodes [66–68]) and for batteries with $W = 2$ (e.g., LIBs with NMC cathodes [47, 53, 63]). The profitability of batteries with $W = 2$ is generally somewhat higher, especially under market conditions that offer multiple PA opportunities per day (e.g., intraday markets with quarter hourly time resolution). On these electricity markets, a considerable share of the maximum possible PA revenues (i.e., revenues from batteries that have an unlimited cycle lifetime) can be generated by using battery systems mainly for shallow cycles. This causes less degradation in batteries with $W = 2$ than in batteries with $W = 1$ (see figure 5.5 and 5.6 for a comparison of dispatch schedules optimized for batteries with different Wöhler coefficients). By contrast, under current day-ahead market prices (*PAd18* and *PAd19* scenarios), the Wöhler coefficient has only a negligible impact on the economic assessment, as the cycle lifetime is generally not a limiting factor.

[4] Note that the inverse of the profitability index (PI^{-1}_{bat}) indicates by which factor the costs of battery systems must be reduced (with respect to today's costs) in order to ensure economic viability of the business case. See eq. (5.1) for the definition of the profitability index used in this thesis.

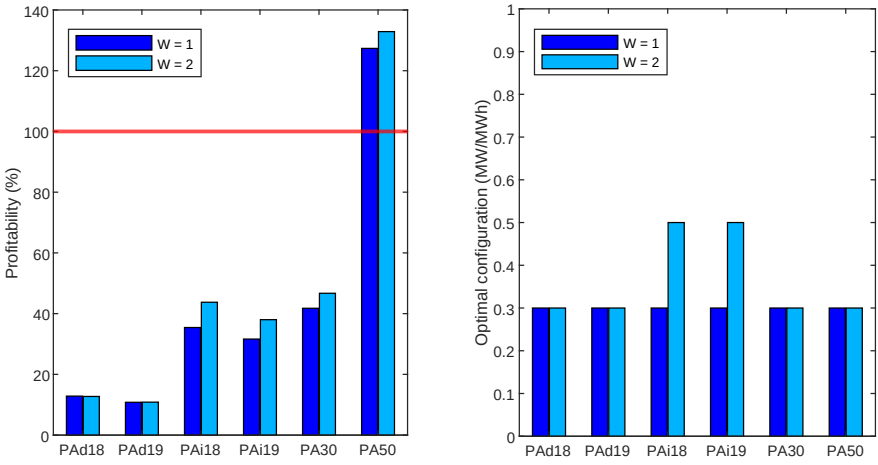

FIGURE 5.7: Profitability (left) and optimal configuration (right) of battery systems providing PA services under different electricity market conditions: Day-ahead market in Switzerland from October 2017 to September 2018 (*PAd18*), day-ahead market in Switzerland in 2019 (*PAd19*), intraday market in Germany in 2018 (*PAi18*), intraday market in Germany in 2019 (*PAi19*), 2030 scenario for Switzerland (*PA30*), and 2050 scenario for Switzerland (*PA50*). The model results were obtained for battery systems with the following parameters: Cycle lifetime (EoL_{cyc}): 6,000 cycles at 80% DoD, calendar lifetime (EoL_{cal}): 15 years, energy efficiency of new battery packs ($\eta^{bat,0}$): 95%. These parameters correspond to the *base* scenario (#0) in table 5.1. Model results for batteries with Wöhler coefficients $W = 1$ and $W = 2$ are shown in dark blue and light blue, respectively. Battery deployment is profitable if the profitability index is higher than 100%, which is indicated by the red line.

Figure 5.8 shows the profitability (left) and the lifetime revenues (right) of battery systems with varying power ratings. The profitability indices are highest for relatively low power ratings (r_{bat}) of 0.3 - 0.5 MW/MWh. This can be attributed to the fact that the lifetime revenues start to plateau at relatively low power ratings, hence the additional PA revenues do not justify the significantly higher investment and O&M costs associated with the larger power units.

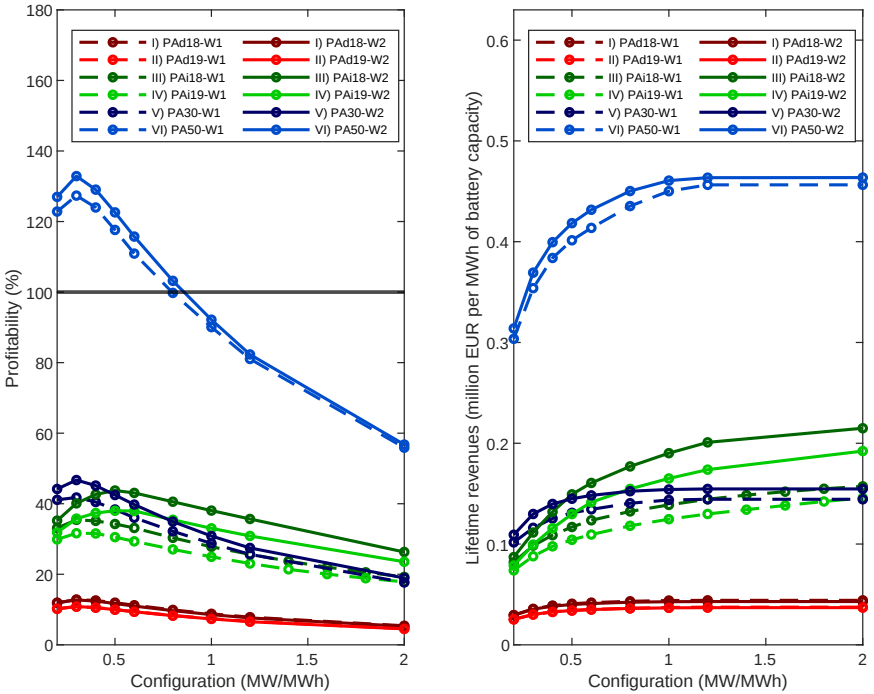

FIGURE 5.8: Profitability (left) and lifetime revenues (right) of battery systems with varying power ratings providing PA services under different electricity market conditions: Day-ahead market in Switzerland from October 2017 to September 2018 (*PAd18*), day-ahead market in Switzerland in 2019 (*PAd19*), intraday market in Germany in 2018 (*PAi18*), intraday market in Germany in 2019 (*PAi19*), 2030 scenario for Switzerland (*PA30*), and 2050 scenario for Switzerland (*PA50*). The model results were obtained for battery systems with the following parameters: Cycle lifetime (EoL_{cyc}): 6,000 cycles at 80% DoD, calendar lifetime (EoL_{cal}): 15 years, energy efficiency of new battery packs ($\eta^{bat,0}$): 95%. These parameters correspond to the *base* scenario (#0) in table 5.1. Model results for batteries with Wöhler coefficients $W = 1$ and $W = 2$ are shown as dashed and solid lines, respectively. Battery deployment is profitable if the profitability index is higher than 100%, which is indicated by the grey line.

5.3.5 *Evaluation of battery research targets*

Figure 5.9 compares the profitability of battery systems providing PA services under different development scenarios for today's LIBs (see table 5.1). The shown ranges indicate how much the profitability of battery systems could be increased by improving their performance parameters from the current *base* values (bullets (•) and (•) for $W = 1$ and $W = 2$, respectively) to the enhanced values of the 15 development scenarios detailed in table 5.1 (upper end of the vertical solid lines). Only the model results obtained for the most profitable battery system configurations are shown.

Figure 5.9 shows that the economic benefits of improving different performance parameters are strongly dependent on the electricity market scenario considered: In the *Day-ahead 2019* scenario, the energy efficiency of the battery system (η) is the most influential parameter. Due to the comparatively small difference between peak and valley prices in this scenario, PA revenues are strongly affected by the battery charge and discharge losses, explaining the high impact of the energy efficiency (η) on PA revenues.[5] By contrast, the cycle lifetime (Cy) and the second life (SL) usability rank as the most important parameters in all other market scenarios. Longer cycle lifetimes (Cy) would be particularly desirable under market conditions that offer multiple revenue opportunities per day (e.g., intraday market with quarter hourly time resolution), as it allows for higher PA revenues by charging and discharging the battery system several times per day. These findings underline that there is no *one-target-fits-all* strategy for the further development of today's LIBs. It is therefore vital to take into consideration the specifics of the application case and electricity market conditions when creating (and communicating) guidelines for battery research. However, as general rules of thumb, the following conclusions can be drawn: (i) improving the second life usability of batteries would generally be highly beneficial, as it extends the number of years the storage system is operational, and (ii) the higher the volatility of the electricity prices and thus the number of PA opportunities, the higher the economic benefits of long cycle lifetimes.

Furthermore, figure 5.9 shows that the economic benefits of improving two or multiple performance parameters at the same time are typically not additive. For instance, in the *Day-ahead 2019* scenario, improving only the cycle lifetime (Cy) of today's battery systems would have an almost negligible impact on their profitability, whereas longer cycle lifetimes become an important lever to further increase PA revenues once the calendar lifetime (Ca) or the energy efficiency (η) has been improved. Similarly, in the other market scenarios, improving the calendar lifetime (Ca) would currently only have a minor impact on the profitability, which, however, will change as soon as the

[5] Conversely, if the difference between peak and valley prices is high, performing PA may still be economically attractive even if the energy losses are significant.

cycle lifetime has been improved.

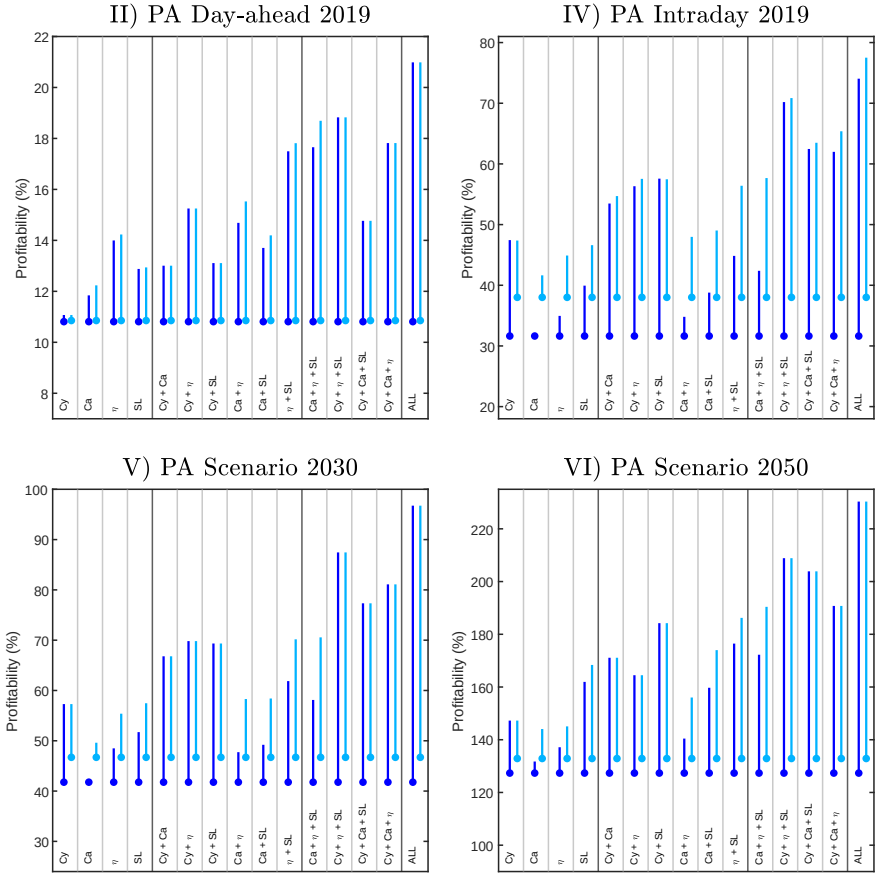

FIGURE 5.9: Profitability of battery systems providing PA services under different development scenarios for today's LIBs (see table 5.1). The shown ranges (vertical solid lines) indicate how much the profitability of battery systems could be increased in each development scenario, whereas the bullets ((●) and (●) for $W = 1$ and $W = 2$, respectively) refer to the *base* scenario (i.e., performance of LIBs today). Used symbols and abbreviations: Cycle lifetime (Cy), calendar lifetime (Ca), energy efficiency of the battery system (η), and second life (SL) usability. Only the model results obtained for battery systems with optimized power ratings (r^*_{bat}) are shown. The battery system costs were computed based on the costs of battery packs and power units in the year 2019, and a discount rate (r_d) of 4% was assumed (see chapter 5.1 for the details of the battery system cost model and table A2 for the model parameters.) The profitability indices are shown on different scales, as they vary significantly across the considered electricity market scenarios.

5.4 CASE STUDIES FOR COMBINED PEAK SHAVING AND PRICE ARBITRAGE

This chapter discusses the economics of using rechargeable batteries for combined PS and PA, where revenues are generated both by lowering peak load charges and by exploiting temporal price differences on the day-ahead electricity market.

5.4.1 *Model input data*

The deployment of stationary batteries is considered for two different electricity substations of a Swiss distribution system operator. Figure 5.10 shows the load profile of the two electricity substations and the day-ahead electricity market prices in Switzerland for the period of October 2017 to September 2018.

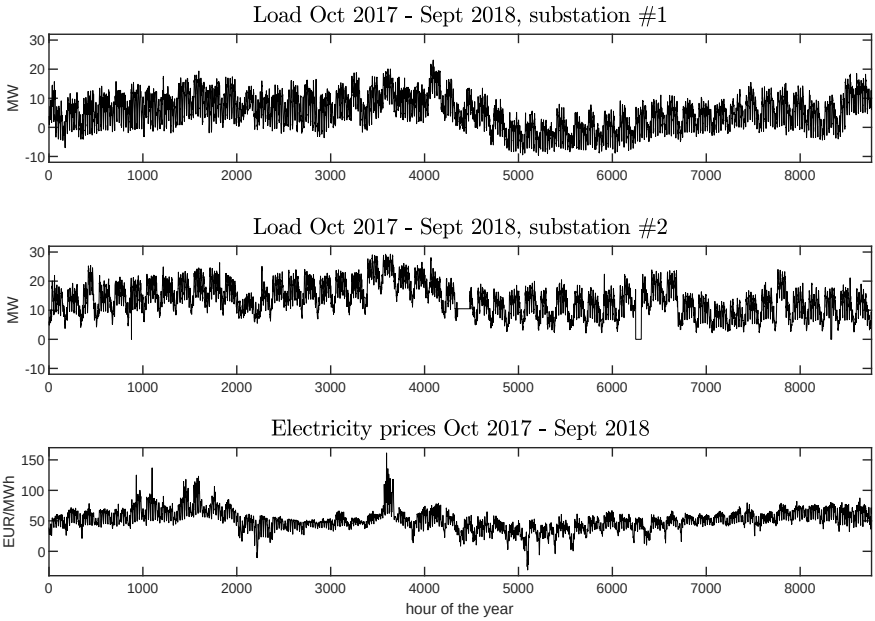

FIGURE 5.10: Load profile of the two electricity substations (top and middle) and day-ahead electricity market prices in Switzerland for the period of October 2017 to September 2018 (bottom).

The following model assumptions are made:

- The distribution system operator is assumed to be a price taker, hence the electricity prices are provided as an external model input. In addition to the energy-specific costs, the distribution system operator must pay charges for the peak load in each month ($p_{peak}^{month} = 4{,}950\ CHF/MW$). It is assumed that the peak load charges are the same in all years of battery operation.
- Perfect foresight of the load profile and the electricity prices is assumed to ensure that the distribution system operator can realize the maximum possible PS and PA revenues. In practice, the revenues might be somewhat lower due to forecast errors and thus suboptimal battery dispatch schedules. However, the negative impact of forecast errors on PS and PA revenues could be mitigated by adapting (i.e., recomputing) the dispatch schedules as more recent forecasts become available.
- The same load profiles and electricity prices are used to assess PS and PA revenues in all years of battery operation.
- The operation of battery systems is optimized for non-overlapping dispatch periods (i.e., optimization horizons) of 1 day. The battery SoC at the beginning (SoC^{init}) and end (SoC^{end}) of each day is set to 50%.
- For each year, the operation of battery systems is modeled for 10 *typical* days. The *typical* load profiles and price curves were obtained by applying the clustering algorithm described in chapter 4.3.2.

5.4.2 *Clustering of load profiles and price curves*

Figure 5.11 provides an example illustrating the clustering of load and price time series, showing *typical* load profiles and price curves for substation #1 (see figure 5.10). The data was obtained by applying the clustering algorithm described in chapter 4.3.2.

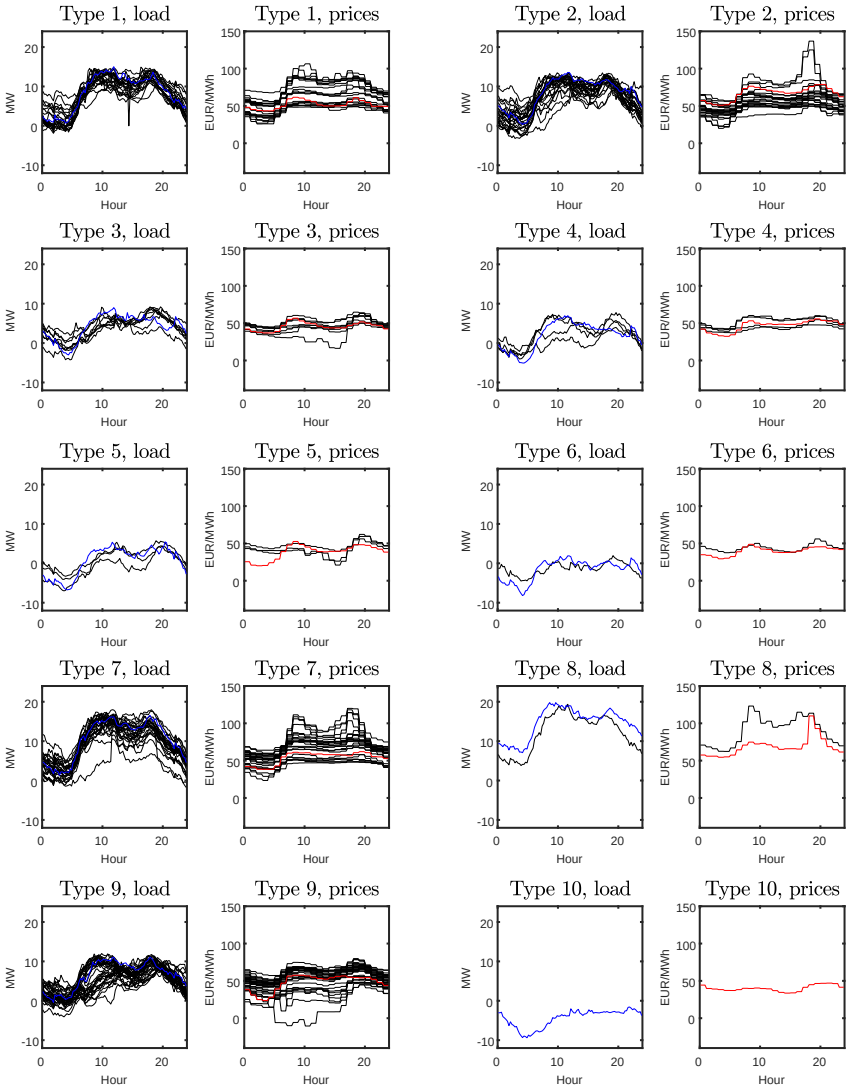

FIGURE 5.11: Clustering of daily load profiles and electricity prices for substation #1 (see figure 5.10) using the clustering algorithm described in chapter 4.3.2. For each *typical* day, the representative load profile and price curve are shown in blue and red, respectively. All other time series assigned to the same *typical* day are shown in black.

5.4.3 *Battery system operation*

Figure 5.12 and 5.13 show optimal dispatch schedules for battery systems providing combined PS and PA services. A battery system with $C_{bat} = 1\,MWh$ and $r_{bat} = 1.5\,MW/MWh$ is considered.[6] The charge and discharge power is illustrated for dispatch periods of *type 7* (figure 5.12) and *type 9* (figure 5.13) with an optimization horizon of 24 hours and a time step length of 15 minutes (see figure 5.11 for an illustration of the *typical* dispatch periods). These dispatch periods are shown to illustrate the charge and discharge power for two example days with (*type 7*) and without (*type 9*) PS. Note, however, that all 10 typical dispatch periods of the whole year (see figure 5.11) were considered for the economic assessment of battery systems. All model results were obtained for batteries with Wöhler coefficients $W = 2$, such as LIBs with NMC cathodes [47, 53, 63] (see chapter 2.3.3.1). Figure 5.12a and 5.13a show optimal dispatch schedules for degradation cost penalties $a = 0\,EUR/cycle$ (i.e., battery usage is not penalized), whereas figure 5.12b and 5.13b show optimal dispatch schedules for $a = 20\,EUR/cycle$.[7] As expected, imposing a penalty on battery degradation reduces the number of cycles at the expense of lower revenues. This is especially the case during dispatch periods of *type 9* (figure 5.13), where the battery system provides only the PA (but no PS) service due to the low load of the electricity substation during these days.

During dispatch periods of *type 7* (figure 5.12), the battery system is used both for PA and PS. In order to reduce the two load peaks at noon and in the early evening hours, the battery system is discharged at ca. 12 pm and at ca. 6 pm, respectively. This allows the distribution system operator to reduce the daily peak load of the electricity substation (and hence the peak load in the month of October) from $16.54\,MW$ to $15.30\,MW$.

A closer look at figure 5.12 shows that there exist trade-offs between the PS and PA operation objectives: In order to reduce the evening peak load, the battery system must be recharged between ca. 4 pm and 5 pm when the electricity price is high. Hence, the monthly peak load is reduced at the expense of lower PA revenues.

[6] While a relatively *large* battery (i.e., $C_{bat} = 1\,MWh$) is considered here to better illustrate its PS capabilities, the deployment of *smaller* batteries (e.g., $C_{bat} = 0.25\,MWh$) would be more profitable, as smaller batteries generally offer a better ratio between PS revenues and battery investment costs (see chapter 5.4.4).

[7] Note that these degradation cost penalties differ somewhat from the ones used in figure 5.5 and 5.6, where PA on the intraday electricity market is illustrated for penalties of up to $60\,EUR/cycle$. In the combined PS and PA case, battery systems would perform an unrealistically low number of cycles under such high penalties due to the lower price volatility of the day-ahead market. Therefore, figure 5.12 and 5.13 show only model results for penalties of up to $20\,EUR/cycle$. Imposing higher penalties on battery degradation would further reduce the number of cycles at the expense of lower PS and PA revenues.

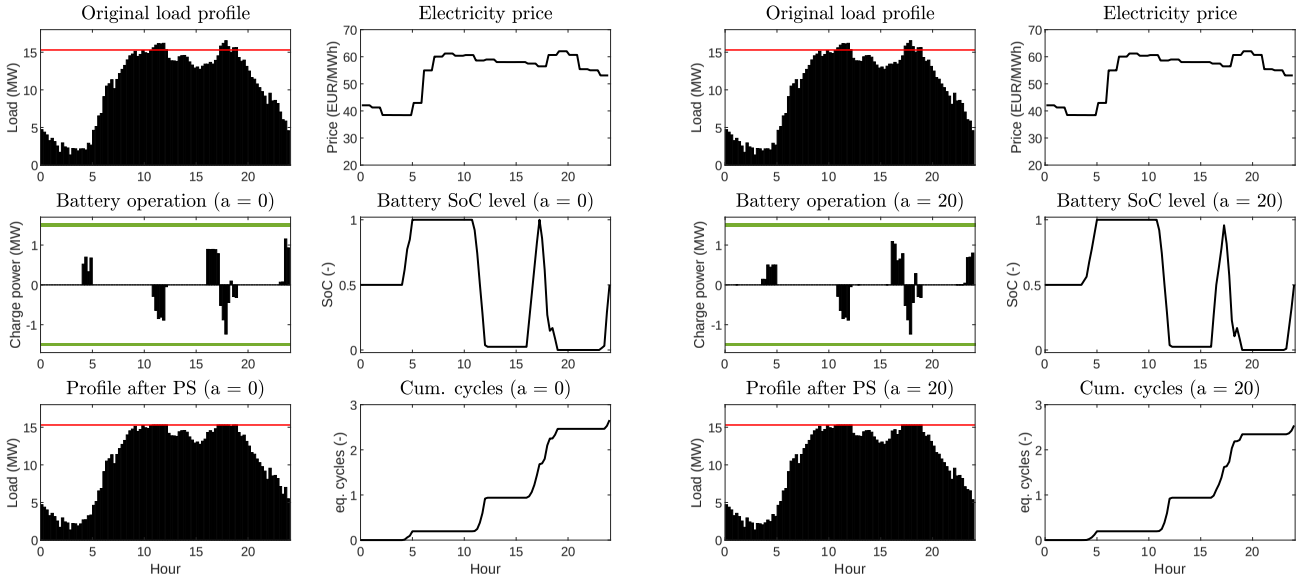

FIGURE 5.12: Optimal dispatch schedules for a *typical* day in October 2017 (electricity substation #1, day of *type 7*). (a) Dispatch if battery usage is not penalized. (b) Dispatch if a penalty of $20\,EUR/cycle$ is imposed, which reduces the degradation of the battery at the expense of lower PA revenues. The dispatch schedules illustrate that PS and PA are conflicting objectives: In order to reduce the evening peak load at ca. 6 pm, the battery must be recharged between ca. 4 pm and 5 pm when the electricity price is high. This allows the distribution system operator to reduce the highest load in October from $16.54\,MW$ to $15.30\,MW$ (red line). Note that the optimal dispatch schedule would be significantly different if no PS was performed: In this case, the battery would be discharged only once, i.e., when the electricity price is highest. In other words, in the shown example, the monthly peak load is reduced at the expense of lower PA revenues. The model results were obtained for battery systems with the following parameters: energy capacity (C_{bat}): $1\,MWh$, power rating (r_{bat}): $1.5\,MW/MWh$, battery state of health (SoH_{bat}): 100%, energy efficiency of the battery system (η^{tot}): 90%, Wöhler coefficient (W): 2, state of charge at the beginning (SoC^{init}) and end (SoC^{end}) of the dispatch period: 50%. The green lines indicate the limits on the battery charge and discharge power.

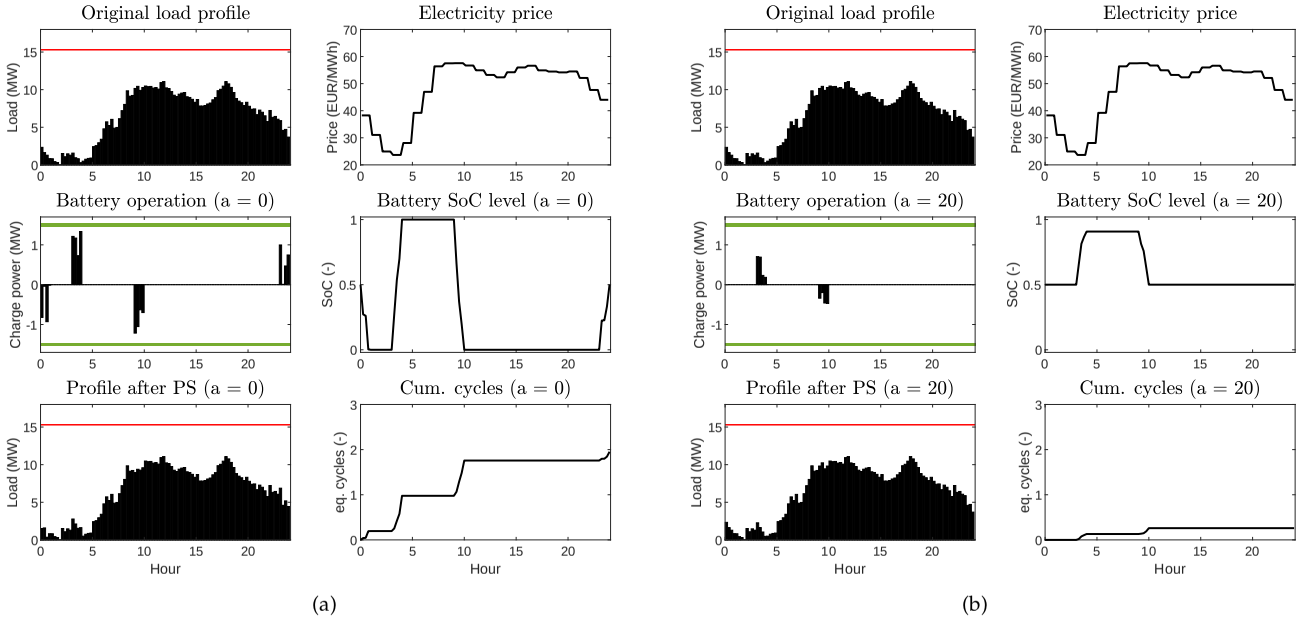

FIGURE 5.13: Optimal dispatch schedules for a *typical* day in October 2017 (electricity substation #1, day of *type 9*). (a) Dispatch if battery usage is not penalized. (b) Dispatch if a penalty of $20 EUR/cycle$ is imposed, which reduces the degradation of the battery at the expense of lower PA revenues. The model results were obtained for battery systems with the following parameters: energy capacity (C_{bat}): $1 MWh$, power rating (r_{bat}): $1.5 MW/MWh$, battery state of health (SoH_{bat}): 100%, energy efficiency of the battery system (η^{tot}): 90%, Wöhler coefficient (W): 2, state of charge at the beginning (SoC^{init}) and end (SoC^{end}) of the dispatch period: 50%. The green lines indicate the limits on the battery charge and discharge power.

Figure 5.14 shows monthly peak loads after PS for the first (dark green) and last (light green) year of the PSPA project. Minor differences are due to the decreasing performance of the battery system over time, i.e., lower remaining energy capacity and lower energy efficiency. For comparison, monthly peak loads before PS (i.e., without battery) are shown in blue.

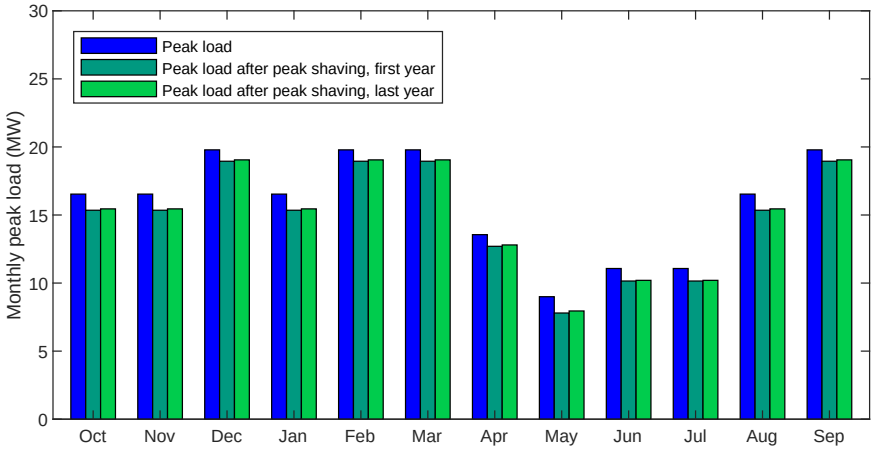

FIGURE 5.14: Monthly peak loads after performing PS for the first (dark green) and last (light green) year of the PSPA project (electricity substation #1). For comparison, monthly peak loads before performing PS (i.e., without battery) are shown in blue. The model results were obtained for battery systems with the following parameters: energy capacity (C_{bat}): $1\,MWh$, power rating (r_{bat}): $1.5\,MW/MWh$, battery state of health (SoH_{bat}): 94.8% (first year) and 80.0% (last $\widehat{=}$ 15^{th} year), energy efficiency of the battery system (η^{tot}): 90.8% (first year) and 86.7% (last $\widehat{=}$ 15^{th} year), Wöhler coefficient (W): 2, maximum number of cycles per year (N^{ref}_{max}): 400, state of charge at the beginning (SoC^{init}) and end (SoC^{end}) of the dispatch periods: 50%.

Figure 5.15 compares revenue streams from PS (left) and PA (middle) generated in the first year of the PSPA project. Interestingly, 94.1% of the total revenues of $57{,}261\,EUR$ are due to PS, while the PA business contributes only 5.9%. In order to quantify trade-offs existing between the PS and PA operation objectives, figure 5.15 (right) additionally shows revenues for the hypothetical scenario that the distribution system operator incurs no power-specific electricity costs, i.e., $p^{month}_{peak} = 0$. (Regardless of battery dispatch, PS revenues are equal to zero in this scenario.) In the presence and absence of power-specific electricity costs, PA revenues amount to $3{,}369\,EUR$ and $3{,}849\,EUR$, respectively. Hence, performing PS in addition to PA reduces PA revenues by 12.5%, which, however, is more than compensated by the high PS revenues. This comparison shows that the economic trade-offs existing between the PS and PA operation objectives are relatively minor for the considered case study.

It is important to note that the economic assessment of battery systems providing PS and PA services is dependent on both the electricity costs and the load profile of the distribution system operator: PS revenue opportunities are determined by the power-specific electricity costs and specific features in the load profile, such as the *shape* (i.e., *height* to *area* ratio) of the load peaks. By contrast, PA revenue opportunities are dependent mainly on the volatility of the (energy-specific) electricity prices.

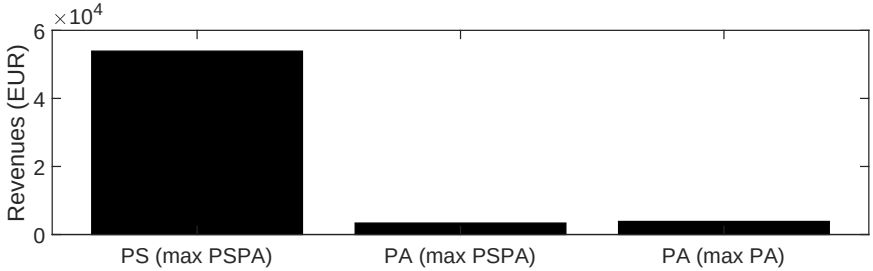

FIGURE 5.15: Revenue streams (electricity substation #1). Left and middle: revenue streams from PS and PA in the presence of power-specific electricity costs. Right: PA revenues in the absence of power-specific electricity costs. The revenues are specified for the first year of the PSPA project without consideration of O&M costs. The model results were obtained for battery systems with the following parameters: energy capacity (C_{bat}): $1\,MWh$, power rating (r_{bat}): $1.5\,MW/MWh$, battery state of health (SoH_{bat}): 94.8%, energy efficiency of the battery system (η^{tot}): 90.8%, Wöhler coefficient (W): 2, maximum number of cycles per year (N^{ref}_{max}): 400, state of charge at the beginning (SoC^{init}) and end (SoC^{end}) of the dispatch periods: 50%.

Figure 5.16 shows the lifetime revenues of battery systems with varying energy capacities (C_{bat}) and power ratings (r_{bat}). Model results for electricity substation #1 are shown in figure 5.16a, and the results for substation #2 are shown in figure 5.16b. The lifetime revenues are almost identical for batteries with Wöhler coefficients $W = 1$ (e.g., LIBs with LFP cathodes [66–68]) and $W = 2$ (e.g., LIBs with NMC cathodes [47, 53, 63]), as the cycle lifetime is generally not a limiting factor in the shown examples.

As expected, the lifetime revenues depend both on the *size* (i.e., energy capacity) and maximum charge/discharge *rate* (i.e., power rating[8]) of the battery system. Whereas *small* batteries ($C_{bat} = 0.25\,MWh$, shown in dark blue/green) require *high* power ratings ($r_{bat} > 2\,MW/MWh$) to exploit their full PS potential, *large* batteries ($C_{bat} = 3\,MWh$, shown in light blue/green) do not benefit from power ratings higher than ca. $0.8\,MW/MWh$. This illustrates that the maximum charge/discharge rate is a critical factor mainly for *small* batteries that perform PS during short periods of time (typically, ≤ 30 minutes). By contrast, for *large* batteries, which perform PS for

[8]Note that the power rating (r_{bat}) determines the minimum time required for battery (dis)charging. For instance, a battery system with a power rating of $r_{bat} = 2MW/MWh$ requires at least 30 minutes to fully (dis)charge.

extended periods of time[9] (typically, ≥ 1 hour), the energy capacity is usually the performance limiting factor. Hence, the power rating is less critical.

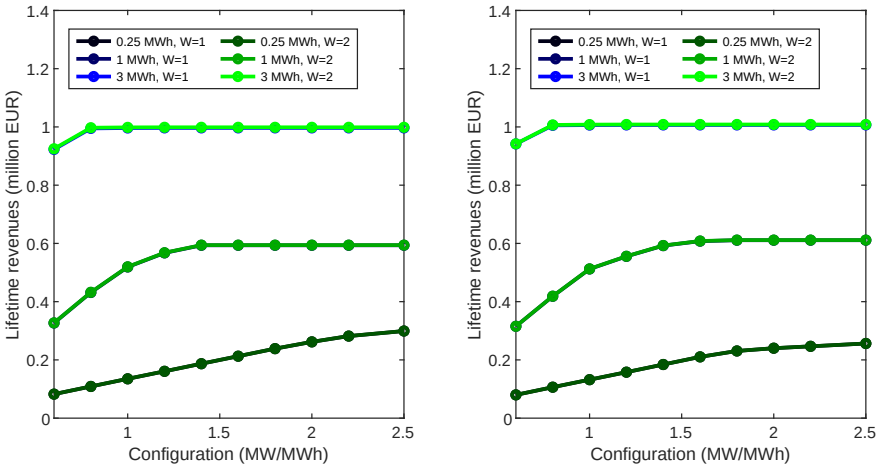

(a) Electricity substation #1

(b) Electricity substation #2

FIGURE 5.16: Lifetime revenues of battery systems with varying energy capacities (C_{bat}) and power ratings (r_{bat}) providing combined PS and PA at two different electricity substations. The model results were obtained for battery systems with the following parameters: Cycle lifetime (EoL_{cyc}): 6,000 cycles at 80% DoD, calendar lifetime (EoL_{cal}): 15 years, energy efficiency of new battery packs ($\eta^{bat,0}$): 95%. These parameters correspond to the base scenario (#0) in table 5.1. The model results obtained for batteries with Wöhler coefficients $W = 1$ (blue) and $W = 2$ (green) are almost identical.

5.4.4 *Profitability assessment*

The energy capacity (C_{bat}) has a significant impact on battery profitability: the *smaller* the battery, the higher its profitability (see figure 5.17). This can be ascribed to the fact that, starting from a *small* battery system, significantly higher energy capacities (C_{bat}) are generally required to further reduce peak loads, as the battery system not only has to provide higher discharge power but also has to do so for expended periods of time. Hence, the achievable reduction in peak load $[MW]$ (and thus the achievable PS revenues) does not scale linearly with the energy capacity. As a result, the marginal PS revenues with respect to battery size (i.e., $\partial R^{PS}/\partial C_{bat}$) usually decrease as C_{bat} increases. By contrast, the costs of battery systems are assumed to be proportional to

[9] The more the peak capacity is reduced, the longer the battery system must provide the PS service. This can be ascribed to the non-rectangular shape of the peaks in typical electricity load profiles (i.e., the load peaks are broader at the bottom than at the top).

their energy capacity (see eq. 5.6).[10] Therefore, *small* batteries offer the highest revenue to cost ratio and are thus considered the preferred choice for PS applications.

Figure 5.17 shows that *small* battery systems (e.g., $C_{bat} = 0.25\,MWh$) with relatively high power ratings of $1.8\,MW/MWh$ to $2.0\,MW/MWh$ are most profitable for the combined provision of PS and PA services. In the considered case studies, revenues are mainly generated by performing PS, whereas PA contributes only relatively little to the total revenues (see figure 5.15). The optimal configuration therefore depends on the technical requirements enabling PS, explaining why higher power ratings are required than when batteries are used solely for PA ($r^*_{bat} = 0.3\,MW/MWh$ for battery systems performing PA on the day-ahead market, see figure 5.7).

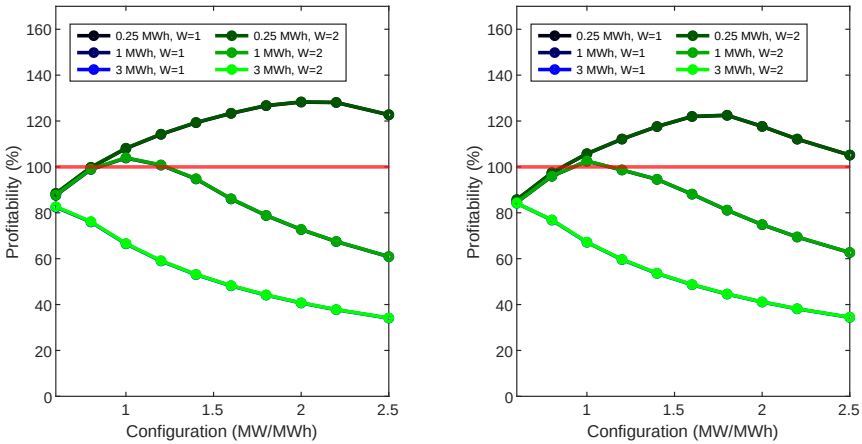

(a) Electricity substation #1 (b) Electricity substation #2

FIGURE 5.17: Profitability of battery systems with varying energy capacities (C_{bat}) and power ratings (r_{bat}) providing combined PS and PA at two different electricity substations. The model results were obtained for battery systems with the following parameters: Cycle lifetime (EoL_{cyc}): 6,000 cycles at 80% DoD, calendar lifetime (EoL_{cal}): 15 years, energy efficiency of new battery packs ($\eta^{bat,0}$): 95%. These parameters correspond to the base scenario (#0) in table 5.1. The model results obtained for batteries with Wöhler coefficients $W = 1$ (blue) and $W = 2$ (green) are almost identical. Battery deployment is profitable if the profitability index is higher than 100%, which is indicated by the red line.

It should be noted that the economic assessment is affected by the energy capacity (C_{bat}) only if the battery system provides PS services (or any service combined with

[10] This assumption may no longer be valid for battery systems with energy capacities significantly smaller than $1\,MWh$, as the developed battery system cost model (see chapter 5.1) was parameterized for large-scale batteries designed for industrial applications (smaller batteries would be more expensive per unit of energy capacity). For this reason, energy capacities $C_{bat} \geq 0.25\,MWh$ are considered for the economic assessment of different battery configurations.

PS). By contrast, the profitability of battery systems providing exclusively PA or PCR depends solely on their power rating (r_{bat}), as the revenues and investment costs are in this case both proportional to the energy capacity.[11]

5.4.5 *Evaluation of battery research targets*

Figure 5.18 compares the profitability of battery systems providing combined PS and PA services at electricity substation #1 under different development scenarios for today's LIBs (see table 5.1). The shown ranges indicate how much the profitability of battery systems could be increased by improving their performance parameters from the current *base* values (bullets (•) and (•) for $W = 1$ and $W = 2$, respectively) to the enhanced values of the 15 development scenarios detailed in table 5.1 (upper end of the vertical solid lines). Only the model results obtained for the most profitable battery system configurations are shown, i.e., $C_{bat} = 0.25\,MWh$ and optimized power ratings. Note that the *optimal* power rating (r^*_{bat}) may differ across the different battery development scenarios.

The second life (SL) usability and the calendar lifetime (Ca) rank as the most important targets for battery research. Both of these parameters extend the number of years battery systems remain operational and hence increase their lifetime revenues. By contrast, improving the energy efficiency (η) and the cycle lifetime (Cy) would only have a minor impact on the profitability of the considered business case. This can be ascribed to the fact that the energy efficiency (η) and the cycle lifetime (Cy) affect mainly the PA revenues, which contribute relatively little to the total revenues. Note, however, that higher energy efficiencies would be beneficial from an environmental point of view.

It should be emphasized that the results presented in this chapter are case study specific, as the provision of PS has been analyzed for two particular electricity substations. The developed modeling framework could be used to assess the viability of PS under additional load profiles and electricity prices, which would allow for more generally valid conclusions.

[11] Strictly speaking, this is only the case if no minimum bid increments apply to both trading on the electricity market and the provision of PCR services. In this thesis work, these practical aspects (see Refs. [145, 146]) are not considered, as it is assumed that battery operators have the option to pool multiple independent battery systems into one bigger storage unit.

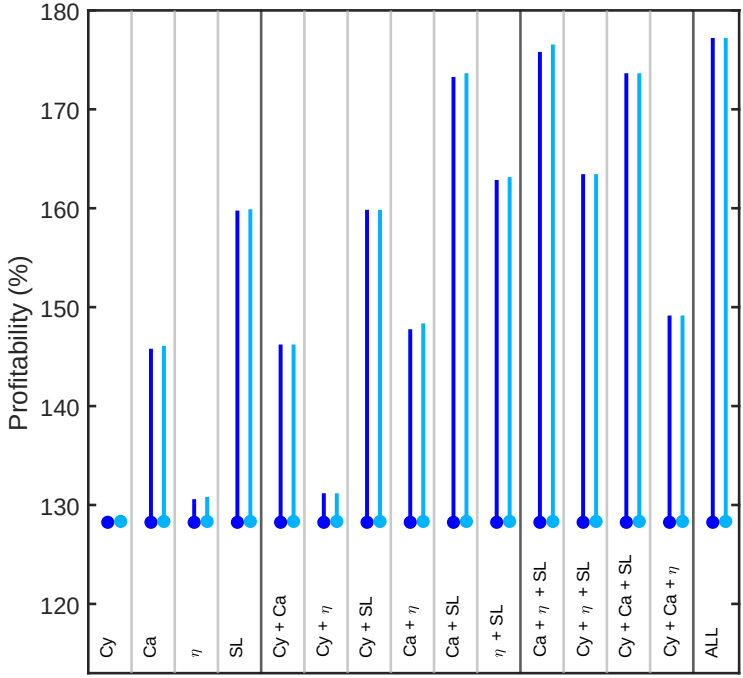

FIGURE 5.18: Profitability of battery systems providing combined PS and PA services at electricity substation #1 under different development scenarios for today's LIBs (see table 5.1). The shown ranges (vertical solid lines) indicate how much the profitability of battery systems could be increased in each development scenario, whereas the bullets ((•) and (•) for $W = 1$ and $W = 2$, respectively) refer to the *base* scenario (i.e., performance of LIBs today). Used symbols and abbreviations: Cycle lifetime (Cy), calendar lifetime (Ca), energy efficiency of the battery system (η), and second life (SL) usability. Only the model results obtained for battery systems with an energy capacity (C_{bat}) of $0.25\,MWh$ and optimized power ratings (r^*_{bat}) are shown. The battery system costs were computed based on the costs of battery packs and power units in the year 2019, and a discount rate (r_d) of 4% was assumed (see chapter 5.1 for the details of the battery system cost model and table A2 for the model parameters).

5.5 CASE STUDIES FOR PRIMARY CONTROL RESERVES

This chapter discusses the economics of using rechargeable batteries for PCR, where revenues are generated by providing regulation power to the electricity grid.

5.5.1 *Model input data*

The provision of PCR services is analyzed under varying electricity market conditions. It is assumed that the battery operator has access to the intraday electricity market and that the battery SoC level is managed using a moving average based control scheme (see chapter 4.4 for the details).

Table 5.3 details the electricity market scenarios considered as case studies. In the case studies I - II, the provision of PCR is modeled under current electricity market conditions, considering the regulatory framework defined by Swissgrid [138]. Case studies III - IV are representative of electricity market scenarios with less stringent PCR prequalification criteria that do not require battery operators to keep additional energy reserves (i.e., batteries are required to be operational only during periods with *normal* evolution of the grid frequency as defined by the *prequalification time series* of the grid frequency ($\mathbf{f}^p$)). To analyze the impact of alternative intraday electricity market designs with shorter delivery periods on the provision of PCR services, case study IV assumes that electricity contracts can be traded every 5 minutes. It should be noted that the case studies III - IV are based on hypothetical electricity market conditions. These case studies are inspired by Ref. [139], which suggests that less stringent PCR prequalification criteria would allow stationary batteries to better exploit their technical potential without significantly compromising their ability to provide the PCR service. Case study IV is motivated by the design of intraday electricity markets in countries other than Switzerland. The implementation of $5\,min$ settlement periods is planned for the Australian electricity market, for instance [152].

The provision of PCR is modeled for the years 2017 and 2019. In addition to the parameters listed in table 5.3, the following input data is used:

- Prequalification time series of the grid frequency ($\mathbf{f}^p$). According to the regulatory framework defined by Swissgrid, $\mathbf{f}^p$ corresponds to the following time series: $49.80\,Hz$ for $5\,min$, $49.90\,Hz$ for $10\,min$, and $49.95\,Hz$ for an indefinite time duration. [138, 139]
- Historical (measured) time series of the frequency of the Swiss electricity grid ($\mathbf{f}$) for two months (June and October) in 2017 and for two months (June and November) in 2019. The data is considered representative for the years 2017 and 2019, respectively.

- Historical time series of the electricity price in 2017 and 2019 obtained from *EPEX spot*. As the data was not available for Switzerland, the provision of PCR in Switzerland is assessed using prices from the German intraday electricity market. Note that the electricity price determines the costs of battery SoC restoration. As these costs contribute only a few percent to the annual cash flows, using data for Germany instead of Switzerland should have a minor impact on the model results.

- Average remuneration for the provision of PCR ($\overline{\pi}^{PCR}$) in Switzerland, taken to be the average remuneration for *accepted* PCR bids. $\overline{\pi}^{PCR} = 122{,}052\ EUR/(MW \cdot yr)$ for the year 2017 and $\overline{\pi}^{PCR} = 77{,}710\ EUR/(MW \cdot yr)$ for the period from January to June 2019 [153]. Note that as of July 2019, *pay-as-bid* PCR capacity auctions were replaced by *pay-as-cleared* auctions. Albeit these changes had a minor impact on the remuneration payments for PCR capacity in the second half year 2019, only the period from January to June 2019 is considered to improve the comparability of model results obtained for the years 2017 and 2019. [145, 153]

TABLE 5.3: Electricity market scenarios considered as case studies. τ_{WP} denotes the duration of electricity contracts, τ_{MA} is the duration of the averaging period, τ_{LT} denotes the lead time between power exchange scheduling and physical delivery, and τ^{Res} is the additional energy capacity that must be kept for PCR provision. Access to electricity markets with different lead times and contract durations is modeled using different sets of SoC control scheme parameters (τ_{WP}, τ_{MA}, and τ_{LT}).

#	Description of electricity market scenario	τ_{WP} [s]	τ_{MA} [s]	τ_{LT} [s]	τ^{Res} [s]
I	PCR today 1 (*PCR-T1*): Provision of PCR under the current regulatory framework defined by Swissgrid [138]. The following electricity market conditions are considered, which are representative of the intraday market in Switzerland: lead time between power exchange scheduling and physical delivery (τ_{LT}): 30 *min*; contract duration (τ_{WP}): 15 *min* [146].	900	900	1,800	900
II	PCR today 2 (*PCR-T2*): Identical to the *PCR-T1* scenario, except that the lead time $\tau_{LT} = 5\,min$, which is the case in some European intraday markets [146].	900	900	300	900
III	PCR alternative 1 (*PCR-A1*): Provision of PCR under a less stringent regulatory framework which does not require battery operators to keep additional energy reserves. Like in the *PCR-T2* scenario, the lead time $\tau_{LT} = 5\,min$.	900	900	300	0
IV	PCR alternative 2 (*PCR-A2*): Identical to the *PCR-A1* scenario, except that electricity contracts can be traded every 5 minutes.	300	300	300	0

5.5.2 *Battery system operation*

Figure 5.19 and 5.20 show simulation results illustrating the operation of battery systems under prequalification grid frequencies ($\mathbf{f}^p$) and under measured frequencies ($\mathbf{f}$), respectively. The left-hand side of the figures shows the evolution of different power flows: P^{WP} (green) is the working point, P^{Loss} (red) denotes the internal energy losses in the battery system, P^{PCR} (blue) corresponds to the control signal, and P^{Ext} (black) denotes the total power exchanged between the battery system and the electricity grid. A positive sign for P^{Ext} indicates battery charging, whereas a negative sign indicates battery discharging. All power flows have units $[MW/MW]$, as they are normalized by the amount of PCR capacity provided by the battery system. The right-hand side of figure 5.19 and 5.20 shows the evolution of the battery SoC.

Figure 5.19 (left) shows in blue the control signal (P^{PCR}). It is identical for all case studies, as the same prequalification time series of the grid frequency ($\mathbf{f}^p$) is assumed to model the provision of PCR under the different electricity market scenarios (see chapter 5.5.1). The working point (P^{WP}) is shown in green. Initially, $P^{WP} = 0$, since no power is supplied from the intraday market as the battery starts providing the PCR service.[12] Hence, the power exchanged between the battery and the electricity grid (P^{Ext}) (shown in black) corresponds to the control signal (i.e., $P^{Ext} = P^{PCR}$). As the battery system is discharged ($P^{Ext} < 0$), its SoC level drops close to the minimum of the allowed range (green lines). At $t = \tau_{WP} + \tau_{LT} + 1\ [s]$, physical delivery of the first electricity contract[13] starts (hence, $P^{WP} > 0$), and the battery system is recharged.

A comparison of battery systems operated under the different electricity market scenarios reveals that the parameters τ_{WP}, τ_{MA}, τ_{LT}, and τ^{Res} have a significant impact on the PCR capacity that can be provided: $C^{PCR} = 0.83\,MW$ (*PCR-T1*), $C^{PCR} = 1.02\,MW$ (*PCR-T2*), $C^{PCR} = 2.40\,MW$ (*PCR-A1*), and $C^{PCR} = 3.46\,MW$ (*PCR-A2*).[14] As the operator of the battery system is remunerated by the TSO for the provided PCR capacity, higher capacities translate into higher revenues. It should be noted, however, that the PCR capacity that can be provided in practice may be lower because of the limited battery cycle lifetime, and, depending on the configuration of the battery system, due to constraints on the maximum charge and discharge power (see figure 5.21 and

[12] $P^{WP} = 0$ for the first 2,700 (*PCR-T1*), 1,200 (*PCR-T2* and *PCR-A1*), or 600 (*PCR-A2*) seconds.

[13] The first electricity contract is closed at $t = \tau_{WP}\ [s]$. New contracts are closed every $\tau_{WP}\ [s]$ in order to adjust the working point of the battery system. A discussion of the moving average based SoC control scheme is provided in chapter 4.4.

[14] The model results were obtained for battery systems with the following parameters: energy capacity (C_{bat}): $1\,MWh$, power rating (r_{bat}): $5\,MW/MWh$, battery state of health (SoH_{bat}): 100%, energy efficiency of the battery system (η^{tot}): 90%, initial battery state of charge (SoC^{init}): 50%. It is assumed that the battery cycle lifetime is not a limiting factor. Hence, the specified PCR capacities refer to the theoretical ones (C^{PCR}_{theor}). Depending on the battery cycle lifetime and its degradation behavior with respect to cycle depth, the offered PCR capacities ($C^{PCR}_{offered}$) could be lower than the theoretical ones.

5.22 for the details). Nevertheless, the results suggest that the regulatory conditions defined by the TSO and the design of the intraday electricity market are important factors affecting the business case of providing PCR services.

Figure 5.20 illustrates the operation of battery systems under measured grid frequencies. The control signal (P^{PCR}) (shown in blue) is approximately balanced (i.e., zero mean), and its amplitude is significantly smaller than is the case under prequalification grid frequencies (see figure 5.19). As a result, the battery system performs mostly shallow cycles in a SoC range close to 50%. The differences in the SoC profiles shown in figure 5.19 and 5.20 can be attributed to the fact that the prequalification time series of the grid frequency ($\mathbf{f}^p$), which is used in the prequalification process of energy storage units, occurs very rarely in practice (see also Ref. [139] for a discussion of this matter).

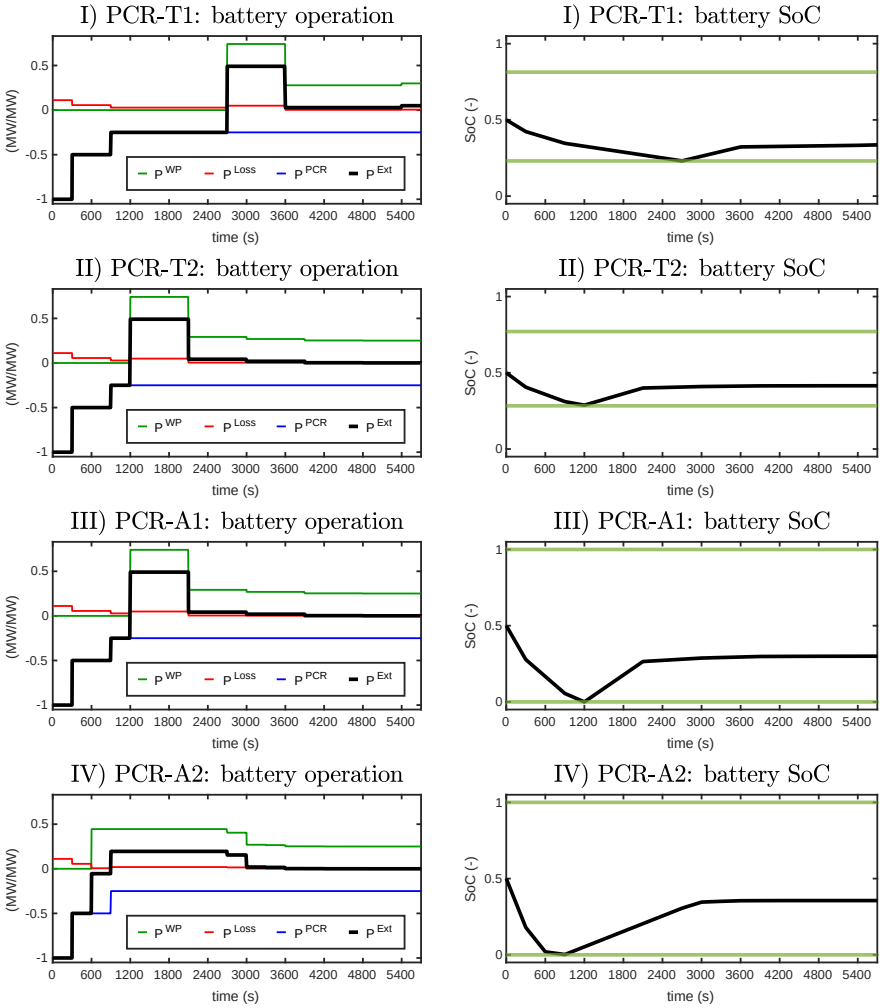

FIGURE 5.19: Provision of PCR under prequalification grid frequencies ($\mathbf{f}^p$). The model results were obtained for battery systems with the following parameters: energy capacity (C_{bat}): $1\,MWh$, power rating (r_{bat}): $5\,MW/MWh$, battery state of health (SoH_{bat}): 100%, energy efficiency of the battery system (η^{tot}): 90%, battery state of charge level at $t = 0$ (SoC^{init}): 50%. The left-hand side of the figure shows varying power flows: P^{WP} (green) is the working point, P^{Loss} (red) denotes the internal energy losses in the battery system, P^{PCR} (blue) corresponds to the control signal, and P^{Ext} (black) denotes the total power exchanged between the battery system and the electricity grid. A positive sign for P^{Ext} indicates battery charging, whereas a negative sign indicates battery discharging. All power flows have units $[MW/MW]$, as they are normalized by the amount of PCR capacity provided by the battery system, which is dependent on the electricity market conditions: $C^{PCR} = 0.83\,MW$ (*PCR-T1*), $C^{PCR} = 1.02\,MW$ (*PCR-T2*), $C^{PCR} = 2.40\,MW$ (*PCR-A1*), and $C^{PCR} = 3.46\,MW$ (*PCR-A2*). The right-hand side of the figure shows the evolution of the battery SoC level. The green lines indicate the boundaries of the allowed SoC range. In the case studies III and IV, battery operators are allowed to use the full SoC range of the battery system, as no energy reserves need to be kept (i.e., $\tau^{Res} = 0$).

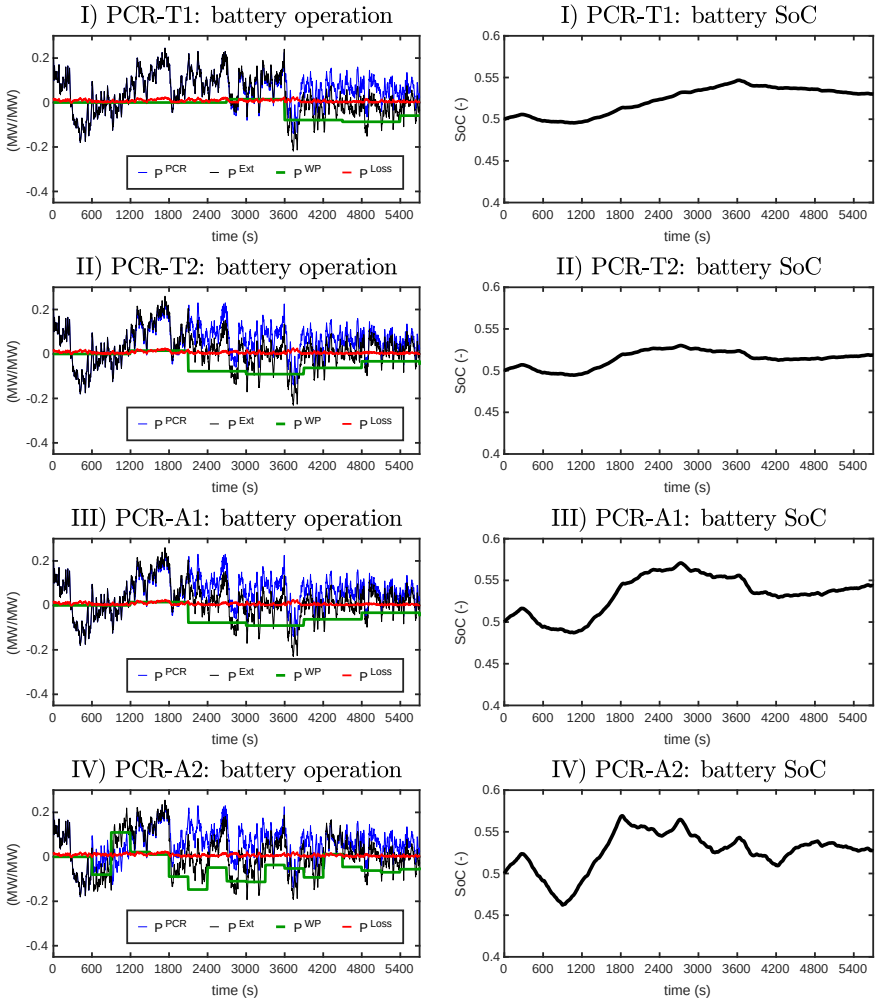

FIGURE 5.20: Example illustrating the provision of PCR under measured grid frequencies (time period of 5,700 seconds in the year 2019, Switzerland). The model results were obtained for battery systems with the following parameters: energy capacity (C_{bat}): $1\,MWh$, power rating (r_{bat}): $5\,MW/MWh$, battery state of health (SoH_{bat}): 100%, energy efficiency of the battery system (η^{tot}): 90%, battery state of charge level at $t = 0$ (SoC^{init}): 50%. The left-hand side of the figure shows varying power flows: P^{WP} (green) is the working point, P^{Loss} (red) denotes the internal energy losses in the battery system, P^{PCR} (blue) corresponds to the control signal, and P^{Ext} (black) denotes the total power exchanged between the battery system and the electricity grid. A positive sign for P^{Ext} indicates battery charging, whereas a negative sign indicates battery discharging. All power flows have units $[MW/MW]$, as they are normalized by the amount of PCR capacity provided by the battery system, which is dependent on the electricity market conditions: $C^{PCR} = 0.83\,MW$ (*PCR-T1*), $C^{PCR} = 1.02\,MW$ (*PCR-T2*), $C^{PCR} = 2.40\,MW$ (*PCR-A1*), and $C^{PCR} = 3.46\,MW$ (*PCR-A2*). The right-hand side of the figure shows the evolution of the battery SoC level.

5.5.3 *Profitability assessment*

Figure 5.21 shows the profitability (left) and optimal configuration (right) of battery systems providing PCR under varying electricity market conditions. The model results were obtained using electricity prices for the year 2019 and PCR remuneration data for the period from January to June 2019.[15] The profitability index is higher than 100% under all considered scenarios, hence battery deployment is profitable. The model results are shown for batteries with Wöhler coefficients $W = 1$ (e.g., LIBs with LFP cathodes [66–68]) and for batteries with $W = 2$ (e.g., LIBs with NMC cathodes [47, 53, 63]). Under the current electricity market scenarios (*PCR-T1* and *PCR-T2*), the Wöhler coefficient has only a minor impact on the PCR capacity that can be provided, thus the economic assessment of the two technologies is similar. This is because the offered PCR capacity corresponds (almost) to the theoretical one (i.e., $C^{PCR}_{offered} \approx C^{PCR}_{theor}$), as the cycle lifetime is generally not a limiting factor.

Under the alternative electricity market scenarios (*PCR-A1* and *PCR-A2*), battery operators are allowed to exploit the full SoC range of the battery system, as no additional energy reserves need to be kept ($\tau^{Res} = 0$). As a consequence, higher PCR capacities can be provided if the battery cycle lifetime does not constitute a limiting factor. As the provision of the PCR service results mainly in very shallow cycles, batteries with $W = 2$ degrade less than batteries with $W = 1$.[16] For this reason, batteries with $W = 2$ can provide higher PCR capacities (hence, $C^{PCR}_{offered} = C^{PCR}_{theor}$) than batteries with $W = 1$, for which the cycle lifetime becomes a limiting factor (hence, $C^{PCR}_{offered} < C^{PCR}_{theor}$). As a result, batteries with $W = 2$ are more profitable.

As shown in figure 5.21 (right), the electricity market conditions have also a significant impact on the optimal (i.e., most profitable) battery system configuration. This is because the higher the PCR capacity provided by the battery operator, the higher the charge and discharge power of the battery system. In order to exploit the high revenue potential of the alternative market scenarios (*PCR-A1* and *PCR-A2*), battery systems therefore require high power ratings $r_{bat} \geq 3\,MW/MWh$. However, high power ratings are beneficial only if the cycle lifetime does not constitute a limiting factor. As discussed above, this is the case for batteries with $W = 2$.

[15] The provision of PCR in the *whole* year 2019 is analyzed using PCR remuneration data for the period from January to June 2019 (i.e., the same compensation payments are assumed for the second half of 2019).

[16] When exposed to *shallow* cycles, i.e., $\delta < \delta_{ref}$, where $\delta_{ref} := 80\%$ is the DoD of a cycle under reference conditions, batteries with $W > 1$ perform less equivalent cycles (N^{ref}) than batteries with $W = 1$ (see eq. 4.23). When exposed to *deep* cycles, i.e., $\delta > \delta_{ref}$, the opposite is the case, and batteries with $W = 1$ degrade less than batteries with $W > 1$.

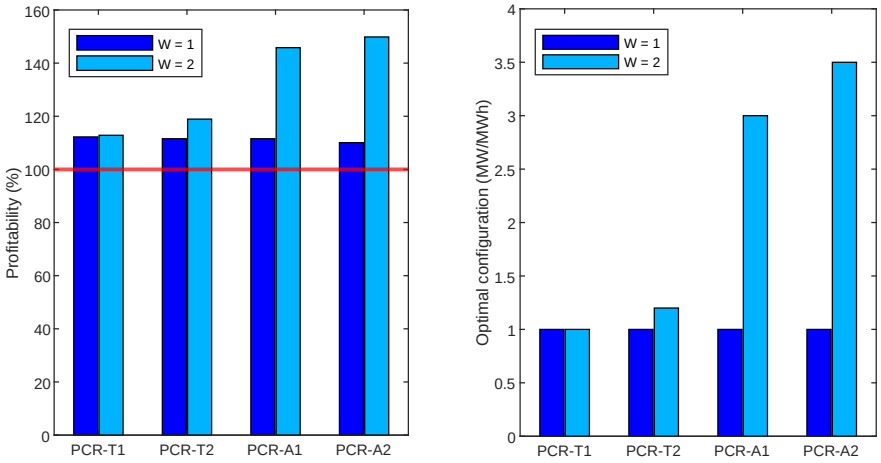

FIGURE 5.21: Profitability (left) and optimal configuration (right) of battery systems providing PCR under varying electricity market scenarios. The model results were obtained for battery systems with the following parameters: Cycle lifetime (EoL_{cyc}): 6,000 cycles at 80% DoD, calendar lifetime (EoL_{cal}): 15 years, energy efficiency of new battery packs ($\eta^{bat,0}$): 95%. These parameters correspond to the *base* scenario (#0) in table 5.1. Model results for batteries with Wöhler coefficients $W = 1$ and $W = 2$ are shown in dark blue and light blue, respectively. Battery deployment is profitable if the profitability index is higher than 100%, which is indicated by the red line.

Figure 5.22 shows the profitability (left) and the lifetime revenues (right) of battery systems with varying power ratings. For batteries with $W = 1$, the lifetime revenues scale roughly linearly with r_{bat} at low power ratings ($r_{bat} \leq 1\,MW/MWh$). This trend changes at higher power ratings ($r_{bat} > 1\,MW/MWh$) where the PCR revenues are no longer dependent on the configuration of the battery system. The situation is different for batteries with $W = 2$, for which power ratings up to $1.4\,MW/MWh$ (*PCR-T2*), $3.0\,MW/MWh$ (*PCR-A1*), or $5.5\,MW/MWh$ (*PCR-A2*) provide an additional benefit. As a consequence, the profitability index of these batteries peaks at power ratings of $1.2\,MW/MWh$ (*PCR-T2*), $3.0\,MW/MWh$ (*PCR-A1*), or even $3.5\,MW/MWh$ (*PCR-A2*), as the additional revenues justify the higher investment and O&M costs associated with the larger power units.

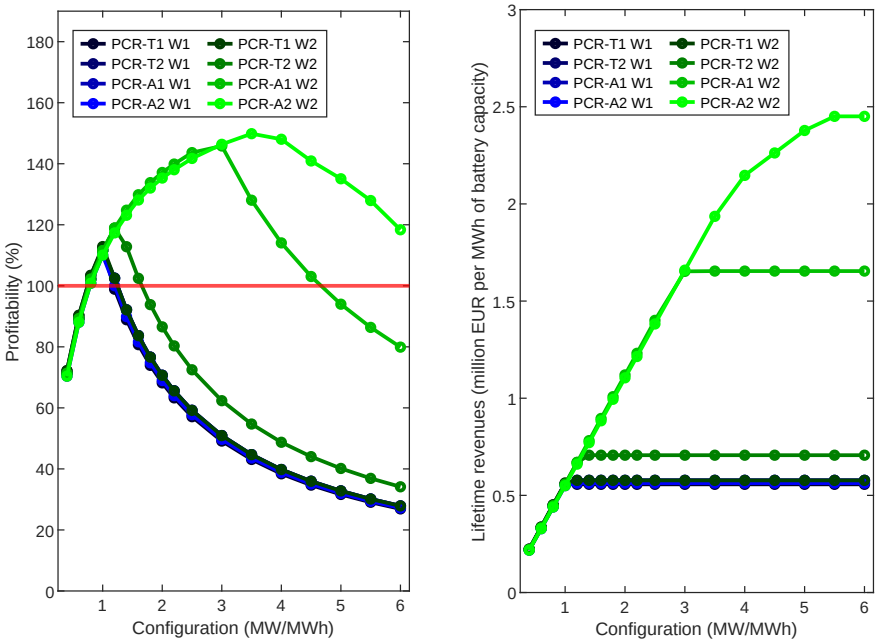

FIGURE 5.22: Profitability (left) and lifetime revenues (right) of battery systems with varying power ratings providing PCR under different electricity market scenarios. The model results were obtained for battery systems with the following parameters: Cycle lifetime (EoL_{cyc}): 6,000 cycles at 80% DoD, calendar lifetime (EoL_{cal}): 15 years, energy efficiency of new battery packs ($\eta^{bat,0}$): 95%. These parameters correspond to the *base* scenario (#0) in table 5.1. Model results for batteries with Wöhler coefficients $W = 1$ and $W = 2$ are shown in blue and green, respectively. Battery deployment is profitable if the profitability index is higher than 100%, which is indicated by the red line.

If neither the power rating nor the cycle lifetime are limiting factors, the electricity market conditions have a big impact on the amount of PCR capacity battery systems can provide and hence on their lifetime revenues[17] (see figure 5.22, right). By contrast, the market conditions have only a comparatively small impact on the profitability of battery systems[18] (see figure 5.22, left). Although these findings may seem somewhat contradictory, they can be explained by the high power-specific investment costs of battery systems. For instance, while the investment costs of battery systems designed for *medium power* applications ($r_{bat} = 1\,MW/MWh$) amount to ca. 409,000 EUR/MWh, the investment costs of battery systems with *very high* power ratings ($r_{bat} = 5.5\,MW/MWh$) are significantly higher, i.e., roughly 1,567,000 EUR/MWh (see chapter 5.1 for the details of the battery system cost model). Hence, battery systems that can fully exploit

[17] The lifetime revenues range from 577,000 *EUR* per *MWh* of battery capacity (*PCR-T1*) to 2,451,000 *EUR* per *MWh* of battery capacity (*PCR-A2* scenario).

[18] The profitability index ranges from 113% (*PCR-T1*) to 150% (*PCR-A2*).

the high revenue potential of the *PCR-A2* market conditions are currently 3.8 times more costly than battery systems designed for *medium power* applications. These considerations suggest that the viability of batteries providing PCR services does not only depend on the design of the regulation and electricity markets but to a large extent also on the future cost reduction that can be achieved for *high power* battery cells[19], AC/DC power inverters, and other components that are more costly for battery systems with higher power ratings.

Based on the presented model results, it is argued that the implementation of less stringent prequalification criteria (e.g., in terms of energy reserves) would certainly be beneficial from the viewpoint of a battery system operator (see also Ref. [139] for a discussion of this matter). However, a less stringent regulatory framework would not *per se* guarantee that the profitability of battery systems can be significantly increased. This is because the ability of stationary batteries to provide higher PCR capacities and hence increase revenues depends not only on the regulatory conditions but also on the power rating and cycle lifetime of the battery system. While the cycle lifetime of today's LIBs is not a limiting factor for batteries with $W = 2$, the high power-specific investment costs reduce the profitability of battery systems designed for power intense applications.

Compensation payments for the provision of PCR services have declined in the past years[20], which reduces the revenues of PCR units. Figure 5.23 compares the profitability of battery systems under 2017 and 2019 market conditions. Due to the declining remuneration of the PCR service, the business case has become considerably less attractive for battery operators within only two years. If the downward trend continues, the provision of PCR services will only be economically viable in the future if the battery system costs can be further reduced.

[19] Emerging technologies, such as sodium-ion batteries (NIBs) could potentially offer high power capabilities at lower investment costs than LIBs (see chapter 3 for an in-depth discussion of the performance and costs of different battery chemistries).

[20] Compensation payments for the provision of PCR can be obtained from Ref. [153].

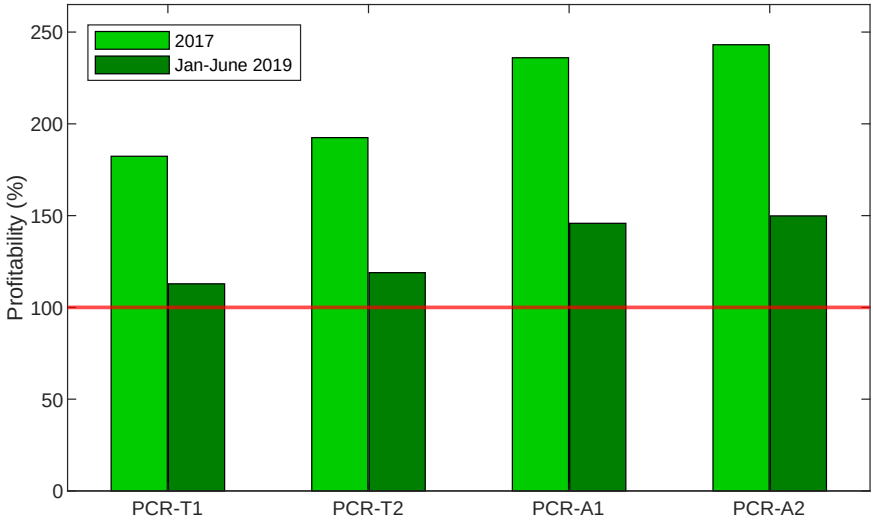

FIGURE 5.23: Profitability of providing PCR services under different electricity market scenarios, considering the remuneration of PCR in 2017 and 2019 (January-June). The model results are shown for batteries with Wöhler coefficients $W = 2$.

5.5.4 *Evaluation of battery research targets*

Figure 5.24 compares the profitability of battery systems providing PCR services under different development scenarios for today's LIBs (see table 5.1). The shown ranges indicate how much the profitability of battery systems could be increased by improving their performance parameters from current *base* values (bullets (•) and (•) for $W = 1$ and $W = 2$, respectively) to the enhanced values of the 15 development scenarios detailed in table 5.1 (upper end of the vertical solid lines). Only the model results obtained for the most profitable battery system configurations are shown.

Whereas the second life (SL) usability ranks consistently as one of the two most influential parameters, the impact of the cycle lifetime (Cy) varies significantly across the different electricity market scenarios. Under the *PCR-T1* scenario, longer cycle lifetimes would have only a minor impact on the profitability of batteries with $W = 1$ and no impact at all for batteries with $W = 2$. By contrast, under the *PCR-A1* and *PCR-A2* scenarios, improving the cycle lifetime becomes the most important development target for batteries with $W = 1$, as the cycle lifetime does in this case strongly affect the amount of PCR capacity the battery system can provide. However, for batteries with $W = 2$, the cycle lifetime is still not a limiting factor.

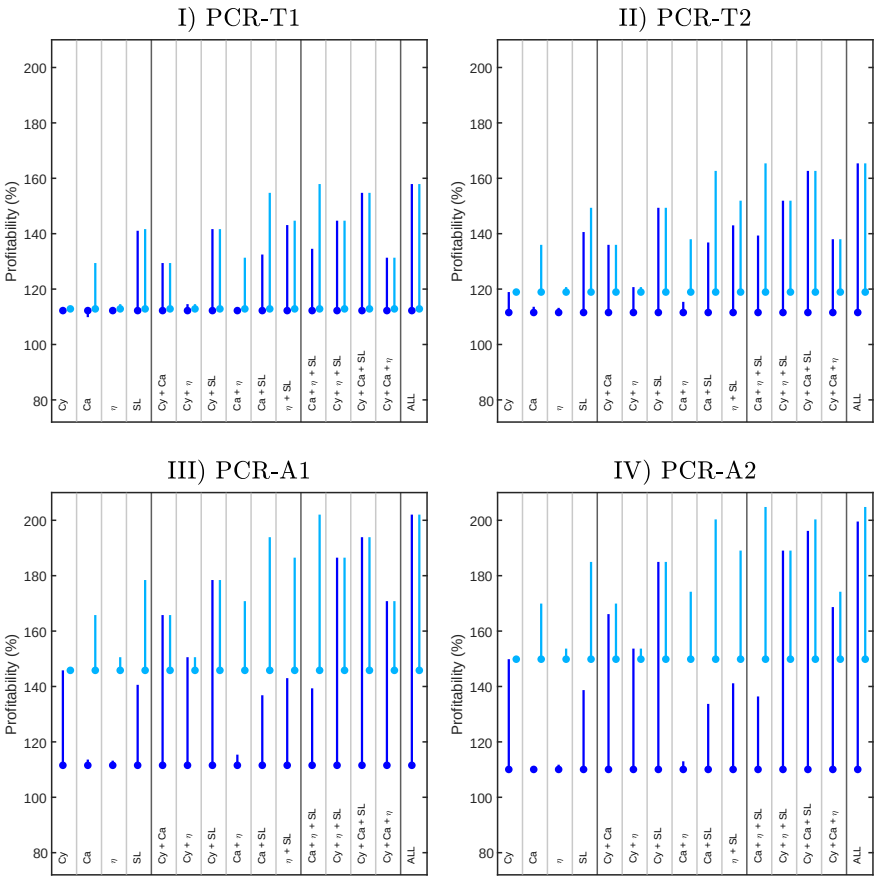

FIGURE 5.24: Profitability of battery systems providing PCR services under different development scenarios for today's LIBs (see table 5.1). The shown ranges (vertical solid lines) indicate how much the profitability of battery systems could be increased in each development scenario, whereas the bullets ((•) and (•)) for $W = 1$ and $W = 2$, respectively) refer to the *base* scenario (i.e., performance of LIBs today). Used symbols and abbreviations: Cycle lifetime (Cy), calendar lifetime (Ca), energy efficiency of the battery system (η), and second life (SL) usability. Only the model results obtained for battery systems with optimized power ratings (r^*_{bat}) are shown. The battery system costs were computed based on the costs of battery packs and power units in the year 2019, and a discount rate (r_d) of 4% was assumed (see chapter 5.1 for the details of the battery system cost model and table A2 for the model parameters).

5.6 SUMMARY

Based on the modeling framework developed in chapter 4, this chapter presented a techno-economic assessment of stationary battery systems providing PS, PA, and PCR services under a wide range of electricity market conditions. Figure 5.25 summarizes the results of the assessment in terms of battery profitability and research priorities for the further improvement of today's LIBs. Green colors are used to highlight application cases that are currently profitable (i.e., under battery system costs in the year 2019 and technical parameters representative of state-of-the-art LIBs), and red colors indicate that battery deployment is currently not profitable. The black bars indicate the priority of different battery development targets: improving the cycle lifetime (Cy), improving the calendar lifetime (Ca), improving the energy efficiency (η), and enabling second life (SL) use. The first of the four bars refers to the development target that would currently have the biggest impact on the profitability of battery systems. The second, third, and last bar indicates the combined impact of improving two, three, and four performance parameters of today's LIBs, respectively. The height of the bars represents the economic benefits associated with the different development scenarios. Note that the bars indicate the *percentage* increase in the battery's profitability index (and *not* the *percentage point* increase).

Figure 5.25 (top left, highlighted in red) illustrates that the deployment of stationary batteries for PA alone is currently not economically viable in Switzerland and Germany. The profitability index is only 11% (day-ahead market 2019 in Switzerland) and 38% (intraday market 2019 in Germany), indicating that the lifetime costs of battery systems currently exceed the lifetime revenues by a factor of 9.2 and 2.6, respectively. These results suggest that today's LIBs would need further technical improvement and significant cost reduction in order to reach economic viability when used exclusively for PA.

The impact of more volatile electricity prices on battery profitability is illustrated for simulated future electricity prices in Switzerland (Figure 5.25, bottom left). In the two considered scenarios, the profitability index is 47% (year 2030) and 133% (year 2050), indicating that the provision of PA services could potentially become a viable business case over the next decades. It should be noted that these model results were obtained for current battery system costs (year 2019). As the anticipated decline in costs is not taken into account, the profitability of battery systems providing PA on future electricity markets (*PA30* and *PA50* scenarios) is generally underestimated. A literature survey of cost projections for utility-scale battery systems for the years 2020 to 2050 is provided in Ref. [151].

Figure 5.25 (left) shows that the economic benefits of improving different performance parameters depend on the electricity market scenario considered. In the *Day-ahead 2019* scenario, the energy efficiency (η) is currently the most influential parameter: increasing the energy efficiency of today's battery packs from 95% to 97% would increase the profitability of battery systems by 29% ($W = 1$) and 31% ($W = 2$). Due to the comparatively small difference between peak and valley prices on the day-ahead market, PA revenues are strongly affected by the battery charge and discharge losses, explaining the high impact of the energy efficiency (η) on PA revenues. Notably, the other performance parameters become important development targets in a later stage of battery research. For instance, enabling second life (SL) use becomes the main development goal once the energy efficiency (η) has been improved, and longer cycle (Cy) and calendar (Ca) lifetimes become important in a third and fourth stage of battery research, respectively. In general, the economic benefits of improving two or multiple performance parameters are not additive, explaining why development targets that have low priority today may become important in a later stage of battery research. In all other PA market scenarios, the cycle lifetime (Cy) or the second life (SL) usability currently rank as the most important parameters. Longer cycle lifetimes (Cy) are particularly desirable for batteries that perform PA on electricity markets with high price volatility (e.g., intraday market), as it would allow battery operators to increase PA revenues by charging and discharging the battery system several times per day. This is especially the case for batteries with $W = 1$, where cycle lifetimes of 25,000 (instead of 6,000) cycles would increase the profitability by 50%. On the intraday market, a considerable share of the maximum possible PA revenues (i.e., revenues from batteries that have an unlimited cycle lifetime) can be generated by using battery systems mainly for shallow cycles. As this causes less degradation in batteries with $W = 2$ than in batteries with $W = 1$, the limited cycle lifetime of today's LIBs is somewhat less critical if $W = 2$.

Figure 5.25 (top right, highlighted in green) illustrates that the deployment of batteries for combined PS and PA would be economically viable for the case studies analyzed in this thesis. Due to the high revenue potential of PS, battery deployment is significantly more profitable than in the case of pure PA usage (see figure 5.25 top left). Enabling second life (SL) use of batteries would result in a 25% increase in profitability. Hence, extending their lifetime beyond 80% remaining capacity is currently the most important development target for batteries providing PS services. As the energy efficiency (η) and the cycle lifetime (Cy) affect mainly the PA revenues (which contribute relatively little to the total revenues), improving these parameters would only have a minor impact on battery profitability.

The *optimal* power rating (r^*_{bat}) of battery systems providing PA services ranges from 0.3 to 0.5 MW/MWh under the different electricity market scenarios. By contrast, PS

requires battery systems that are able to supply power mainly for short periods of time. Hence, the optimal power rating is significantly higher in the case of combined PS and PA usage (ca. 2 MW/MWh in the considered examples). In general, *small* battery systems offer the best ratio between PS revenues and battery investment costs and are therefore considered the preferred choice for PS applications.

The economics of providing PCR services is summarized in the bottom right of figure 5.25. The profitability index ranges from 112% (*current* electricity market conditions in Switzerland) to 150% (*alternative* scenario with less stringent PCR prequalification criteria). Notably, the benefits of less stringent regulatory conditions can only be exploited if battery systems are deployed that are able to sustain a *high* number of *shallow* charge and discharge cycles. Without further improvements of the cycle lifetime (Cy), this is currently the case for batteries with $W = 2$, such as LIBs with NMC cathodes [47, 53, 63]. For batteries with $W = 2$, enabling second life (SL) use by extending their lifetime beyond 80% remaining capacity is currently the most desirable development target in all considered PCR scenarios. A second lifetime (SL) would increase the profitability of battery systems by 23% to 26%.

The regulatory conditions imposed by the TSO do not only impact the economic viability of battery systems providing PCR (as illustrated in figure 5.25) but also their *optimal* power rating (r^*_{bat}). Under *current* market conditions, the optimal power rating ranges from 1.0 to 1.2 MW/MWh. By contrast, power ratings of $\geq 3.0\,MW/MWh$ are required to exploit the higher revenue potential of the *alternative* market scenarios.

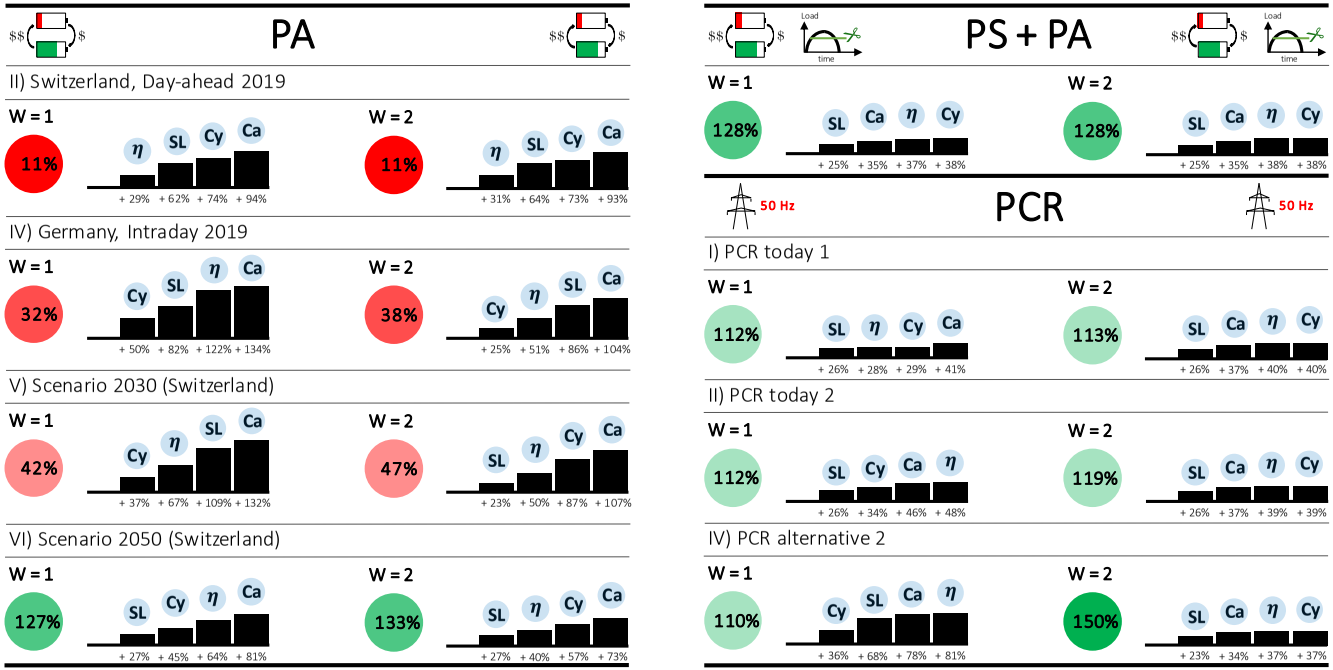

FIGURE 5.25: Summary of the model results. The profitability index (PI_{bat}) ranges from 11% (*PA, Day-ahead 2019*) to 150% (*PCR, alternative market scenario 2*). Green colors indicate that battery deployment is profitable ($PI_{bat} > 100\%$), whereas red colors indicate that battery deployment is not profitable ($PI_{bat} < 100\%$). The profitability index was computed assuming battery system costs in the year 2019 and technical parameters representative of today's LIBs (corresponding to the base scenario (#0) in table 5.1). The black bars indicate the priority of different battery development targets: improving the cycle lifetime (*Cy*), improving the calendar lifetime (*Ca*), improving the energy efficiency (η), and enabling second life (*SL*) use. The first of the four bars refers to the development target that would currently have the biggest impact on the profitability of battery systems. The second, third, and last bar indicates the combined impact of improving two, three, and four performance parameters of today's LIBs, respectively. The height of the bars represents the economic benefits associated with the different development scenarios. For instance, considering PA on the *Day-ahead* market in 2019 (Wöhler coefficient $W = 1$), improving η would increase the profitability by 29%, improving both η and *SL* would increase the profitability by 62%, improving η, *SL*, and *Cy* would increase the profitability by 74%, and improving all parameters would increase the profitability by 94%. In the last case, PI_{bat} would be increased from currently 11% to 21%.

6

CONCLUSIONS AND OUTLOOK

The viability of stationary energy storage in rechargeable batteries depends on multiple parameters related to the battery chemistry, battery manufacturing, and battery use phase. In this thesis, an assessment framework has been developed (i) to compare the technical, economic, and environmental performance of batteries on a cell level and (ii) to optimize the deployment of battery systems in a wide range of stationary application cases. The computational models have been applied to various case studies and business cases, and the model results have been used to formulate recommendations for further research on rechargeable batteries and the materials they are composed of. This chapter starts with an overview of the assessment framework developed in this thesis, along with a short discussion of the model results. Then, a *checklist* is presented that is intended to serve scientists and decision-makers in the field of chemistry and neighboring disciplines as a high-level guideline for battery research. The chapter concludes with an outlook on possible extensions of the developed assessment framework, new applications, and suggestions for future research.

6.1 BATTERY CELL ASSESSMENT

In order to evaluate the future potential of different battery chemistries from a holistic perspective, a modeling framework has been developed for the technical, economic, and environmental assessment of battery cells. In a first step, a physics-based electrochemical P2D model is employed to assess practical specific energies of intercalation-based battery cells under varying discharge rates. In a second step, the output of the P2D model is used to parameterize a bottom-up battery cell cost model and to assess GHG emissions of battery cells from a life cycle perspective.

The developed modeling framework has been used to perform a comparative assessment of LIB and NIB cells. First, active material configurations are considered that are intended to be representative of today's LIBs and NIBs ($LiNi_{1/3}Co_{1/3}Mn_{1/3}O_2$ *vs.* graphite and $NaNi_{1/3}Co_{1/3}Mn_{1/3}O_2$ *vs.* hard carbon, respectively). The model results are in favor of LIBs, as significantly higher practical specific energies, lower manufacturing costs, and lower GHG emissions have been projected for LIBs. These findings suggest that the materials for NIBs need further improvement in order to make NIBs competitive with LIBs.

A strong inverse correlation has been found between the practical specific energy of battery cells and both their manufacturing costs and environmental impacts. By contrast, other drivers, such as cost savings due to the replacement of lithium-based materials by sodium-based ones, play only a relatively minor role under current raw material costs. NIBs are therefore most likely to become competitive with LIBs if their specific energy can be further increased. This translates into a need for anode and cathode active materials that offer higher specific charges, higher gravimetric densities, and higher voltages.

Whereas the further development of LIBs has received significant attention from academia and industry, NIBs are currently a less mature technology in their prototyping stage [5]. It is therefore expected that the ongoing research activities will eventually lead to the development of improved NIB active materials. In order to avoid that the future potential of NIBs is underestimated due to the currently different development stages of the two technologies, a second assessment has been performed. This assessment is representative of a hypothetical scenario where differences in battery performance originate solely from fundamental thermodynamic and kinetic disparities inherent to LIBs and NIBs. Under these assumptions, NIBs are projected to reach practical specific energies close to (for *high energy* NIB cells) or even somewhat higher (for *high power* NIB cells) than LIBs.

6.2 BATTERY SYSTEMS IN STATIONARY APPLICATIONS

A second part of this thesis has been devoted to the technical and economic assessment of battery systems providing grid-level energy storage. To this end, a modeling framework has been developed to analyze and optimize the provision of different services, including PS, PA, and PCR, under varying electricity market conditions.

As the rate of battery degradation is determined by the application case and operation profile of the battery system, degradation should be considered as an operational cost factor. Therefore, the Rainflow cycle counting algorithm has been implemented into an energy-economic modeling framework for battery sizing and dispatch planning. This ensures that the DoD-dependent degradation behavior of batteries can be modeled using technology-specific empirical fitting functions, which allows for an advanced representation of cycle degradation in the modeling framework.

6.2.1 *Peak shaving and price arbitrage*

The *PSPA model* is an optimization model that aims to provide dispatch schedules which maximize the combined revenues from PS and PA over the lifetime of the battery system. In a first step, the *short-term* (1 - 3 days) dispatch of battery systems is

formulated as a multi-objective optimization problem: (1) maximizing PA revenues, (2) minimizing the peak load (in order to maximize PS revenues), and (3) minimizing battery degradation. This optimization problem is solved multiple times to generate a set of Pareto optimal solutions between the three objectives. In a second step, the PSPA model solves a *long-term* (1 year) planning problem to determine which *short-term* Pareto optimal dispatch actions are optimal under a long-term perspective for battery operation.

The PSPA model has been applied to a number of case studies by determining optimal battery system configurations and optimal dispatch schedules. The model results reveal that the deployment of stationary batteries for PA alone is currently not economically viable in Switzerland and Germany. The PA revenues generated over the battery lifetime recover only 11% (day-ahead market 2019 in Switzerland) and 38% (intraday market 2019 in Germany) of the total battery system costs. These results suggest that today's LIBs need further technical improvement and significant cost reduction in order to make their use for PA profitable.

The impact of more volatile electricity prices on PA revenues has been quantified by analyzing the deployment of stationary batteries under simulated electricity prices for Switzerland in the year 2030 and 2050. Under these conditions, the PA revenues recover 47% (year 2030) and 133% (year 2050) of the total battery system costs, suggesting that the provision of PA services could potentially become a viable business case over the next decades.[1]

A Swiss distribution system operator has been considered as a case study to analyze the combined provision of PS and PA. Due to the high revenue potential of PS, the deployment of batteries would be economically viable for the assessed business cases.

For battery systems providing only PA, the *optimal* power rating (r^*_{bat}) ranges from 0.3 to 0.5 MW/MWh for the electricity markets considered in this thesis. The optimal power rating is defined in terms of maximizing the profitability of the battery system. By contrast, PS requires battery systems that are able to supply power mainly for short periods of time. Hence, the optimal power rating is significantly higher (ca. 2 MW/MWh in the considered case studies). In general, *small* battery systems offer

[1] The massive deployment of stationary batteries could potentially reduce the revenue opportunities in future electricity markets. As the PSPA model assumes that battery operators are price takers (i.e., electricity prices are provided as an external model input), such systems effects are not captured in the developed modeling framework. On the other hand, it should be noted that current costs (year 2019) are assumed for battery systems throughout this thesis (also for battery systems that perform PA on future electricity markets). The anticipated decline in costs for battery systems is therefore not considered in the model results. An overview and discussion of different cost projections for utility-scale battery systems is provided in Ref. [151]. Note that lower investment costs would, of course, increase the profitability of stationary battery systems.

the best ratio between PS revenues and battery investment costs and are therefore considered the preferred choice for the analyzed PS applications.

6.2.2 *Primary control reserves*

In contrast to the previous chapter, which is dedicated to PS and PA, the present chapter deals with PCR, where batteries are used to provide regulation power to the electricity grid. The *PCR model* is a simulation model that has been developed to assess the technical and economic viability of stationary battery systems providing PCR services. A moving average based SoC control scheme is considered to adjust the battery SoC level via charge/discharge power traded on the intraday electricity market. This ensures that battery systems are capable of providing the PCR service at (almost) all times. The PCR model has been used to analyze the provision of PCR services under (i) *current* electricity market conditions in Switzerland and (ii) under two *alternative* (hypothetical) market scenarios with less stringent regulatory conditions.

The provision of PCR services has been analyzed under current (year 2019) and historical (year 2017) PCR compensation payments. In both cases, the deployment of stationary batteries has been found to be economically viable. Under 2019 compensation payments, the revenues recovered over the battery lifetime range from 112% (*current* electricity market conditions in Switzerland) to 150% (*alternative* scenario with less stringent PCR prequalification criteria) of the total battery system costs. Notably, the model results reveal that the benefits of less stringent regulatory conditions can only be exploited if battery systems are deployed that are able to sustain a *high* number of *shallow* charge and discharge cycles. This is currently the case, e.g., for LIBs with NMC cathodes [47, 53, 63].

The regulatory conditions imposed by the TSO impact both the economic viability of battery systems and their *optimal* power rating (r^*_{bat}). Under *current* electricity market conditions, the optimal power rating ranges from 1.0 to 1.2 MW/MWh. By contrast, power ratings of $\geq 3.0\,MW/MWh$ are required to exploit the higher revenue potential of the *alternative* market scenarios.

6.3 IMPLICATIONS FOR BATTERY RESEARCH

6.3.1 *Battery cells*

In order to improve today's LIB cells and enable the successful market implementation of alternative cell chemistries, the following development targets should be prioritized:

- Increasing the specific charges of anode and cathode active materials.
- Increasing the gravimetric densities of anode and cathode active materials.
- Increasing the voltage of battery cells.

The above development targets have in common that they aim to increase the specific energy of battery cells. Due to the strong inverse correlation that has been found between the specific energy of battery cells and both their manufacturing costs and life cycle GHG emissions, higher specific energies would be beneficial not only from a technical but also from an economic and environmental point of view. By contrast, other parameters, such as the costs of raw materials (e.g., lithium carbonate), have been found to play only a relatively minor role under current market prices.

The main contributors to the life cycle GHG emissions of battery cells include the cathode and the energy required for battery cell manufacturing. Hence, increased recycling [154] of cathode active materials and the use of renewable energy sources for battery cell manufacturing would be beneficial from an environmental point of view.

6.3.2 *Battery systems in stationary applications*

In order to increase the economic viability of stationary battery systems, the following development targets should be prioritized:

- *Battery second life* → The second life use of batteries, which is enabled by extending their lifetime beyond 80% remaining capacity, is an important development target for all application cases considered in this thesis. The onset of accelerated degradation at ca. 80% remaining capacity could be mitigated by improving the electrode materials and the battery cell design.
- *Longer cycle lifetime* → Longer cycle lifetimes (Cy) would be desirable for batteries that perform PA on electricity markets with high price volatility, as it would allow battery operators to generate higher PA revenues by charging and discharging the battery system several times per day.
- *Higher energy efficiency* → Higher energy efficiency (η) would be desirable for batteries that perform PA on electricity markets with low price volatility. If the difference between peak and valley prices is small, PA revenues are strongly dependent on charge and discharge losses, explaining the high impact of the energy efficiency on PA revenues.
- *Ability to sustain many shallow cycles* → The provision of PCR requires batteries to perform many shallow charge and discharge cycles. As the cycle lifetime (Cy) is

currently a limiting factor for some of today's LIBs, the cycle stability should be improved so that they can sustain a higher number of shallow cycles.

- *Need for high power battery systems* → The provision of PCR requires battery systems with relatively high power ratings. Hence, it would be desirable to improve the performance and reduce the costs of high power battery cells and other components that are more costly for battery systems with high power ratings. From a materials point of view, the performance of high power battery cells depends on the availability of electrode materials that offer high specific charges, high gravimetric densities, high voltages, fast mass transport, and fast reaction kinetics at the electrode/electrolyte interface.

Importantly, the economics of stationary batteries does not only depend on technical parameters related to the above development targets but also on future cost reductions for battery systems, design of future electricity markets, regulatory conditions, energy and power specific electricity prices, and remuneration for the provision of PCR services. All of these impact factors should be considered by investors and decision-makers in order to account for the technical and economic uncertainties associated with stationary energy storage.

6.4 SUGGESTIONS FOR FUTURE RESEARCH

Model-based analysis of stationary energy storage can provide valuable insights into the optimal deployment and operation of grid-connected battery systems. In addition, it helps to establish guidelines and research targets for the further improvement of today's LIBs and related technologies. In order to further extend the scope and capabilities of the assessment framework presented in this thesis, the below sections provide suggestions for future research in the field of battery model development.

6.4.1 *Assessment of battery cells*

- *Broadening the technology scope:* The assessment of battery cells could be extended to a wider range of cell chemistries, including LIBs (e.g., based on graphite/silicon composite anodes and nickel- or lithium-rich cathodes [21]), NIBs, K-ion batteries (KIBs), and Al-ion batteries (AIBs). Such an extensive comparative assessment would shed additional light on how the viability of emerging battery chemistries is affected by physicochemical material properties[2], raw material costs, battery cell manufacturing processes, and material supply chains. The model results could be used to build a reference database, which would help scientists and decision-makers to recognize and evaluate the market prospects of new technologies at an early stage of research.

[2] i.e., kinetic parameters, specific charges, voltage profiles, and gravimetric densities of active materials and mass transport parameters of the electrolyte.

As the P2D model requires a large number of empirical input parameters, the proposed modeling activities should be accompanied by experimental studies dedicated to the determination of kinetic and thermodynamic parameters for a wide range of promising active materials. A practical challenge lies in the time-consuming nature of these studies, as they require the synthesis and electrochemical characterization of a large number of materials. A possible way around this problem could be to complement the experimental studies using data-driven machine-learning based methods. Data-driven models have in the past years emerged as a promising platform for the discovery of new materials and prediction of their properties based on existing data sets [155, 156].

- *Harmonization of LCA modeling assumptions:* Whereas several studies have been dedicated to the harmonization of LCA modeling assumptions for LIBs [7, 12, 157], further research is needed to establish and refine life cycle inventory data for emerging technologies. Existing LCA studies have concluded that the assessment of environmental impacts is highly dependent on the model assumptions [12]. Hence, more primary data on global material supply chains, material recycling, and battery cell manufacturing should be collected to avoid that any biases are introduced in the assessment of LIBs, NIBs, and related technologies.

6.4.2 *Assessment of grid-connected battery systems*

- *Analyzing more case studies:* In order to draw conclusions that are less case study specific and thus more generally valid, the developed assessment framework could be used to analyze the provision of PS and PA services under a wider range of load profiles and electricity prices. In a second step, unsupervised [158, 159] and supervised [160] learning methods could be employed (i) to group electricity consumers, based on their load profiles, into different consumer classes and (ii) to assess the impact of load-specific features (e.g., number of load peaks per day, *height* of the peaks, and peak *shapes*; see also Ref. [124]) and price-specific features (e.g., price volatility and peak load tariff) on PS and PA revenues. This would allow distribution system operators and business owners to assess the influence of case specific impact factors on the profitability of stationary battery systems. Notably, once trained, the use of supervised machine learning models as a complementary modeling approach would reduce the need to run a computationally expensive techno-economic optimization model every time a new business case is analyzed. In addition to analyzing more case studies for PS and PA, the developed modeling framework could be adapted to model use cases for stationary batteries in residential applications, such as increasing the self-consumption rate of households with installed solar photovoltaics (PV) [7, 160].

- *Refining the battery degradation model:* In order to tailor the assessment framework to the degradation behavior of a wide range of battery chemistries, the impact of the following stress factors on cycle and calendar degradation could be modeled: (i) average cycle SoC (σ_c), (ii) temperature (T), and (iii) current rate (r) [11, 161]. The implementation of these model refinements is straightforward in simulation settings (e.g., provision of PCR services) and merely requires the user of the PCR model to make some minor modifications to the Rainflow cycle counting procedure. By contrast, more care is needed in optimization settings (e.g., PSPA model). To ensure that the battery dispatch problem (4.4a)-(4.4g) preserves its convexity and hence can be solved efficiently (see chapter 4), the costs of battery degradation should be modeled using functions that are convex in the charge and discharge variables.

- *Long-term battery dispatch modeling:* The PSPA and PCR models rely on two key assumptions for the long-term dispatch modeling of stationary battery systems. First, it is assumed that battery systems perform the same number of cycles in each year, which is achieved by constraining the number of cycles per year to the ratio of the battery cycle and calendar lifetime. Second, a maximum-based ($L_{tot} = max\{L_{cal}, L_{cyc}\}$) approach is used to model the combined impact of calendar and cycle degradation, i.e., the battery is considered to be operational until it reaches the end of either the calendar or cycle lifetime. These modeling assumptions allow for a straightforward parameterization of the degradation model using calendar and cycle lifetime data provided by battery manufacturers and hence simplify the modeling process and the interpretation of model results obtained under different battery development scenarios. In future work, the application scope of the developed assessment framework could be further extended by implementing the PSPA and PCR models in a dynamic programming (DP) setting. Instead of constraining the number of cycles per year to a *fixed* number, an additional DP model could be formulated that determines the *optimal* number of cycles in each year.[3] This would extend the scope of the PSPA and PCR models to situations where (i) the electricity market conditions and thus the PS, PA, or PCR revenue opportunities are expected to change over time, (ii) the discount rate (r_d) is *high*, and/or (iii) additive ($L_{tot} = L_{cal} + L_{cyc}$) or multiplicative ($L_{tot} = L_{cal} \cdot L_{cyc}$) degradation models are more suitable than maximum-based ($L_{tot} = max\{L_{cal}, L_{cyc}\}$) ones.

[3] Both the PSPA and PCR models compute the revenues in each year (R_y) as a function of the battery degradation level (L_{tot}) and the number of cycles (N^{ref}), i.e., $R_y = R_y(L_{tot}, N^{ref})$. These are the same quantities that would be required by an additional DP model, where the battery degradation level (L_{tot}) corresponds to the *state* variable, and the number of cycles (N^{ref}) allocated to each year is the *control* variable. The degradation level (L_{tot}) describes the *state* of the battery system, i.e., its state of health (SoH_{bat}) (see eq. 4.28) and energy efficiency (see eq. 4.29). Instead of the number of cycles (N^{ref}), one could use other definitions of the control variable to express the fraction of the battery lifetime used up in each year, such as the degradation increment (ΔL_{tot}). Such a generic definition of the *control* variable offers the advantage of being compatible with any (combined) calendar and cycle degradation model that can be formulated as a function of battery charge and discharge.

- *Consideration of alternative objectives:* The PSPA and PCR models have been developed to assess the economics of grid-connected battery systems from the perspective of an investor that seeks to maximize economic revenues. In future work, the deployment and optimal operation of battery systems could be analyzed under alternative objectives such as total energy system cost minimization and environmental impact reduction [63, 162, 163].

A

APPENDIX

A.1 MODEL PARAMETERS

TABLE A1: P2D model parameters: parameter values for the comparative assessment of LIB and NIB cells discussed in chapter 3 of the thesis.

Symbol	Units	Parameter description	Parameter value	Reference and comments
l_y	m	Half of the thickness of the cathode current collector (Al sheet for both the LIB and NIB)	LIB: $10 \cdot 10^{-6}$ NIB: $10 \cdot 10^{-6}$	LIB: Ref. [101] NIB: Ref. [101]
l_z	m	Half of the thickness of the anode current collector (Cu sheet for LIB and Al sheet for NIB)	LIB: $4 \cdot 10^{-6}$ NIB: $4 \cdot 10^{-6}$	LIB: Ref. [101] NIB: same value assumed as for LIB
l_c	m	Thickness of cathode	Variable	Subject to optimization
l_a	m	Thickness of anode	Variable	Subject to optimization
l_s	m	Thickness of separator	$25 \cdot 10^{-6}$	Celgard specification sheet
ϵ_c	$[-]$	Porosity of cathode	Variable	Subject to optimization
ϵ_a	$[-]$	Porosity of anode	Variable	Subject to optimization
ϵ_s	$[-]$	Porosity of separator	0.39	Celgard specification sheet
$\epsilon_{f,c}$	$[-]$	Filler fraction cathode (total volume fraction of binder + conductive additive in porous cathode)	$\epsilon_{f,c} = \frac{0.07\rho_c - 0.07\epsilon_c\rho_c}{0.93\rho_f + 0.07\rho_c}$	Electrode composition: 93 wt.% active material and 7 wt.% filler (3 wt.% binder + 4 wt.% conductive additive)
$\epsilon_{f,a}$	$[-]$	Filler fraction anode (total volume fraction of binder + conductive additive in porous anode)	$\epsilon_{f,a} = \frac{0.07\rho_a - 0.07\epsilon_a\rho_a}{0.93\rho_f + 0.07\rho_a}$	Electrode composition: 93 wt.% active material and 7 wt.% filler (3 wt.% binder + 4 wt.% conductive additive)
c_e^{init}	mol/m^3	Initial Li^+ or Na^+ concentration in electrolyte	1,000	Assumed
$c_{s,c}^{max}$	mol/m^3	Maximum solid phase Li^+ or Na^+ concentration in cathode active material	LIB: 49,200 NIB present: 42,200 NIB hypothetical: 49,200	Calculated parameter values
$c_{s,c}^{init}$	mol/m^3	Initial solid phase Li^+ or Na^+ concentration in cathode active material	LIB: $0.44\, c_{s,c}^{max}$ = 21,648 NIB present: $0.50\, c_{s,c}^{max}$ = 21,100 NIB hypothetical: $0.44\, c_{s,c}^{max}$ = 21,648	LIB: calculated based on Ref. [42] NIB present: calculated based on Ref. [113]
$c_{s,a}^{max}$	mol/m^3	Maximum solid phase Li^+ or Na^+ concentration in anode active material	LIB: 30,500 NIB present: 20,900 NIB hypothetical: 30,500	NIB present: calculated based on Ref. [110]

$c_{s,a}^{init}$	mol/m^3	Initial solid phase Li^+ or Na^+ concentration in anode active material	LIB: 0.90 $c_{s,a}^{max}$ = 27,450 NIB present: 0.90 $c_{s,a}^{max}$ = 18,810 NIB hypothetical: 0.90 $c_{s,a}^{max}$ = 27,450	Calculated parameter values
$c_{s,a}^{min,avg}$	mol/m^3	Minimum average solid phase Li^+ or Na^+ concentration in anode active material (equivalent to cut-off state-of-charge)	LIB: 0.01 $c_{s,a}^{max}$ = 305 (cut-off SoC = 1%) NIB present: 0.10 $c_{s,a}^{max}$ = 2,090 (cut-off SoC = 10%) NIB hypothetical: 0.01 $c_{s,a}^{max}$ = 305 (cut-off SoC = 1%)	Calculated parameter values
$D_{s,c}$	m^2/s	Solid phase diffusion coefficient of Li^+ or Na^+ in the cathode	LIB: $4 \cdot 10^{-15}$ NIB: $4 \cdot 10^{-15}$	LIB: similar to Ref. [164] NIB: same value assumed as for LIB
$D_{s,a}$	m^2/s	Solid phase diffusion coefficient of Li^+ or Na^+ in the anode	LIB: $4.02 \cdot 10^{-14}$ NIB: $4.02 \cdot 10^{-14}$	LIB: similar to Ref. [34] NIB: same value assumed as for LIB
D_e	m^2/s	Electrolyte diffusion coefficient of Li^+ or Na^+	LIB: $3 \cdot 10^{-10}$ NIB pessimistic: $3 \cdot 10^{-10}$ NIB base: $3.84 \cdot 10^{-10}$ NIB optimistic: $6 \cdot 10^{-10}$ The Bruggeman relation is used to compute effective diffusion coefficients: $D_{e,eff,i} = D_{e,i}\epsilon_i^{brugg_i},\ i \in \{c,s,a\}$	LIB: assumed based on Ref. [38] NIB: In the base scenarios, it is assumed that electrolyte diffusion coefficients (Li^+ vs. Na^+) are proportional to self-diffusion coefficients of Li^+/Na^+ in diluted aqueous solution [111].
k_c	$m^{2.5}/(mol^{0.5}s)$	Heterogeneous reaction rate constant cathode	LIB: $2 \cdot 10^{-11}$ NIB pessimistic: $2 \cdot 10^{-11}$ NIB base: $2 \cdot 10^{-9}$ NIB optimistic: $2 \cdot 10^{-8}$	LIB: value from Ref. [42] NIB: The scenarios are defined based on Refs. [96–98]. Note that if desolvation is the rate-limiting step in the charge transfer reaction, the heterogeneous rate constant may be several orders of magnitude higher in NIBs than LIBs.
k_a	$m^{2.5}/(mol^{0.5}s)$	Heterogeneous reaction rate constant anode	LIB: $2 \cdot 10^{-11}$ NIB pessimistic: $2 \cdot 10^{-11}$ NIB base: $2 \cdot 10^{-9}$ NIB optimistic: $2 \cdot 10^{-8}$	LIB: value from Ref. [42] NIB: The scenarios are defined based on Refs. [96–98]. Note that if desolvation is the rate-limiting step in the charge transfer reaction, the heterogeneous rate constant may be several orders of magnitude higher in NIBs than LIBs.
$R_{p,c}$	m	Particle radius of cathode active material particles	LIB: $2 \cdot 10^{-6}$ NIB: $2 \cdot 10^{-6}$	Assumed
$R_{p,a}$	m	Particle radius of anode active material particles	LIB: $2 \cdot 10^{-6}$ NIB: $2 \cdot 10^{-6}$	Assumed
ρ_y	kg/m^3	Density of cathode current collector	LIB: 2,700 NIB: 2,700	LIB: value from Ref. [101] NIB: value from Ref. [101]
ρ_z	kg/m^3	Density of anode current collector	LIB: 8,960 NIB: 2,700	LIB: value from Ref. [101] NIB: value from Ref. [101]

ρ_c	kg/m^3	Density of cathode active material (fully lithiated/sodiated state)	LIB: 4,750 NIB: 4,750	LIB: value from Ref. [101] NIB: same value assumed as for NIB
ρ_a	kg/m^3	Density of anode active material (fully delithiated/desodiated state)	LIB: 2,200 NIB present: 1,700 NIB hypothetical: 2,200	LIB: value from Ref. [101] NIB present: assumed NIB hypothetical: assumed
ρ_b	kg/m^3	Density of binder	LIB: 1,800 NIB: 1,800	LIB: value from Ref. [101] NIB: same value assumed as for LIB
ρ_{cond}	kg/m^3	Density of conductive additive	LIB: 2,260 NIB: 2,260	LIB: value from Ref. [101] NIB: same value assumed as for LIB
ρ_f	kg/m^3	Density of filler (mixture of binder + conductive additive in 3:4 wt. ratio)	LIB: 2,063 NIB: 2,063	Calculated parameter values
ρ_e	kg/m^3	Density of electrolyte	LIB: 1,200 NIB: 1,200	LIB: value from Ref. [101] NIB: same value assumed as for NIB
ρ_s	kg/m^3	Density of separator polymer	LIB: 946 NIB: 946	LIB: value from Ref. [101] NIB: same value assumed as for NIB
σ_c	S/m	Electronic conductivity of composite cathode	LIB: 1 NIB: 1 The effective electronic conductivity of the porous electrode is computed as follows: $\sigma_{eff,c} = \sigma_c(1-\epsilon_c)$	Assumed
σ_a	S/m	Electronic conductivity of composite anode	LIB: 10 NIB: 10 The effective electronic conductivity of the porous electrode is computed as follows: $\sigma_{eff,a} = \sigma_a(1-\epsilon_a)$	Assumed
a_c	m^2/m^3	Specific interfacial area of cathode (i.e., specific area of active material per unit volume of porous cathode)	$a_c = \frac{3(1-\epsilon_c-\epsilon_{f,c})}{R_{p,c}}$	Calculated parameter values
a_a	m^2/m^3	Specific interfacial area of anode (i.e., specific area of active material per unit volume of porous anode)	$a_a = \frac{3(1-\epsilon_a-\epsilon_{f,a})}{R_{p,a}}$	Calculated parameter values
$brugg_i$	$[-]$	Bruggeman coefficient in cathode, separator, and anode	LIB: 2.5 NIB: 2.5	Values assumed based on Ref. [37]

t_+	$[-]$	Transference number of Li^+ or Na^+	LIB: 0.4 NIB pessimistic: 0.4 NIB base: 0.5 NIB optimistic: 0.5	Values assumed based on Ref. [165]
F	C/mol	Faraday constant	96,485	
R	$mol/(JK)$	Universal gas constant	8.3145	

Additional P2D model parameters (chapter 3)

- Electrolyte ionic conductivity $\kappa_e(c_e)$ $[S/m]$ in LIBs: fit to measured conductivity of $LiPF_6$ in EC:DMC (3 : 7 wt.) in Ref. [112], $T = 30°C$ is assumed:

$$\kappa_e(c_e) = 3.01 \cdot 10^{-3} c_e - 2.4845 \cdot 10^{-6} c_e^2 + 8.9583 \cdot 10^{-10} c_e^3 - 1.241 \cdot 10^{-13} c_e^4$$

- Electrolyte ionic conductivity $\kappa_e(c_e)$ $[S/m]$ in NIBs:
  - Pessimistic scenarios: $\kappa_e^{NIB}(c_e) = \kappa_e^{LIB}(c_e)$
  - Base scenarios: $\kappa_e^{NIB}(c_e) = 1.2 \cdot \kappa_e^{LIB}(c_e)$
  - Optimistic scenarios: $\kappa_e^{NIB}(c_e) = 1.5 \cdot \kappa_e^{LIB}(c_e)$
- Open circuit potential of LIB active materials:
  - Graphite: Ref. [34]
  - $LiNi_{1/3}Co_{1/3}Mn_{1/3}O_2$: Ref. [42]
- Cut-off voltage:
  - LIB: $2.80\,V$
  - NIB present scenarios: $1.80\,V$
  - NIB hypothetical scenarios: $2.47\,V$
- Open circuit potential of NIB active materials:
  - Hard carbon (fit to discharge curve in Ref. [110]):

$$\begin{aligned} U = 0.06319 &+ 14.18 \cdot exp(-16.84\theta) - 1.402 \cdot exp(-14.17\theta) \\ &- 21.5 \cdot exp(-23.19\theta) + 10.8 \cdot exp(-32.34\theta), \end{aligned}$$

    $\theta = \frac{c_{s,a}^*}{c_{s,a}^{max}}$, where $c_{s,a}^*$ denotes the solid phase surface concentration of Na^+ ions, and $c_{s,a}^{max}$ is the maximum solid phase Na^+ concentration.
  - $NaNi_{1/3}Co_{1/3}Mn_{1/3}O_2$ (fit to discharge curve in Ref. [113]):

$$\begin{aligned} U = &-0.022893 \cdot \left(\frac{\theta - 0.72957}{0.14747}\right)^5 - 0.051731 \cdot \left(\frac{\theta - 0.72957}{0.14747}\right)^4 \\ &+ 0.087786 \cdot \left(\frac{\theta - 0.72957}{0.14747}\right)^3 + 0.23729 \cdot \left(\frac{\theta - 0.72957}{0.14747}\right)^2 \\ &- 0.5341 \cdot \left(\frac{\theta - 0.72957}{0.14747}\right) + 2.717, \end{aligned}$$

$\theta = \frac{c^*_{s,c}}{c^{max}_{s,c}}$, where $c^*_{s,c}$ denotes the solid phase surface concentration of Na^+ ions, and $c^{max}_{s,c}$ is the maximum solid phase Na^+ concentration.

- Numerical approximation used to model diffusion in the active material particles: *higher-order polynomial approximation* (see Ref. [34]).
- Balanced anode and cathode capacities are assumed, and the loss of lithium/sodium due to SEI formation is assumed to be 10% (therefore, $c^{init}_{s,a} = 0.90\, c^{max}_{s,a}$).

TABLE A2: PSPA/PCR model parameters. Specified values indicate typical parameter ranges.

Parameter	Typical range	Units	Description
EoL_{cyc}^{80}	$6{,}000 - 25{,}000$	cycles	Number of equivalent cycles (N^{ref}) under reference conditions ($\delta_{ref} := 80\%$) until the battery pack reaches 80% SoH.
EoL_{cal}^{80}	$15 - 20$	yr	Number of years until the battery pack reaches 80% SoH.
SoH_{EoL}	$0.7 - 0.8$	$[-]$	SoH of the battery pack at the end of its lifetime.
SoH_{bat}	$\in [SoH_{EoL}, 1]$	$[-]$	Current state of health of the battery pack.
EoL_{cyc}		cycles	Cycle lifetime: number of equivalent cycles (N^{ref}) under reference conditions ($\delta_{ref} := 80\%$) until the battery pack reaches the end of its lifetime.
EoL_{cal}		yr	Calendar lifetime: number of years until the battery pack reaches the end of its lifetime.
EoL_{bat}		yr	Battery lifetime: number of years until the battery pack reaches the end of its lifetime. In the PSPA and PCR models, the battery pack lifetime is defined as the number of years until either the cycle (EoL_{cyc}) or the calendar (EoL_{cal}) lifetime is reached.
L_{iv}	15	yr	Lifetime of AC/DC power inverters.
δ	$\in [0,1]$	$[-]$	Depth of discharge (DoD).
N^{ref}		cycles	Number of equivalent cycles under reference conditions ($\delta_{ref} := 80\%$).
C_{bat}		MWh	Energy capacity of the new battery pack.
r_{bat}		MW/MWh	Power rating: maximum charge and discharge rate of the battery system.
$\eta^{bat,0}$	$0.95 - 0.97$	$[-]$	One-way energy efficiency of the new battery pack.
η^{bat}		$[-]$	Current one-way energy efficiency of the battery pack.
η^{iv}	0.97	$[-]$	One-way energy efficiency of power units (AC/DC power inverters and transformers).
η^{tot}		$[-]$	One-way energy efficiency of the (grid-connected) battery system. $\eta^{tot} = \eta^{bat}\,\eta^{iv}$.
W	$\in [1,2]$	$[-]$	Wöhler coefficient.
c_{sys}		EUR_{2019}	Battery system investment costs.
c_{pack}		EUR_{2019}/MWh	Battery pack investment costs.
c_{power}	243,000	EUR_{2019}/MW	Power unit investment costs (including the energy management system, thermal management system, cooling system, AC/DC power inverters, and transformers). The parameter value was selected based on Ref. [7].
c_{iv}	70,000	USD_{2019}/MW	AC/DC inverter replacement costs. Note that equal lifetimes are assumed for the battery pack and all components of the power unit except for AC/DC inverters. The inverters must be replaced if the battery pack lifetime exceeds the inverter lifetime. The parameter value was selected based on Ref. [166].
$c_{O\&M}$	$0.02\,c_{sys}$	EUR/yr	Yearly O&M costs in relative units of the battery system investment costs. The parameter value was selected based on Ref. [141].

r_d	4	$\%/yr$	Yearly discount rate.
$r_{ex_{EUR}}$	1.10	$[-]$	Currency exchange rate CHF/EUR (year 2019).
$r_{ex_{USD}}$	1.00	$[-]$	Currency exchange rate CHF/USD (year 2019).

TABLE A3: PSPA model parameters. Specified values indicate typical parameter ranges.

Parameter	Value	Units	Description
τ	$0.25 - 1.00$	h	Time step length.
T	$24 - 288$	$[-]$	Number of time steps in a dispatch period.
$\mathbf{L_i}$		MW	Load time series for dispatch period of type i. Vector of length T.
$\mathbf{p_i}$		EUR/MWh	Price time series for dispatch period of type i. Vector of length T.
P_{peak}^{month}		CHF/MW	Monthly peak power costs (power averaged over time period of length τ).
$N_{m,i}$		$[-]$	Number of dispatch periods of type i in month m.
L_l^{max}		MW	Maximum monthly peak load. A finite set of values L_l^{max}, $l \in \mathcal{L} = \{1,2,\ldots,L\}$, is provided as input and the PSPA model determines the optimal value L_l^{max} for each month.
a_k		$EUR/cycle$	Costs of battery degradation. A finite set of values a_k, $k \in \mathcal{K} = \{1,2,\ldots,K\}$, is provided as input to the PSPA model.
$\mathbf{P}^{ch}$		MW	Battery charge power. Decision variable vector of length T.
$\mathbf{P}^{dis}$		MW	Battery discharge power. Decision variable vector of length T.
SoC^{init}	0.5	$[-]$	Battery state of charge level at the beginning of a dispatch period ($t = 0$).
SoC^{end}	0.5	$[-]$	Battery state of charge level at the end of a dispatch period ($t = T$).
$\mathbf{SoC}$		$[-]$	Battery state of charge time series for a dispatch period. Vector of length $T + 1$ (including $SoC_{t=0}$ and $SoC_{t=T}$).

TABLE A4: PCR model parameters. Specified values indicate typical parameter ranges.

Parameter	Typical value	Units	Description
τ	1	s	Time step length.
τ_{WP}		s	Contract duration for scheduled power exchanges. τ_{WP} is a parameter of the SoC control strategy.
τ_{MA}		s	Duration of the averaging period to compute the working point. τ_{MA} is a parameter of the SoC control strategy.
τ_{LT}		s	Lead time (i.e., time lag) between power exchange scheduling and physical delivery. τ_{LT} is a parameter of the SoC control strategy.
τ^{Res}		s	Additional energy capacity that must be kept for PCR provision. τ^{Res} is defined by the transmission system operator (TSO).
P_t^{Ext}		MW/MW	Power exchanged between the battery system and the electricity grid per MW of offered PCR capacity. A positive sign indicates battery charging and a negative sign battery discharging.
P_t^{WP}		MW/MW	*Actual* working point of the battery. P_t^{WP} corresponds to scheduled power exchanges in the electricity market (MW per MW of offered PCR capacity).
$P_t^{WP_{ant}}$		MW/MW	*Anticipated* working point of the battery.
$P_t^{WP_{diff}}$		MW/MW	Difference between the *anticipated* and *actual* working point.
P_t^{PCR}	$\in [-1,+1]$	MW/MW	Control signal (MW per MW of offered PCR capacity). A positive sign denotes down-regulation of the grid frequency and a negative sign denotes up-regulation.
P_t^{Loss}		MW/MW	Power losses of the battery system (per MW of offered PCR capacity).
$\mathcal{C}^{\mathcal{PCR}}$		MW	Set of tradable PCR capacities.
C_{theor}^{PCR}		MW	Theoretical PCR capacity defined as the highest capacity $C^{PCR} \in \mathcal{C}^{\mathcal{PCR}}$ that is compatible with battery SoC constraints at all times.
$C_{offered}^{PCR}$		MW	Offered PCR capacity.
$\mathbf{f}$		Hz	Historical time series of the grid frequency. Vector of length T.
T		$[-]$	Length of the historical grid frequency time series.
$\mathbf{f}^p$		Hz	Prequalification time series of the grid frequency as defined by Swissgrid's prequalification criteria. Vector of length T_p.
T_p		$[-]$	Length of the prequalification time series of the grid frequency.
f^{nom}	50	Hz	Nominal grid frequency.
SoC^{init}	0.5	$[-]$	Battery state of charge level at $t = 0$.
$\mathbf{SoC}$		$[-]$	Battery state of charge time series. Vector of length $T+1$ (including $SoC_{t=0}$ and $SoC_{t=T}$).
$\overline{\pi}^{PCR}$		$[EUR/(MW \cdot yr)]$	Average remuneration for PCR provision.
π_t^{WP}		$[EUR/MWh]$	Electricity price on the intraday electricity market.

A.2 LIST OF ABBREVIATIONS

BMS	Battery management system
DoD	Depth of discharge
DP	Dynamic programming
FDM	Finite difference method
FR	Frequency regulation
FVM	Finite volume method
GHG	Greenhouse gas
LCA	Life cycle assessment
LFP	Lithium iron phosphate
LIB	Lithium-ion battery
LP	Linear programming
MILP	Mixed-integer linear programming
MINLP	Mixed-integer nonlinear programming
NIB	Sodium-ion battery
NLP	Nonlinear programming
NMC	Nickel manganese cobalt oxide
ODE	Ordinary differential equation
O&M	Operation and maintenance [costs]
PA	Price arbitrage [business]
PCR	Primary control reserves
PDE	Partial differential equation
PS	Peak shaving
PSPA	[(Combined) provision of] peak shaving and price arbitrage
PV	Photovoltaics
P2D model	Pseudo-two-dimensional [battery cell] model
SEI	Solid electrolyte interphase
SLSQP	Sequential least squares programming
SoC	State of charge
SoH	State of health
TSO	Transmission system operator

BIBLIOGRAPHY

[1] M. Allen, O. Dube, W. Solecki, F. Aragón-Durand, W. Cramer, S. Humphreys, M. Kainuma, J. Kala, N. Mahowald, Y. Mulugetta, R. Perez, M. Wairiu, and K. Zickfeld, "An IPCC special report on the impacts of global warming of 1.5°C above pre-industrial levels and related global greenhouse gas emission pathways, in the context of strengthening the global response to the threat of climate change, sustainable development", Tech. Rep., 2018.

[2] C. F. Schleussner, J. Rogelj, M. Schaeffer, T. Lissner, R. Licker, E. M. Fischer, R. Knutti, A. Levermann, K. Frieler, and W. Hare, "Science and policy characteristics of the Paris agreement temperature goal", *Nature Climate Change*, vol. 6, no. 9, pp. 827–835, 2016. DOI: 10.1038/nclimate3096.

[3] M. Aneke and M. Wang, "Energy storage technologies and real life applications – a state of the art review", *Applied Energy*, vol. 179, pp. 350–377, 2016. DOI: 10.1016/j.apenergy.2016.06.097.

[4] H. C. Hesse, M. Schimpe, D. Kucevic, and A. Jossen, "Lithium-ion battery storage for the grid - a review of stationary battery storage system design tailored for applications in modern power grids", *Energies*, vol. 10, no. 12, pp. 1–42, 2017. DOI: 10.3390/en10122107.

[5] M. Li, J. Lu, Z. Chen, and K. Amine, "30 years of lithium-ion batteries", *Advanced Materials*, vol. 30, no. 33, 2018. DOI: 10.1002/adma.201800561.

[6] *Allied market research, lithium-ion battery market outlook, https://www.alliedmarketresearch.com/lithium-ion-battery-market, Accessed: July 09, 2020*.

[7] T. S. Schmidt, M. Beuse, X. Zhang, B. Steffen, S. F. Schneider, A. Pena-Bello, C. Bauer, and D. Parra, "Additional emissions and cost from storing electricity in stationary battery systems", *Environmental Science and Technology*, vol. 53, no. 7, pp. 3379–3390, 2019. DOI: 10.1021/acs.est.8b05313.

[8] T. S. Schmidt, B. Battke, D. Grosspietsch, and V. H. Hoffmann, "Do deployment policies pick technologies by (not) picking applications?—a simulation of investment decisions in technologies with multiple applications", *Research Policy*, vol. 45, no. 10, pp. 1965–1983, 2016. DOI: 10.1016/j.respol.2016.07.001.

[9] A. Malhotra, B. Battke, M. Beuse, A. Stephan, and T. Schmidt, "Use cases for stationary battery technologies: a review of the literature and existing projects", *Renewable and Sustainable Energy Reviews*, vol. 56, pp. 705–721, 2016. DOI: 10.1016/j.rser.2015.11.085.

[10] D. M. Rosewater, D. A. Copp, T. A. Nguyen, R. H. Byrne, and S. Santoso, "Battery energy storage models for optimal control", *IEEE Access*, vol. 7, pp. 178 357–178 391, 2019. DOI: 10.1109/ACCESS.2019.2957698.

[11] B. Xu, A. Oudalov, A. Ulbig, G. Andersson, and D. S. Kirschen, "Modeling of lithium-ion battery degradation for cell life assessment", *IEEE Transactions on Smart Grid*, vol. 9, no. 2, pp. 1131–1140, 2018. DOI: 10.1109/TSG.2016.2578950.

[12] J. F. Peters and M. Weil, "Providing a common base for life cycle assessments of Li-ion batteries", *Journal of Cleaner Production*, vol. 171, pp. 704–713, 2018. DOI: 10.1016/j.jclepro.2017.10.016.

[13] C. Vaalma, D. Buchholz, M. Weil, and S. Passerini, "A cost and resource analysis of sodium-ion batteries", *Nature Reviews Materials*, vol. 3, no. 18013, pp. 1–11, 2018. DOI: 10.1038/natrevmats.2018.13.

[14] I. Tsiropoulos, D. Tarvydas, and N. Lebedeva, "Li-ion batteries for mobility and stationary storage applications.", JRC Science for policy report, Tech. Rep., 2018. DOI: 10.2760/87175.

[15] J. Betz, G. Bieker, P. Meister, T. Placke, M. Winter, and R. Schmuch, "Theoretical versus practical energy: a plea for more transparency in the energy calculation of different rechargeable battery systems", *Advanced Energy Materials*, vol. 9, no. 6, p. 1 803 170, 2019. DOI: 10.1002/aenm.201803170.

[16] J. M. Reniers, G. Mulder, S. Ober-Blöbaum, and D. A. Howey, "Improving optimal control of grid-connected lithium-ion batteries through more accurate battery and degradation modelling", *Journal of Power Sources*, vol. 379, pp. 91–102, 2018. DOI: 10.1016/j.jpowsour.2018.01.004.

[17] N. Chawla, N. Bharti, and S. Singh, "Recent advances in non-flammable electrolytes for safer lithium-ion batteries", *Batteries*, vol. 5, no. 19, pp. 1–25, 2019. DOI: 10.3390/batteries5010019.

[18] U. Krewer, F. Röder, E. Harinath, R. D. Braatz, B. Bedürftig, and R. Findeisen, "Review — dynamic models of Li-ion batteries for diagnosis and operation: a review and perspective", *Journal of the Electrochemical Society*, vol. 165, no. 16, A3656–A3673, 2018. DOI: 10.1149/2.1061814jes.

[19] G. Patry, A. Romagny, S. Martinet, and D. Froelich, "Cost modeling of lithium-ion battery cells for automotive applications", *Energy Science & Engineering*, vol. 3, no. 1, pp. 71–82, 2015. DOI: 10.1002/ese3.47.

[20] L. A. W. Ellingsen, G. Majeau-Bettez, B. Singh, A. K. Srivastava, L. O. Valøen, and A. H. Strømman, "Life cycle assessment of a lithium-ion battery vehicle pack", *Journal of Industrial Ecology*, vol. 18, no. 1, pp. 113–124, 2014. DOI: 10.1111/jiec.12072.

[21] M. Armand, P. Axmann, D. Bresser, M. Copley, K. Edström, C. Ekberg, D. Guyomard, B. Lestriez, P. Novák, M. Petranikova, W. Porcher, S. Trabesinger, M. Wohlfahrt-Mehrens, and H. Zhang, "Lithium-ion batteries - current state of the art and anticipated developments", *Journal of Power Sources*, vol. 479, p. 228 708, 2020. DOI: 10.1016/j.jpowsour.2020.228708.

[22] *Homer energy, https://www.homerenergy.com/, Accessed: August 21, 2020*.

[23] C.A.R.M.E.N., "Marktübersicht Batteriespeicher 2019", Centrales Agrar-Rohstoff Marketing- und Energie-Netzwerk, Schulgasse 18, 94315 Straubing, Germany, Tech. Rep., 2020, www.carmen-ev.de, Accessed: December 02, 2020.

[24] M. Torchio, "Model predictive control strategies for advanced battery management systems", PhD thesis, University of Pavia, 2017.

[25] V. Ramadesigan, P. W. C. Northrop, S. De, S. Santhanagopalan, R. D. Braatz, and V. R. Subramanian, "Modeling and simulation of lithium-ion batteries from a systems engineering perspective", *Journal of the Electrochemical Society*, vol. 159, no. 3, R31–R45, 2012. DOI: 10.1149/2.018203jes.

[26] A. M. Bizeray, J. H. Kim, S. R. Duncan, and D. A. Howey, "Identifiability and parameter estimation of the single particle lithium-ion battery model", *IEEE Transactions on Control Systems Technology*, vol. 27, no. 5, pp. 1862–1877, 2019. DOI: 10.1109/TCST.2018.2838097.

[27] B. Wu, S. Han, K. G. Shin, and W. Lu, "Application of artificial neural networks in design of lithium-ion batteries", *Journal of Power Sources*, vol. 395, pp. 128–136, 2018. DOI: 10.1016/j.jpowsour.2018.05.040.

[28] S. B. Lee, N. Dawson-Elli, K. Mitra, V. R. Subramanian, and M. Pathak, "Data science approaches for electrochemical engineers: an introduction through surrogate model development for lithium-ion batteries", *Journal of The Electrochemical Society*, vol. 165, no. 2, A1–A15, 2018. DOI: 10.1149/2.1391714jes.

[29] K. A. Severson, P. M. Attia, N. Jin, N. Perkins, B. Jiang, Z. Yang, M. H. Chen, M. Aykol, P. K. Herring, D. Fraggedakis, M. Z. Bazant, S. J. Harris, W. C. Chueh, and R. D. Braatz, "Data-driven prediction of battery cycle life before capacity degradation", *Nature Energy*, vol. 4, no. 5, pp. 383–391, 2019. DOI: 10.1038/s41560-019-0356-8.

[30] Y. Li, K. Liu, A. M. Foley, A. Zülke, M. Berecibar, E. Nanini-Maury, J. Van Mierlo, and H. E. Hoster, "Data-driven health estimation and lifetime prediction of lithium-ion batteries: a review", *Renewable and Sustainable Energy Reviews*, vol. 113, 2019. DOI: 10.1016/j.rser.2019.109254.

[31] R. De Levie, "On porous electrodes in electrolyte solutions", *Electrochimica Acta*, vol. 8, pp. 751–780, 1963.

[32] J. Newman and W. Tiedeman, "Porouse-electrode theory with battery applications", *AIChE Journal*, vol. 21, no. 1, pp. 25–41, 1975. DOI: 10.1002/aic.690210103.

[33] M. Doyle, "Modeling of galvanostatic charge and discharge of the lithium/polymer/ insertion cell", *Journal of The Electrochemical Society*, vol. 140, no. 6, p. 1526, 1993. DOI: 10.1149/1.2221597.

[34] M. Torchio, L. Magni, R. B. Gopaluni, R. D. Braatz, and D. M. Raimondo, "Lionsimba: a Matlab framework based on a finite volume model suitable for Li-ion battery design, simulation, and control", *Journal of The Electrochemical Society*, vol. 163, no. 7, A1192–A1205, 2016. DOI: 10.1149/2.0291607jes.

[35] T. R. Ferguson and M. Z. Bazant, "Nonequilibrium thermodynamics of porous electrodes", *Journal of The Electrochemical Society*, vol. 159, no. 12, A1967–A1985, 2012. DOI: 10.1149/2.048212jes.

[36] D. W. Chung, M. Ebner, D. R. Ely, V. Wood, and R. Edwin García, "Validity of the Bruggeman relation for porous electrodes", *Modelling and Simulation in Materials Science and Engineering*, vol. 21, no. 7, pp. 1–16, 2013. DOI: 10.1088/0965-0393/21/7/074009.

[37] J. Landesfeind, J. Hattendorff, A. Ehrl, W. A. Wall, and H. A. Gasteiger, "Tortuosity determination of battery electrodes and separators by impedance spectroscopy", *Journal of The Electrochemical Society*, vol. 163, no. 7, A1373–A1387, 2016. DOI: 10.1149/2.1141607jes.

[38] A. Ehrl, J. Landesfeind, W. A. Wall, and H. A. Gasteiger, "Determination of transport parameters in liquid binary lithium ion battery electrolytes. I. diffusion coefficient", *Journal of The Electrochemical Society*, vol. 164, no. 4, A826–836, 2017. DOI: 10.1149/2.1131704jes.

[39] A. J. Bard and L. R. Faulkner, *Electrochemical methods: fundamentals and applications, 2nd eddition*. WILEY-VCH Verlag, 2000, pp. 148–149.

[40] Y. Ma, M. Yin, Z. Ying, and H. Chen, "Establishment and simulation of an electrode averaged model for a lithium-ion battery based on kinetic reactions", *RSC Adv.*, vol. 6, no. 30, pp. 25 435–25 443, 2016. DOI: 10.1039/C5RA27556C.

[41] D. Howey, S. Duncan, and A. Bizeray, "Advanced battery management systems using fast electrochemical modelling", *Hybrid and Electric Vehicles Conference 2013 (HEVC 2013)*, 2013. DOI: 10.1049/cp.2013.1890.

[42] G. Lenze, F. Röder, H. Bockholt, W. Haselrieder, A. Kwade, and U. Krewer, "Simulation-supported analysis of calendering impacts on the performance of lithium-ion-batteries", *Journal of The Electrochemical Society*, vol. 164, no. 6, A1223–A1233, 2017. DOI: 10.1149/2.1141706jes.

[43] P. Verma, P. Maire, and P. Novák, "A review of the features and analyses of the solid electrolyte interphase in Li-ion batteries", *Electrochimica Acta*, vol. 55, no. 22, pp. 6332–6341, 2010. DOI: 10.1016/j.electacta.2010.05.072.

[44] M. Woody, M. Arbabzadeh, G. M. Lewis, G. A. Keoleian, and A. Stefanopoulou, "Strategies to limit degradation and maximize Li-ion battery service lifetime - critical review and guidance for stakeholders", *Journal of Energy Storage*, vol. 28, p. 101 231, 2020. DOI: 10.1016/j.est.2020.101231.

[45] S. J. An, J. Li, C. Daniel, D. Mohanty, S. Nagpure, and D. L. Wood, "The state of understanding of the lithium-ion-battery graphite solid electrolyte interphase (SEI) and its relationship to formation cycling", *Carbon*, vol. 105, pp. 52–76, 2016. DOI: 10.1016/j.carbon.2016.04.008.

[46] M. Dubarry, N. Qin, and P. Brooker, "Calendar aging of commercial Li-ion cells of different chemistries – a review", *Current Opinion in Electrochemistry*, vol. 9, pp. 106–113, 2018. DOI: 10.1016/j.coelec.2018.05.023.

[47] J. Schmalstieg, S. Käbitz, M. Ecker, and D. U. Sauer, "A holistic aging model for Li(NiMnCo)O_2 based 18650 lithium-ion batteries", *Journal of Power Sources*, vol. 257, pp. 325–334, 2014. DOI: 10.1016/j.jpowsour.2014.02.012.

[48] Y. X. Lin, Z. Liu, K. Leung, L. Q. Chen, P. Lu, and Y. Qi, "Connecting the irreversible capacity loss in Li-ion batteries with the electronic insulating properties of solid electrolyte interphase (SEI) components", *Journal of Power Sources*, vol. 309, pp. 221–230, 2016. DOI: 10.1016/j.jpowsour.2016.01.078.

[49] S. Schweidler, L. De Biasi, A. Schiele, P. Hartmann, T. Brezesinski, and J. Janek, "Volume changes of graphite anodes revisited: a combined operando X-ray diffraction and in situ pressure analysis study", *Journal of Physical Chemistry C*, vol. 122, no. 16, pp. 8829–8835, 2018. DOI: 10.1021/acs.jpcc.8b01873.

[50] J. Vetter, P. Novák, M. R. Wagner, C. Veit, K. C. Möller, J. O. Besenhard, M. Winter, M. Wohlfahrt-Mehrens, C. Vogler, and A. Hammouche, "Ageing mechanisms in lithium-ion batteries", *Journal of Power Sources*, vol. 147, pp. 269–281, 2005. DOI: 10.1016/j.jpowsour.2005.01.006.

[51] D. Galatro, C. D. Silva, D. A. Romero, O. Trescases, and C. H. Amon, "Challenges in data-based degradation models for lithium-ion batteries", *International Journal of Energy Research*, pp. 3954–3975, 2020. DOI: 10.1002/er.5196.

[52] R. Sahore, D. C. O'Hanlon, A. Tornheim, C.-W. Lee, J. C. Garcia, H. Iddir, M. Balasubramanian, and I. Bloom, "Revisiting the mechanism behind transition-metal dissolution from delithiated $LiNi_xMn_yCo_zO_2$ (NMC) cathodes", *Journal of The Electrochemical Society*, vol. 167, no. 2, p. 020 513, 2020. DOI: 10.1149/1945-7111/ab6826.

[53] M. Ecker, N. Nieto, S. Käbitz, J. Schmalstieg, H. Blanke, A. Warnecke, and D. U. Sauer, "Calendar and cycle life study of Li(NiMnCo)O_2 based 18650 lithium-ion batteries", *Journal of Power Sources*, vol. 248, pp. 839–851, 2014. DOI: 10.1016/j.jpowsour.2013.09.143.

[54] K. Edström, T. Gustafsson, and J. O. Thomas, "The cathode-electrolyte interface in the Li-ion battery", *Electrochimica Acta*, vol. 50, pp. 397–403, 2004. DOI: 10.1016/j.electacta.2004.03.049.

[55] R. Hausbrand, G. Cherkashinin, H. Ehrenberg, M. Gröting, K. Albe, C. Hess, and W. Jaegermann, "Fundamental degradation mechanisms of layered oxide Li-ion battery cathode materials: methodology, insights and novel approaches", *Materials Science and Engineering B: Solid-State Materials for Advanced Technology*, vol. 192, pp. 3–25, 2015. DOI: 10.1016/j.mseb.2014.11.014.

[56] Y. Li, M. Vilathgamuwa, S. S. Choi, T. W. Farrell, N. T. Tran, and J. Teague, "Development of a degradation-conscious physics-based lithium-ion battery model for use in power system planning studies", *Applied Energy*, vol. 248, pp. 512–525, 2019. DOI: 10.1016/j.apenergy.2019.04.143.

[57] X. Jin, A. Vora, V. Hoshing, T. Saha, G. Shaver, O. Wasynczuk, and S. Varigonda, "Applicability of available Li-ion battery degradation models for system and control algorithm design", *Control Engineering Practice*, vol. 71, pp. 1–9, 2018. DOI: 10.1016/j.conengprac.2017.10.002.

[58] B. Xu, J. Zhao, T. Zheng, E. Litvinov, and D. S. Kirschen, "Factoring the cycle aging cost of batteries participating in electricity markets", *IEEE Transactions on Power Systems*, vol. 33, no. 2, pp. 2248–2259, 2018. DOI: 10.1109/TPWRS.2017.2733339.

[59] I. Baghdadi, O. Briat, J. Y. Delétage, P. Gyan, and J. M. Vinassa, "Lithium battery aging model based on Dakin's degradation approach", *Journal of Power Sources*, vol. 325, pp. 273–285, 2016. DOI: 10.1016/j.jpowsour.2016.06.036.

[60] J. Wang, J. Purewal, P. Liu, J. Hicks-Garner, S. Soukazian, E. Sherman, A. Sorenson, L. Vu, H. Tataria, and M. W. Verbrugge, "Degradation of lithium ion batteries employing graphite negatives and nickel-cobalt-manganese oxide + spinel manganese oxide positives: part 1, aging mechanisms and life estimation", *Journal of Power Sources*, vol. 269, pp. 937–948, 2014. DOI: 10.1016/j.jpowsour.2014.07.030.

[61] T. Gewald, A. Candussio, L. Wildfeuer, D. Lehmkuhl, A. Hahn, and M. Lienkamp, "Accelerated aging characterization of lithium-ion cells: using sensitivity analysis to identify the stress factors relevant to cyclic aging", *Batteries*, vol. 6, no. 1, pp. 1–18, 2020. DOI: 10.3390/batteries6010006.

[62] H. C. Hesse, V. Kumtepeli, M. Schimpe, J. Reniers, D. A. Howey, A. Tripathi, Y. Wang, and A. Jossen, "Ageing and efficiency aware battery dispatch for arbitrage markets using mixed integer linear programming", *Energies*, vol. 12, no. 6, 2019. DOI: 10.3390/en12060999.

[63] B. Xu, "Batteries in electricity markets: economic planning and operations", PhD thesis, University of Washington, 2018.

[64] J. de Hoog, J. M. Timmermans, D. Ioan-Stroe, M. Swierczynski, J. Jaguemont, S. Goutam, N. Omar, J. Van Mierlo, and P. Van Den Bossche, "Combined cycling and calendar capacity fade modeling of a nickel-manganese-cobalt oxide cell with real-life profile validation", *Applied Energy*, vol. 200, pp. 47–61, 2017. DOI: 10.1016/j.apenergy.2017.05.018.

[65] S. Käbitz, J. B. Gerschler, M. Ecker, Y. Yurdagel, B. Emmermacher, D. André, T. Mitsch, and D. U. Sauer, "Cycle and calendar life study of a graphite/$LiNi_{1/3}Mn_{1/3}Co_{1/3}O_2$ Li-ion high energy system. Part A: full cell characterization", *Journal of Power Sources*, vol. 239, pp. 572–583, 2013. DOI: 10.1016/j.jpowsour.2013.03.045.

[66] J. Wang, P. Liu, J. Hicks-Garner, E. Sherman, S. Soukiazian, M. Verbrugge, H. Tataria, J. Musser, and P. Finamore, "Cycle-life model for graphite-$LiFePO_4$ cells", *Journal of Power Sources*, vol. 196, no. 8, pp. 3942–3948, 2011. DOI: 10.1016/j.jpowsour.2010.11.134.

[67] S. B. Peterson, J. Apt, and J. F. Whitacre, "Lithium-ion battery cell degradation resulting from realistic vehicle and vehicle-to-grid utilization", *Journal of Power Sources*, vol. 195, no. 8, pp. 2385–2392, 2010. DOI: 10.1016/j.jpowsour.2009.10.010.

[68] M. Naumann, F. Spingler, and A. Jossen, "Analysis and modeling of cycle aging of a commercial $LiFePO_4$/graphite cell", *Journal of Power Sources*, vol. 451, no. January, p. 227666, 2020. DOI: 10.1016/j.jpowsour.2019.227666.

[69] M. Petit, E. Prada, and V. Sauvant-Moynot, "Development of an empirical aging model for Li-ion batteries and application to assess the impact of vehicle-to-grid strategies on battery lifetime", *Applied Energy*, vol. 172, pp. 398–407, 2016. DOI: 10.1016/j.apenergy.2016.03.119.

[70] E. Sarasketa-Zabala, E. Martinez-Laserna, M. Berecibar, I. Gandiaga, L. M. Rodriguez-Martinez, and I. Villarreal, "Realistic lifetime prediction approach for Li-ion batteries", *Applied Energy*, vol. 162, pp. 839–852, 2016. DOI: 10.1016/j.apenergy.2015.10.115.

[71] M. Varini, P. E. Campana, and G. Lindbergh, "A semi-empirical, electrochemistry-based model for Li-ion battery performance prediction over lifetime", *Journal of Energy Storage*, vol. 25, p. 100819, 2019. DOI: 10.1016/j.est.2019.100819.

[72] G. He, Q. Chen, P. Moutis, S. Kar, and J. F. Whitacre, "An intertemporal decision framework for electrochemical energy storage management", *Nature Energy*, vol. 3, no. 5, pp. 404–412, 2018. DOI: 10.1038/s41560-018-0129-9.

[73] S. F. Schuster, T. Bach, E. Fleder, J. Müller, M. Brand, G. Sextl, and A. Jossen, "Nonlinear aging characteristics of lithium-ion cells under different operational conditions", *Journal of Energy Storage*, vol. 1, no. 1, pp. 44–53, 2015. DOI: 10.1016/j.est.2015.05.003.

[74] D. I. Stroe, M. Swierczynski, A. I. Stroe, R. Laerke, P. C. Kjaer, and R. Teodorescu, "Degradation behavior of lithium-ion batteries based on lifetime models and field measured frequency regulation mission profile", *IEEE Transactions on Industry Applications*, vol. 52, no. 6, pp. 5009–5018, 2016. DOI: 10.1109/TIA.2016.2597120.

[75] M. U. Hashmi, W. Labidi, A. Busic, S. E. Elayoubi, and T. Chahed, "Long-term revenue estimation for battery performing arbitrage and ancillary services", *2018 IEEE International Conference on Communications, Control, and Computing Technologies for Smart Grids, SmartGridComm 2018*, 2018. DOI: 10.1109/SmartGridComm.2018.8587562.

[76] M. Kazemi and H. Zareipour, "Long-term scheduling of battery storage systems in energy and regulation markets considering battery's lifespan", *IEEE Transactions on Smart Grid*, vol. 9, no. 6, pp. 6840–6849, 2018. DOI: 10.1109/TSG.2017.2724919.

[77] Y. Shi, B. Xu, Y. Tan, D. Kirschen, and B. Zhang, "Optimal battery control under cycle aging mechanisms in pay for performance settings", *IEEE Transactions on Automatic Control*, pp. 1–20, 2018. DOI: 10.1109/TAC.2018.2867507.

[78] S. D. Downing and D. F. Socie, "Simple Rainflow counting algorithms", *International Journal of Fatigue*, vol. 4, no. 1, pp. 31–40, 1982. DOI: 10.1016/0142-1123(82)90018-4.

[79] C. Amzallag, J. P. Gerey, J. L. Robert, and J. Bahuaud, "Standardization of the rainflow counting method for fatigue analysis", *International Journal of Fatigue*, vol. 16, no. 4, pp. 287–293, 1994. DOI: 10.1016/0142-1123(94)90343-3.

[80] I. Rychlik, "A new definition of the Rainflow cycle counting method", *International Journal of Fatigue*, vol. 9, no. 2, pp. 119–121, 1987. DOI: 10.1016/0142-1123(87)90054-5.

[81] Y. Shi, B. Xu, Y. Tan, and B. Zhang, "A convex cycle-based degradation model for battery energy storage planning and operation", *Proceedings of American Control Conference*, 2018.

[82] M. J. Alam and T. K. Saha, "Cycle-life degradation assessment of battery energy storage systems caused by solar PV variability", in *IEEE Power and Energy Society General Meeting*, IEEE, 2016, pp. 1–5. DOI: 10.1109/PESGM.2016.7741532.

[83] T. Dragičević, H. Pandžić, D. Škrlec, I. Kuzle, J. M. Guerrero, and D. S. Kirschen, "Capacity optimization of renewable energy sources and battery storage in an autonomous telecommunication facility", *IEEE Transactions on Sustainable Energy*, vol. 5, no. 4, pp. 1367–1378, 2014. DOI: 10.1109/TSTE.2014.2316480.

[84] V. Muenzel, J. de Hoog, M. Brazil, A. Vishwanath, and S. Kalyanaraman, "A multi-factor battery cycle life prediction methodology for optimal battery management", in *Proceedings of the 2015 ACM Sixth International Conference on Future Energy Systems*, 2015, pp. 57–66. DOI: 10.1145/2768510.2768532.

[85] M.-F. Ng, J. Zhao, Q. Yan, G. J. Conduit, and Z. W. Seh, "Predicting the state of charge and health of batteries using data-driven machine learning", *Nature Machine Intelligence*, vol. 2, no. 3, pp. 161–170, 2020. DOI: 10.1038/s42256-020-0156-7.

[86] Y. Zhang, Q. Tang, Y. Zhang, J. Wang, U. Stimming, and A. A. Lee, "Identifying degradation patterns of lithium ion batteries from impedance spectroscopy using machine learning", *Nature Communications*, vol. 11, no. 1, pp. 6–11, 2020. DOI: 10.1038/s41467-020-15235-7.

[87] X. Chen, L. Ye, Y. Wang, and X. Li, "Beyond expert-level performance prediction for rechargeable batteries by unsupervised machine learning", *Advanced Intelligent Systems*, vol. 1, no. 8, p. 1 900 102, 2019. DOI: 10.1002/aisy.201900102.

[88] P. Fermín-Cueto, E. McTurk, M. Allerhand, E. Medina-Lopez, M. F. Anjos, J. Sylvester, and G. dos Reis, "Identification and machine learning prediction of knee-point and knee-onset in capacity degradation curves of lithium-ion cells", *Energy and AI*, vol. 1, p. 100 006, 2020. DOI: 10.1016/j.egyai.2020.100006.

[89] S. F. Schneider, C. Bauer, P. Novák, and E. J. Berg, "A modeling framework to assess specific energy, costs and environmental impacts of Li-ion and Na-ion batteries", *Sustainable Energy & Fuels*, vol. 3, pp. 3061–3070, 2019. DOI: 10.1039/C9SE00427K.

[90] J. Tang, A. D. Dysart, and V. G. Pol, "Advancement in sodium-ion rechargeable batteries", *Current Opinion in Chemical Engineering*, vol. 9, pp. 34–41, 2015. DOI: 10.1016/j.coche.2015.08.007.

[91] J. Peters, D. Buchholz, S. Passerini, and M. Weil, "Life cycle assessment of sodium-ion batteries", *Energy Environ. Sci.*, vol. 9, no. 5, pp. 1744–1751, 2016. DOI: 10.1039/C6EE00640J.

[92] P. K. Nayak, L. Yang, W. Brehm, and P. Adelhelm, "From lithium-ion to sodium-ion batteries: advantages, challenges, and surprises", *Angewandte Chemie - International Edition*, vol. 57, no. 1, pp. 102–120, 2018. DOI: 10.1002/anie.201703772.

[93] C. Delmas, "Sodium and sodium-ion batteries: 50 years of research", *Advanced Energy Materials*, vol. 8, no. 17, pp. 1–9, 2018. DOI: 10.1002/aenm.201703137.

[94] P. Vanysek, *Electrochemical Series, CRC Handbook of Chemistry and Physics, 99th edition, Internet Version*. CRC Press/Taylor & Francis, Boca Raton, FL, 2018. DOI: 10.1002/0470862106.id263.

[95] A. Ponrouch, D. Monti, A. Boschin, B. Steen, P. Johansson, and M. R. Palacín, "Non-aqueous electrolytes for sodium-ion batteries", *J. Mater. Chem. A*, vol. 3, no. 1, pp. 22–42, 2015. DOI: 10.1039/C4TA04428B.

[96] T. R. Jow, S. A. Delp, J. L. Allen, J.-P. Jones, and M. C. Smart, "Factors limiting Li^+ charge transfer kinetics in Li-ion batteries", *Journal of the Electrochemical Society*, vol. 165, no. 2, pp. 361–367, 2018. DOI: 10.1149/2.1221802jes.

[97] V. A. Nikitina, S. S. Fedotov, S. Yu. Vassiliev, A. Sh. Samarin, N. R. Khasanova, and E. V. Antipov, "Transport and kinetic aspects of alkali metal ions intercalation into $AVPO_4F$ framework", *Journal of The Electrochemical Society*, vol. 164, no. 1, A6373–A6380, 2017. DOI: 10.1149/2.0531701jes.

[98] K. L. Browning, R. L. Sacci, and G. M. Veith, "Energetics of Na^+ transport through the electrode/cathode interface in single solvent electrolytes", *Journal of The Electrochemical Society*, vol. 164, no. 4, A580–A586, 2017. DOI: 10.1149/2.0311704jes.

[99] P. A. Nelson, S. Ahmed, K. G. Gallagher, and D. W. Dees, "Modeling the performance and cost of lithium-ion batteries for electric-drive vehicles, third edition", Tech. Rep., Argonne National Lab., Argonne, IL (United States), 2019. DOI: 10.2172/1503280.

[100] J. Rempel, B. Barnett, and Y. Hyung, *PHEV battery cost assessment*, 2013, https://www.energy.gov/sites/prod/files/2014/03/f13/es001_barnett_2013_0.pdf, Accessed: December 02, 2020.

[101] E. J. Berg, C. Villevieille, D. Streich, S. Trabesinger, and P. Novák, "Rechargeable batteries: grasping for the limits of chemistry", *Journal of The Electrochemical Society*, vol. 162, no. 14, A2468–A2475, 2015. DOI: 10.1149/2.0081514jes.

[102] N. Xue, W. Du, T. A. Greszler, W. Shyy, and J. R. Martins, "Design of a lithium-ion battery pack for PHEV using a hybrid optimization method", *Applied Energy*, vol. 115, pp. 591–602, 2014. DOI: 10.1016/j.apenergy.2013.10.044.

[103] R. Petri, T. Giebel, B. Zhang, J. H. Schünemann, and C. Herrmann, "Material cost model for innovative Li-ion battery cells in electric vehicle applications", *International Journal of Precision Engineering and Manufacturing - Green Technology*, vol. 2, no. 3, pp. 263–268, 2015. DOI: 10.1007/s40684-015-0031-x.

[104] S. P. Ong, V. L. Chevrier, G. Hautier, A. Jain, C. Moore, S. Kim, X. Ma, and G. Ceder, "Voltage, stability and diffusion barrier differences between sodium-ion and lithium-ion intercalation materials", *Energy and Environmental Science*, vol. 4, no. 9, pp. 3680–3688, 2011. DOI: 10.1039/c1ee01782a.

[105] G. Berckmans, M. Messagie, J. Smekens, N. Omar, L. Vanhaverbeke, and J. V. Mierlo, "Cost projection of state of the art lithium-ion batteries for electric vehicles up to 2030", *Energies*, vol. 10, no. 9, p. 1314, 2017. DOI: 10.3390/en10091314.

[106] N. Xue, W. Du, A. Gupta, W. Shyy, A. M. Sastry, and J. R. R. A. Martins, "Optimization of a single lithium-ion battery cell with a gradient-based algorithm", *Journal of the Electrochemical Society*, vol. 160, no. 8, A1071–A1078, 2013. DOI: 10.1149/2.036308jes.

[107] Y. Dai and V. Srinivasan, "On graded electrode porosity as a design tool for improving the energy density of batteries", *Journal of The Electrochemical Society*, vol. 163, no. 3, A406–A416, 2016. DOI: 10.1149/2.0301603jes.

[108] *Matlab fmincon optimization solver https://www.mathworks.com/help/optim/ug/fmincon.html, Accessed: December 02, 2020.*

[109] *Matlab Particle Swarm optimization solver https://www.mathworks.com/help/gads/particle-swarm.html, Accessed: September 19, 2020.*

[110] K. Wang, Y. Jin, S. Sun, Y. Huang, J. Peng, J. Luo, Q. Zhang, Y. Qiu, C. Fang, and J. Han, "Low-cost and high-performance hard carbon anode materials for sodium-ion batteries", *ACS Omega*, vol. 2, no. 4, pp. 1687–1695, 2017. DOI: 10.1021/acsomega.7b00259.

[111] D. W. McCall and D. C. Douglass, "The effect of ions on the self-diffusion of water. I. Concentration dependence", *Journal of Physical Chemistry*, vol. 69, no. 6, pp. 2001–2011, 1965. DOI: 10.1021/j100890a034.

[112] E. R. Logan, E. M. Tonita, K. L. Gering, J. Li, X. Ma, L. Y. Beaulieu, and J. R. Dahn, "A study of the physical properties of Li-ion battery electrolytes containing esters", *Journal of The Electrochemical Society*, vol. 165, no. 2, A21–A30, 2018. DOI: 10.1149/2.0271802jes.

[113] M. Sathiya, K. Hemalatha, K. Ramesha, J. M. Tarascon, and A. S. Prakash, "Synthesis, structure, and electrochemical properties of the layered sodium insertion cathode material: $NaNi_{1/3}Mn_{1/3}Co_{1/3}O_2$", *Chemistry of Materials*, vol. 24, no. 10, pp. 1846–1853, 2012. DOI: 10.1021/cm300466b.

[114] C. Mutel, "Brightway: An open source framework for life cycle assessment", *The Journal of Open Source Software*, vol. 2, no. 12, p. 236, 2017. DOI: 10.21105/joss.00236.

[115] G. Wernet, C. Bauer, B. Steubing, J. Reinhard, E. Moreno-Ruiz, and B. Weidema, "The ecoinvent database version 3 (part I): overview and methodology", *International Journal of Life Cycle Assessment*, vol. 21, no. 9, pp. 1218–1230, 2016. DOI: 10.1007/s11367-016-1087-8.

[116] B. Cox, C. Bauer, A. Mendoza Beltran, D. P. van Vuuren, and C. L. Mutel, "Life cycle environmental and cost comparison of current and future passenger cars under different energy scenarios", *Applied Energy*, vol. 269, p. 115 021, 2020. DOI: 10.1016/j.apenergy.2020.115021.

[117] Tech. Rep., U.S. Geological Survey, Mineral commodity summaries 2018: U.S. Department of the Interior, 2018. DOI: 10.3133/70194932.

[118] E. J. Berg and S. Trabesinger, "Viability of polysulfide-retaining barriers in Li-S battery", *Journal of The Electrochemical Society*, vol. 165, no. 1, A5001–A5005, 2018. DOI: 10.1149/2.0021801jes.

[119] R. Schmuch, R. Wagner, G. Hörpel, T. Placke, and M. Winter, "Performance and cost of materials for lithium-based rechargeable automotive batteries", *Nature Energy*, vol. 3, no. 4, pp. 267–278, 2018. DOI: 10.1038/s41560-018-0107-2.

[120] B. Rajabloo, A. Jokar, M. Désilets, and M. Lacroix, "An inverse method for estimating the electrochemical parameters of lithium-ion batteries", *Journal of The Electrochemical Society*, vol. 164, no. 2, A99–A105, 2017. DOI: 10.1149/2.0221702jes.

[121] C. Pillot, *Avicenne energy, current status and future trends of the global Li-ion battery market*, 2018, http://www.charles-hatchett.com/public/images/documents/2018/dr_christophe_pillot_current_status_and_future_trends_of_the_global_li-ion_battery_market.pdf, Accessed: December 02, 2020.

[122] R. E. Ciez and J. F. Whitacre, "The cost of lithium is unlikely to upend the price of Li-ion storage systems", *Journal of Power Sources*, vol. 320, pp. 310–313, 2016. DOI: 10.1016/j.jpowsour.2016.04.073.

[123] S. F. Schneider, P. Novák, and T. Kober, "Rechargeable batteries for simultaneous demand peak shaving and price arbitrage business", *IEEE Transactions on Sustainable Energy*, vol. 12, no. 1, pp. 148–157, January 2021. DOI: 10.1109/TSTE.2020.2988205.

[124] F. Braeuer, J. Rominger, R. McKenna, and W. Fichtner, "Battery storage systems: An economic model-based analysis of parallel revenue streams and general implications for industry", *Applied Energy*, vol. 239, pp. 1424–1440, 2019. DOI: 10.1016/j.apenergy.2019.01.050.

[125] C. Bordin, H. O. Anuta, A. Crossland, I. L. Gutierrez, C. J. Dent, and D. Vigo, "A linear programming approach for battery degradation analysis and optimization in offgrid power systems with solar energy integration", *Renewable Energy*, vol. 101, pp. 417–430, 2017. DOI: 10.1016/j.renene.2016.08.066.

[126] Y. Shi, B. Xu, D. Wang, and B. Zhang, "Using battery storage for peak shaving and frequency regulation: joint optimization for superlinear gains", *IEEE Transactions on Power Systems*, vol. 33, no. 3, pp. 2882–2894, 2018. DOI: 10.1109/TPWRS.2017.2749512.

[127] F. Wankmüller, P. R. Thimmapuram, K. G. Gallagher, and A. Botterud, "Impact of battery degradation on energy arbitrage revenue of grid-level energy storage", *Journal of Energy Storage*, vol. 10, pp. 56–66, 2017. DOI: 10.1016/j.est.2016.12.004.

[128] B. Heymann and P. Martinon, "Optimal battery aging: an adaptive weights dynamic programming algorithm", *Journal of Optimization Theory and Applications*, vol. 179, no. 3, pp. 1043–1053, 2018. DOI: 10.1007/s10957-018-1371-9.

[129] L. S. De Oliveira and S. F. Saramago, "Multiobjective optimization techniques applied to engineering problems", *Journal of the Brazilian Society of Mechanical Sciences and Engineering*, vol. 32, no. 1, pp. 94–105, 2010. DOI: 10.1590/s1678-58782010000100012.

[130] P. Nahmmacher, E. Schmid, L. Hirth, and B. Knopf, "Carpe diem: A novel approach to select representative days for long-term power system modeling", *Energy*, vol. 112, pp. 430–442, 2016. DOI: 10.1016/j.energy.2016.06.081.

[131] *SciPy optimization library in Python, https://docs.scipy.org/doc/scipy/reference/optimize.html, Accessed: August 18, 2020.*

[132] *MOSEK Modeling Cookbook, Release 3.2.2, May 04, 2020, p. 102, https://docs.mosek.com/mosekmodelingcookbook-letter.pdf, Accessed: December 02, 2020.*

[133] *Global or multiple starting point search in Matlab, https://www.mathworks.com/help/gads/global-or-multiple-starting-point-search.html, Accessed: September 14, 2020.*

[134] S. Boyd, L. Xiao, and A. Mutapcic, "Notes on decomposition methods", 2003, https://web.stanford.edu/class/ee3920/decomposition.pdf, Accessed: December 02, 2020.

[135] J. H. Ward, "Hierarchical grouping to optimize an objective function", *Journal of the American Statistical Association*, vol. 58, 1963.

[136] S. Pfenninger, "Dealing with multiple decades of hourly wind and PV time series in energy models: A comparison of methods to reduce time resolution and the planning implications of inter-annual variability", *Applied Energy*, vol. 197, pp. 1–13, 2017. DOI: 10.1016/j.apenergy.2017.03.051.

[137] *Agglomerative hierarchical clustering in Matlab, https://www.mathworks.com/help/stats/linkage.html, Accessed: August 18, 2020.*

[138] Swissgrid AG, "Präqualifikationsunterlagen - Primärregelung", Tech. Rep., May 29, 2020, https://www.swissgrid.ch/dam/swissgrid/customers/topics/ancillary-services/prequalification/3/F20200529-prequalification-documents-primary-control-de.pdf, Accessed: December 02, 2020.

[139] M. Koller, M. González Vayá, A. Chacko, T. Borsche, and A. Ulbig, "Primary control reserves provision with battery energy storage systems in the largest European ancillary services cooperation", in *CIGRE*, 2016, pp. 1–12.

[140] D. Kucevic, B. Tepe, S. Englberger, A. Parlikar, M. Mühlbauer, O. Bohlen, A. Jossen, and H. Hesse, "Standard battery energy storage system profiles: analysis of various applications for stationary energy storage systems using a holistic simulation framework", *Journal of Energy Storage*, vol. 28, p. 101 077, 2020. DOI: 10.1016/j.est.2019.101077.

[141] J. Fleer, S. Zurmühlen, J. Badeda, P. Stenzel, J. F. Hake, and D. U. Sauer, "Model-based economic assessment of stationary battery systems providing primary control reserve", *Energy Procedia*, vol. 99, pp. 11–24, 2016. DOI: 10.1016/j.egypro.2016.10.093.

[142] J. Engels, B. Claessens, and G. Deconinck, "Techno-economic analysis and optimal control of battery storage for frequency control services, applied to the German market", *Applied Energy*, vol. 242, pp. 1036–1049, 2019. DOI: 10.1016/j.apenergy.2019.03.128.

[143] T. Borsche, A. Ulbig, M. Koller, and G. Andersson, "Power and energy capacity requirements of storages providing frequency control reserves", in *IEEE Power and Energy Society General Meeting*, 2013. DOI: 10.1109/PESMG.2013.6672843.

[144] T. Borsche, A. Ulbig, and G. Andersson, "A new frequency control reserve framework based on energy-constrained units", in *Power Systems Computation Conference*, 2014. DOI: 10.1109/PSCC.2014.7038111.

[145] Swissgrid AG, "Balancing Roadmap Schweiz", Tech. Rep., April 2018, https://www.swissgrid.ch/dam/swissgrid/about-us/newsroom/publications/balancing-roadmap-ch-de.pdf, Accessed: December 02, 2020.

[146] Trading on EPEX SPOT 2019-2020, Tech. Rep., 2019, https://www.epexspot.com/sites/default/files/2019-02/2019-01-17_Trading%20Brochure_V2.pdf, Accessed: December 02, 2020.

[147] E. Redondo-Iglesias, P. Venet, and S. Pelissier, "Efficiency degradation model of lithium-ion batteries for electric vehicles", *IEEE Transactions on Industry Applications*, vol. 55, no. 2, pp. 1932–1940, 2019. DOI: 10.1109/TIA.2018.2877166.

[148] *Profitability index, https://corporatefinanceinstitute.com/resources/knowledge/accounting/profitability-index/, Accessed: August 28, 2020.*

[149] J. E. Harlow, X. Ma, J. Li, E. Logan, Y. Liu, N. Zhang, L. Ma, S. L. Glazier, M. M. E. Cormier, M. Genovese, S. Buteau, A. Cameron, J. E. Stark, and J. R. Dahn, "A wide range of testing results on an excellent lithium-ion cell chemistry to be used as benchmarks for new battery technologies", *Journal of The Electrochemical Society*, vol. 166, no. 13, A3031–A3044, 2019. DOI: 10.1149/2.0981913jes.

[150] F. Zimmermann, M. Densing, D. Keles, J. Dehler, F. Hack, and W. Fichtner, "Impact of different market designs in the CWE market area on electricity prices and on the competitiveness of Swiss hydropower", Swiss Federal Office of Energy, Berne, Switzerland, Tech. Rep., 2018.

[151] W. Cole and A. W. Frazier, "Cost projections for utility-scale battery storage: 2020 update", Tech. Rep., Golden, CO: National Renewable Energy Laboratory, 2020.

[152] Australian Energy Market Commision, Information: Five Minute Settlement, Sydney, Australia, Tech. Rep., 2017, https://www.aemc.gov.au/sites/default/files/content/18f019ff-de8c-40f3-836f-1bf3c8e43d2b/3-Info-Sheet.pdf, Accessed: December 02, 2020.

[153] Swissgrid AG, Ausschreibungsergebnisse Regelleistung, https://www.swissgrid.ch/de/home/customers/topics/ancillary-services/tenders.html#ausschreibungsergebnisse-regelleistung-prl, Accessed: September 09, 2020.

[154] G. Harper, R. Sommerville, E. Kendrick, L. Driscoll, P. Slater, R. Stolkin, A. Walton, P. Christensen, O. Heidrich, S. Lambert, A. Abbott, K. Ryder, L. Gaines, and P. Anderson, "Recycling lithium-ion batteries from electric vehicles", *Nature*, vol. 575, pp. 75–86, Nov. 2019. DOI: 10.1038/s41586-019-1682-5.

[155] P. Joshi Rajendra, J. Eickholt, L. Li, M. Fornari, V. Barone, and J. E. Peralta, "Machine learning the voltage of electrode materials in metal-ion batteries", *ACS Applied Materials & Interfaces*, vol. 11, no. 20, pp. 18 494–18 503, 2019. DOI: 10.1021/acsami.9b04933.

[156] A. Chen, X. Zhang, and Z. Zhou, "Machine learning: Accelerating materials development for energy storage and conversion", *InfoMat*, vol. 2, no. 3, pp. 553–576, 2020. DOI: 10.1002/inf2.12094.

[157] Q. Dai, J. C. Kelly, L. Gaines, and M. Wang, "Life cycle analysis of lithium-ion batteries for automotive applications", *Batteries*, vol. 5, no. 2, 2019. DOI: 10.3390/batteries5020048.

[158] I. Benítez, A. Quijano, J. L. Díez, and I. Delgado, "Dynamic clustering segmentation applied to load profiles of energy consumption from Spanish customers", *International Journal of Electrical Power and Energy Systems*, vol. 55, pp. 437–448, 2014. DOI: 10.1016/j.ijepes.2013.09.022.

[159] A. Pena-Bello, E. Barbour, M. C. Gonzalez, M. K. Patel, and D. Parra, "Optimized PV-coupled battery systems for combining applications: Impact of battery technology and geography", *Renewable and Sustainable Energy Reviews*, vol. 112, pp. 978–990, 2019. DOI: 10.1016/j.rser.2019.06.003.

[160] S. Schopfer, V. Tiefenbeck, and T. Staake, "Economic assessment of photovoltaic battery systems based on household load profiles", *Applied Energy*, vol. 223, pp. 229–248, 2018. DOI: 10.1016/j.apenergy.2018.03.185.

[161] A. Kies, "Joint optimisation of arbitrage profits and battery life degradation for grid storage application of battery electric vehicles", *Journal of Physics: Conference Series*, vol. 977, no. 1, 2018. DOI: 10.1088/1742-6596/977/1/012005.

[162] A. S. Sidhu, M. G. Pollitt, and K. L. Anaya, "A social cost benefit analysis of grid-scale electrical energy storage projects: a case study", *Applied Energy*, vol. 212, pp. 881–894, 2018. DOI: 10.1016/j.apenergy.2017.12.085.

[163] T. Terlouw, T. AlSkaif, C. Bauer, and W. van Sark, "Multi-objective optimization of energy arbitrage in community energy storage systems using different battery technologies", *Applied Energy*, vol. 239, pp. 356–372, 2019. DOI: 10.1016/j.apenergy.2019.01.227.

[164] S. Cui, Y. Wei, T. Liu, W. Deng, Z. Hu, Y. Su, H. Li, M. Li, H. Guo, Y. Duan, W. Wang, M. Rao, J. Zheng, X. Wang, and F. Pan, "Optimized temperature effect of Li-ion diffusion with layer distance in $Li(Ni_xMn_yCo_z)O_2$ cathode materials for high performance Li-ion battery", *Advanced Energy Materials*, vol. 6, no. 4, p. 1 501 309, 2016. DOI: 10.1002/aenm.201501309.

[165] A. Ehrl, J. Landesfeind, W. A. Wall, and H. A. Gasteiger, "Determination of transport parameters in liquid binary electrolytes: Part II. Transference number", *Journal of The Electrochemical Society*, vol. 164, no. 12, A2716–A2731, 2017. DOI: 10.1149/2.1681712jes.

[166] R. Fu, T. Remo, and R. Margolis, "2018 U.S. Utility-scale photovoltaics-plus-energy storage system costs benchmark", *National Renewable Energy Laboratory*, November 2018.